SYNTHESIS AND CHARACTERIZATION OF NANOCOMPOSITE SCINTILLATORS FOR RADIATION DETECTION

by

SUNIL KUMAR SAHI

Presented to the Faculty of the Graduate School of

The University of Texas at Arlington in Partial Fulfillment

of the Requirements

for the Degree of

DOCTOR OF PHILOSOPHY

THE UNIVERSITY OF TEXAS AT ARLINGTON

May 2016

Acknowledgements

I would like to thank to my advisor, Dr. Wei Chen for his support throughout the course of my dissertation work. This work would not have been possible without his guidance, support and patience.

I would also like to thank to our research collaborators Dr. Arnold Burger, Michael Groza from the “Department of Physics, Fisk University” and Dr. Rasool Kenarangui from the “Department of Electrical Engineering, University of Texas at Arlington” for helping me with the measurements. Also, many thanks to Dr. Alex Weiss, Dr. Andrew Brandt and Dr. Joseph Ngai, for taking their time to serve in my committee.

My sincere gratitude to all the members of my research group from post docs, visiting scholars, undergraduate students to graduate students, for helping me achieved my research targets.

I would like to express my deepest feeling towards my wife Merigold Malla. She was always there to drive me with positive energy. Finally, many thanks to my parents, grandparents, my siblings, my son and every members of my family for all their love and support.

April 14, 2016

Abstract

SYNTHESIS AND CHARACTERIZATION OF NANOCOMPOSITE SCINTILLATORS FOR RADIATION DETECTION

Sunil K Sahi, PhD

The University of Texas at Arlington, 2016

Wei Chen

Inorganic single crystal and organic (plastic and liquid) scintillators are commonly used for radiation detection. Inorganic single crystals are efficient and have better energy resolution compared to organic scintillators. However, inorganic single crystals are difficult to grow in large size and hence expensive. On the other hand, fast decay time and ease of fabrication makes organic scintillators attractive for many applications. However, poor energy resolution of organic scintillators limits its applications in gamma ray spectroscopy. The poor energy resolution is due to the low Z-Value and low density of organic scintillator. The Z-value of organic plastic scintillator can be increase by loading nanoparticles in plastic matrix. It is expected that the increase in Z-value would result in improve energy resolution of nanocomposite scintillator. However, the loss of optical transparency due to nanoparticles loading is one of the major concerns of nanocomposite scintillators.

In this dissertation, we used different methods to synthesize $La_xCe_{1-x}F_3$ nanoparticles with high dispersion in polymer matrix. High nanoparticle dispersion is important to load high concentration of nanoparticles into polymer matrix without losing the transparency of the polymer matrix. The as synthesized nanoparticles are dispersed into monomers and polymerized using heat initiated bulk polymerization method. Nanoparticles

are characterized using TEM, XRD, FTIR and TGA. The optical and scintillation properties of nanoparticles and nanocomposites are studied using spectroscopic techniques. The pulse height spectra obtained using nanocomposite fabricated by loading up to 30 wt% nanoparticles clearly show a photopeak for the 122 keV line of the Co-57 isotope. The generation of the photopeak is due to the enhanced photoelectric effect as a result of increased effective atomic number (Zeff) and density of nanocomposite scintillator. The pulse height spectra of Cs-137 gamma source show a full energy peak at around 622 keV, due to the escape of La and Ce Kα X-rays. The fabrication process of transparent nanocomposite scintillator is discussed in details.

Table of Contents

List of Illustrations

List of Tables

Chapter 1

Introduction

Nanoparticle research is currently a topical area of scientific interest due to its potential applications in various fields from optical, electrical to biological. A nanoparticle is a particle with at least one dimension less than 100 nm. The unique size dependent physical and optical properties such as the quantum confinement effect in semiconductor quantum dots, surface plasmon resonance in some metal nanoparticles and superparamagnetic effect in magnetic nanoparticles, makes nanoparticles different from their bulk counterparts.[1]

Luminescent materials which are also called phosphors are materials which emit light with energy above thermal radiation, when excited by certain types of energy. The electromagnetic radiation emitted by a luminescent material can be in any spectral region from UV, visible to infrared region. Luminescence materials are extensively used in areas such as lighting, coating, optoelectronic devices, radiation detection, pharmaceutical and biological application. Luminescent semiconductor quantum dots have been of particular interest due to their size dependent, tunable optical properties and high quantum yield.[2-4]

The advancement in nanotechnology has opened a new window for the development of polymer nanocomposites. A polymer nanocomposite is a combination of an organic polymer matrix and an additive that has at least one dimension in the nanometer range. Polymer nanocomposites have been studied for application in various fields such as radiation detection, coating, paints, sensors, LEDs, display, optoelectronics devices and biological application. [5, 6].

The main goal of this work is to investigate polymer nanocomposites for radiation detection. The first part of this dissertation is the synthesis of scintillating nanoparticles.

The second part is to embed the nanoparticles into polymers in order to fabricate nanocomposite scintillators for radiation detection.

Radiation detectors that used scintillators play an important role in many applications such as medical imaging, nuclear and high energy physics, safety control and homeland security. Scintillators are the materials that emit light when excited with ionizing radiations. However, not all luminescence materials can be use as scintillating materials. For scintillation application, materials should have high density and high Z value for high stopping power, fast decay time for good timing resolution and high light output. Also, the materials should be transparent to its emission wavelength. Inorganic single crystal and organic scintillators are the two main types of scintillators commonly used. Inorganic single crystals are preferred over organic plastic scintillator for gamma spectroscopy due to their high density and relatively good energy resolution. However, inorganic single crystal are difficult to grow in large size and hence expensive. Also, important single crystal scintillators like NaI, CsI and $LaBr_3$-Ce are hygroscopic and need special protection. Relatively low cost and availability as large size sheets make organic plastic scintillators ideal when a large detection area is required. However, organic scintillators have a low absorption coefficient and exhibit less probability for the photoelectric effect (low density and low Z value) resulting in poor energy resolution, limiting their use in gamma spectroscopy. This necessitates the research for new type of scintillators which combine the performance of single crystals and ease of fabrication of plastic scintillators.

Polymer nanocomposites have been researched as a new type of scintillators that can combine the advantages of both inorganic and organic scintillators. A nanocomposite scintillator is a scintillator that consists of scintillating inorganic nanocrystals embedded in a polymer matrix. Due to the incorporation of inorganic nanocrystals, nanocomposites are expected to have high density and eventually better energy resolution and higher efficiency

than organic plastic scintillators currently available. Furthermore, the use of polymer matrix allows for flexibility in producing these nanocomposite scintillators, making them easy to manufacture and inexpensive.

To manufacture these nanocomposite scintillators, two steps are involved: the first step is the synthesis of nanoparticles and secondly to disperse the nanoparticles in a polymer matrix and fabrication of polymer nanocomposite by heat initiated bulk polymerization. Nanoparticles can be synthesized with various techniques such as wet chemistry method, solid state method, hydrothermal, combustion synthesis and etc. In the second step, it is desirable that the nanoparticles have high dispersion into polymer matrix to obtain optically transparent nanocomposite scintillators. To obtain the highly dispersible nanoparticles it is required to coat the surface of the nanoparticles either during the synthesis or post synthesis. In this dissertation, many different coating techniques were investigated to achieve nanoparticles with high dispersion into polymer matrix.

Nanocomposite scintillators are frequently observed to display luminescence quenching, to avert this dilemma, nanocomposite scintillators based on fluorescence resonance energy transfer (FRET) principle are being proposed within this dissertation. [7] FRET is a distance dependent energy transfer principle in which an excited fluorophore can transfer its energy to another. The efficiency of this energy transfer is inversely proportional to the sixth power of the distance between donor and acceptor fluorophore. This dissertation work, describes the synthesis techniques, surface coating, characterization and fabrication of nanocomposite scintillators. In this work, FRET based nanocomposite scintillators, are investigated, by combining the high density of $La_xCe_{1-x}F_3$, $0 x \leq 1$ nanoparticles with quantum dots and scintillating organic dyes.

Chapter 2

Background

2.1 Scintillator Properties and Requirements

A scintillator is a material that converts high energy radiation such as X-ray or gamma-ray to a UV or visible light. Inorganic single crystals and organic scintillators are widely used as scintillators, depending on the demand of applications. The detector requirements differ depending on the applications, thus consequently, the scintillator requirements also differ. However, the basic requirements for many applications are simply a high light output, fast decay time, high density and a high atomic number (Z).[8] In addition to the basic requirements, scintillator materials are required to be transparent to its emission wavelength, be able to discriminate between gamma-rays with slightly different energy (energy resolution), have the ability to grow in large size and be cost effective.

Inorganic scintillators are preferred over organic scintillator for gamma-ray spectroscopy due to its high light yield and better energy resolution compare to organic scintillator. The high stopping power as a result of its high density makes inorganic scintillator more efficient compared to organic scintillator. The better energy resolution in inorganic scintillators is due to high atomic number (Z) of inorganic scintillators. Since the photoelectric absorption is proportional to the Z^{4-5} whereas Compton scattering is proportional to Z. The higher Z value causes photoelectric effect to be more prevalent in inorganic scintillators. The higher number of photoelectric interactions directly causes the photopeak in a pulse height spectrum taken with inorganic scintillator to be more predominantly featured than one taken with an organic scintillator. However, inorganic scintillators are difficult to grow in large size and hence are expensive. This limits its application in the area where large size detector is required. In addition, some promising inorganic single crystals are very hygroscopic and needs special protection from the

environment. Furthermore, some bright inorganic scintillators such as NaI(Tl) and CsI(Tl) have longer decay time which limit their application in the field where fast timing is necessary. On the other hand, organic scintillators have fast decay time which is desirable for many applications. In addition, the cost effectiveness, production ease and flexibility concerning shape and size makes organic scintillators an attractive alternative for large area detection. However, their low density and low Z value result into poor energy resolution, limiting its application in gamma-ray spectroscopy. Scintillation properties of some common inorganic and plastic scintillator are listed in Table 2-1.

Table 2-1 Scintillation properties of some common scintillators

Scintillator	Density (g/cc)	Emission wavelength (nm)	Light output (photons/MeV)	Decay time (ns)	Energy Resolution at 662 keV(%)	Hygroscopic	References
NaI(Tl)	3.67	410	38,000	230	6	Yes	[8]
CsI (Tl)	4.51	560	65,000	1300	4.3	Slightly	[9]
BGO (Bi4GeO12)	7.12	480	9,000	300	9.0	No	[10]
CeF_3	6.16	330	4,000	30		No	[11, 12]
BaF_2	4.88	310/220	11,000/1500	600/0.8	12	No	[10]
Plastic scintillator	1.03	423	10,000	2		No	[13, 14]
$LaBr_3$(Ce)	5.3	360	61,000	25	3.2	Very	[15]

2.2 Gamma-Ray Interactions in a Scintillator

Scintillation mechanisms are different depending on the scintillator type (organic or inorganic). However, the general mechanism of radiation interaction remains the same in both organic and inorganic. An X-ray or gamma ray is uncharged and creates no direct ionization or excitation of the materials through which it passes. Therefore, the detection of gamma rays is critically dependent on causing the gamma ray photon to undergo an interaction that transfers all or part of the incident gamma energy to an electron in the absorbing materials. In a gamma-ray detector, gamma- rays that enter the detector will interact with its medium in one of three different ways to generate primary electrons:

1) Photoelectric effect

2) Compton scattering

3) Pair production

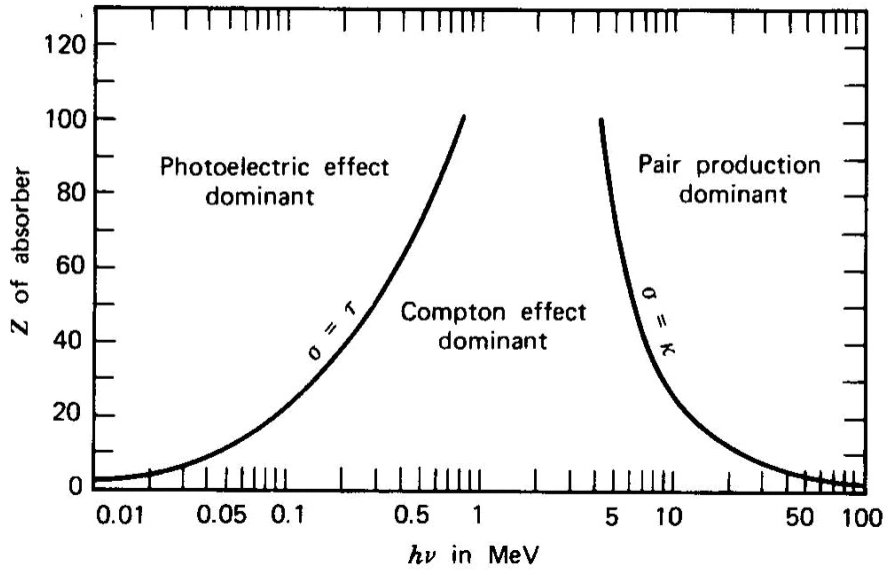

Figure 2-1 The various regions where the different gamma-ray interactions are dominant.[16]

The photoelectric effect is dominant for low energy gamma rays (up to several hundred keV) and high Z materials. In the photoelectric effect, the incident gamma–ray photon is absorbed by an inner shell electron, and an energetic primary electron is ejected from one of the electron shells of the absorber atom with a kinetic energy (E_{e^-}) given by the incident photon energy ($h\nu$) minus the binding energy (E_b) of the electron in its original shell.

$$E_{e^-} = h\nu - E_b \tag{2.1}$$

Compton scattering interaction is dominant for moderate energies. In Compton scattering a gamma-ray scatters off of an electron, thus creating a scattered gamma-ray photon and a recoil electron. In the process, the energy of the gamma-ray photon is divided between the two with a relationship that is dependent on the scattering angle and as in the photoelectric effect; the scattered electron is freed from the atom. The energy of the scattered gamma ray $h\nu'$ in terms of its scattering angle Θ is given by

$$h\nu' = \frac{h\nu}{1+\frac{h\nu(1-cos\theta)}{m_0\ c^2}} \tag{2.2}$$

Where, m_0c^2 is the rest mass of the electron. The kinetic energy of the recoil electron is therefore given by,

$$E_{e-} = h\nu - h\nu' = h\nu\left[\frac{\frac{h\nu\,(1-cos\theta)}{m_0c^2}}{1+\frac{h\nu(1-cos\theta)}{m_0c^2}}\right] \tag{2.3}$$

The two extreme cases for Compton scattering are: 1) When $\Theta = 0$, $h\nu' = h\nu$ and $E_{e^-} = 0$, the scattered photon retains all of its energy and the recoil electron gains no energy.

2) When Θ = π, the incident gamma-ray is backscattered and the recoil electron moves along the direction of incidence. In this case, the maximum energy is transferred between the incoming gamma-ray and the electron. In this case hν´ and E_{e-} are given as

$$h\nu' = \frac{h\nu}{1+\frac{2h\nu}{m_0\ c^2}} \text{ and } E_{e-} = h\nu\left[\frac{\frac{2h\nu}{m_0c^2}}{1+\frac{2h\nu}{m_0c^2}}\right] \quad (2.4)$$

In the detector, all the scattering angles from 0 to π will occur. Therefore, a continuum of energies can be transferred to the electron as shown in Figure 2-2 below

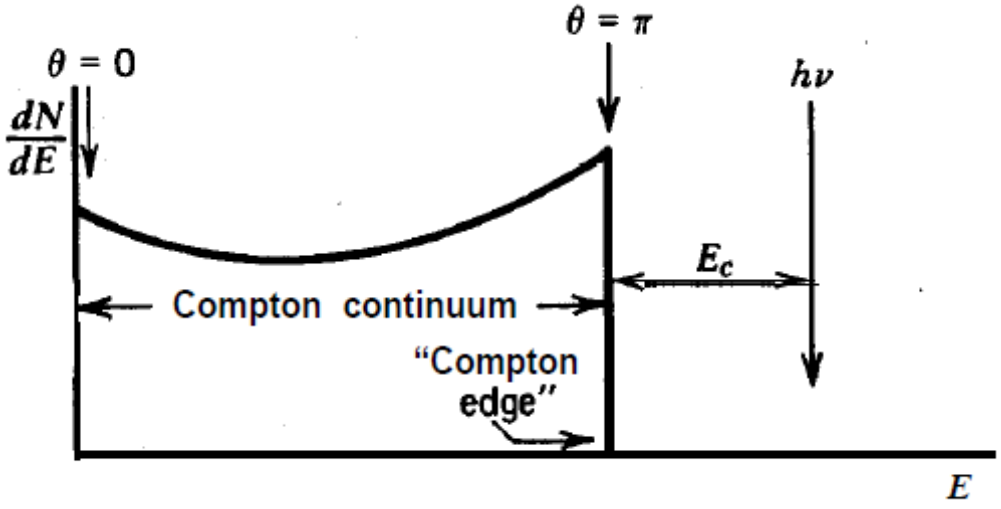

Figure 2-2 The Compton continuum in the gamma-ray detectors.[16]

The third significant gamma-ray interaction is the pair production. This process occurs when the gamma-ray is in the electric field of a nucleus of the absorbing material and corresponds to the creation of an electron-positron pair at the point of complete disappearance of the incident gamma-ray photon. In pair production, a gamma-ray with the minimum energy of $2m_0c^2$ (1.02 MeV) is required to create the electron – positron pair.

If the incident gamma-ray energy exceeds this value, the excess energy appears in the form of kinetic energy shared by the electron-positron pair. Therefore, the conservation of energy gives

$$E_{e-} + E_{e+} = h\nu - 2m_0c^2 \quad (2.5)$$

The plot of the total kinetic energy created by the incident gamma-ray is a delta function that is located $2m_oc^2$ below the incident gamma-ray energy $h\nu$. The position of this energy is called the double escape peak in an actual gamma-ray pulse height spectrum. The pair production process is complicated due to the fact that a positron is not a stable particle. Once the kinetic energy of positron becomes very low, it will annihilate or combine with an electron in the absorbing medium. Upon annihilation, both disappear and they are replaced by two annihilation gamma-ray photons of energy m_oc^2 each. The time required for this process is small and therefore appears to coincide with the original pair production. In some cases only one of the annihilation photons is absorbed inside the detector producing a peak that is known as single escape peak on the pulse height spectrum.[16, 17]

The three cases of above mentioned gamma-ray interactions, in which a primary electron is generated by the incident gamma-ray. This energetic primary electron travels in the detector volume, producing secondary electrons. When the primary electron is no longer capable of generating secondary electrons, the electron cascade stops and the electrons de-excite to the ground state and emit photons of lights. However, the luminescence produced by the incident gamma-ray is extremely weak and requires amplification for meaningful analysis. This amplification is usually performed by a photomultiplier tube (PMT). Figure 2-3 shows the basic elements of a photomultiplier tube.

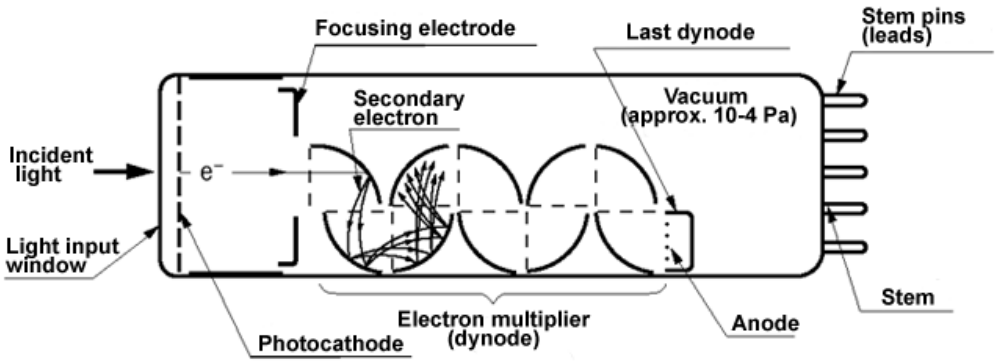

Figure 2-3 Schematic of basic element of a photomultiplier tube.[18]

PMTs convert light signals, that typically consist of no more than a few hundred photons, into a usable current pulse without adding a large amount of noise to the signal. A PMT is a vacuum tube with a photosensitive layer called the photocathode at one end coupled to an electron multiplier structure called dynode and an anode on the other end. The scintillation photons incident on the photocathode are converted to the electrons through the photoelectric effect. These photoelectrons are accelerated by a strong electric field in the PMT. As the photoelectrons are accelerated, they collide with the surface of an electrode, called a dynode, which releases additional electrons called secondary emission. Dynodes are typically made of cesium, antimony, or silver-magnesium due to their low work functions, which is the minimum energy needed to eject an electron from the material. This increased electron flux is then further accelerated to collide with succeeding electrodes, causing a large electron multiplication. The typical value of multiplication factor is on the order of 10^{7} – 10^{10} on a modern PMT. This process of electron multiplication continues through a series of electrodes until they reach the anode. The magnitude of charged collected at the anode is proportional to the charge liberated at the photocathode of the PMT; the constant of proportionality is the gain of the PMT. The amount of charge

liberated at the photocathode is proportional to the amount of light incident on the photocathode which in turn is proportional to the amount of energy deposited by the gamma-ray in the scintillator. Therefore, the output signal produced is proportional to the energy deposited by the gamma-ray in the scintillator.[18] Figure 2-4 shows the typical gamma-ray spectrum of NaI (Tl) scintillator in response to the 662 keV gamma-rays. The characteristics features such as Compton continuum, Compton edge and photopeak are clearly observed in the spectrum. One of the most important characteristics of a scintillator detector is the energy resolution. Energy resolution of a scintillator detector is defined as the ratio of the full width at half maximum and peak energy value. Energy resolution is typically measured for the 662 keV (Cs 137) energy peak. The energy resolution of a detector depends on various factors such as gamma-ray energy, light output of scintillator, size of the scintillator detector, photomultiplier characteristics, and noise presence in the processing electronics and the non-linearity of the scintillator. The non-linearity of a scintillator is defined as the variation in the number of photons emitted by the scintillator for a given electron energy. The next section will describe the scintillation mechanism in organic, inorganic and nanocomposite scintillators.

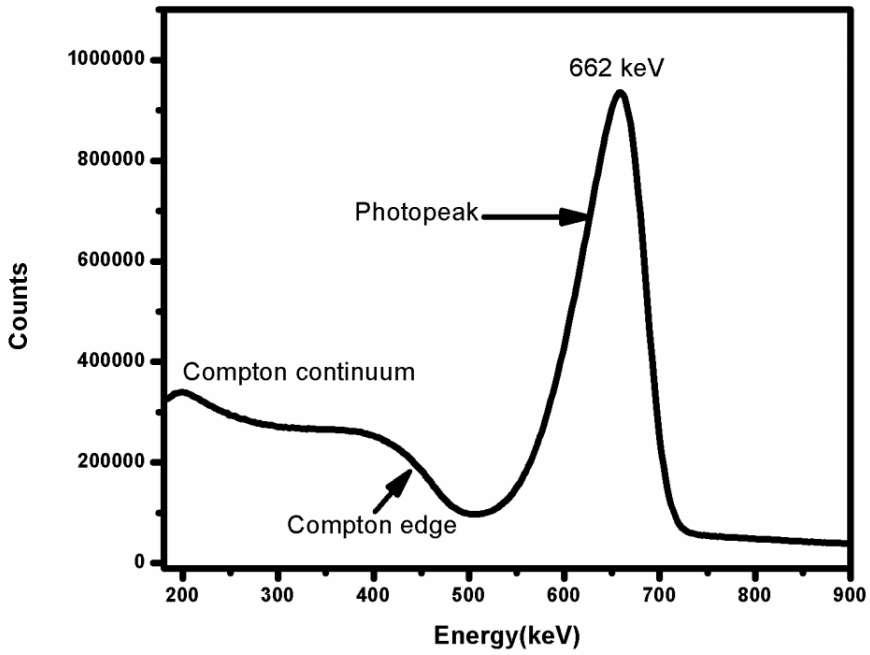

Figure 2-4 Pulse-height spectrum of 662 keV (Cs-137) gamma –ray recorded with NaI(Tl) single crystal scintillator using our detection system.

2.3 Scintillation Mechanism

2.3.1 Inorganic Scintillators

Inorganic scintillators are typically single crystals of different materials such as halides, oxide, fluorides, and sulfide. They can be pure crystals such as CsI and CeF_3 or doped with some impurities such as Tl^+, Eu^{2+} and Ce^{3+}. Examples of doped scintillators are- NaI(Tl), $LaBr_3$(Ce), LaF3(Ce) and SrI_2(Eu). The scintillation mechanism depends on the structure of the crystal lattice. In a pure inorganic crystal such as insulators or semiconductors, electrons are only allowed to occupy discrete energy bands as shown in

Figure 2-5. The lower energy band is called the valence band in which electrons are essentially bound at the lattice sites, whereas the conduction band represents free electrons. The forbidden band or band gap is the intermediate band of energies in which electrons can never be found in the pure crystal. In a pure crystal, absorption of energy can result in the transfer of electron from the valence band to the conduction band, leaving a hole in the normally filled valence band. However, the de-excitation of an electron to the valence band with the emission of a photon is an inefficient process in pure crystals. In addition, many pure inorganic crystals have large band gaps resulting in photon emissions with energy higher than the visible photons, which are difficult to detect with the commonly used photomultiplier tube.[19]

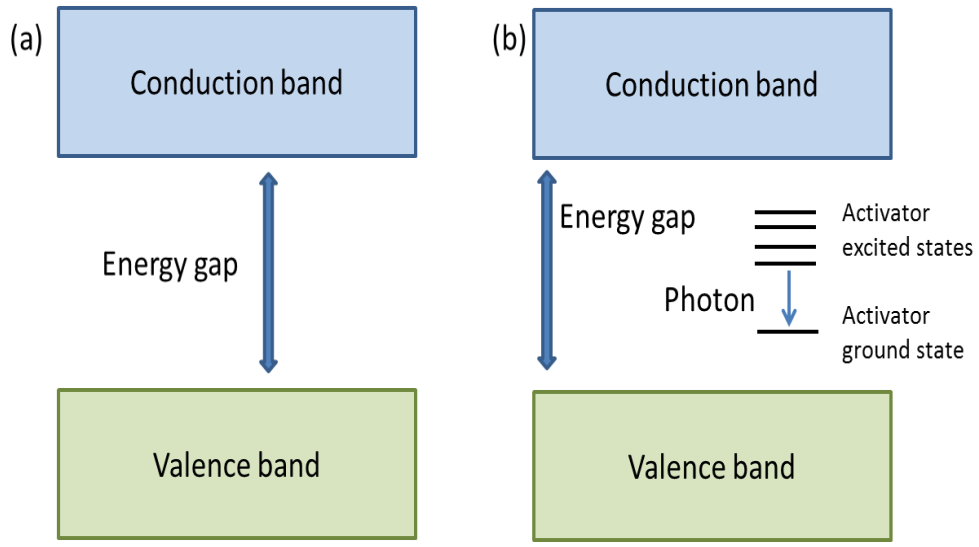

Figure 2-5 (a) Energy band gap of intrinsic scintillator crystal and (b) Energy band gap of an impurity doped (extrinsic) inorganic scintillator crystal.

To enhance the probability of visible photon emission, a small amount of an impurity called activators are commonly added to inorganic crystals. The addition of

activators creates special sites in the crystal lattice at which the band structure is modified from that of the pure crystal. These activators will create the intermediate energy states within the energy band gap through which the electron can de-excite to the valence band emitting lower energy photons (visible photons). These de-excitation sites are called luminescence centers or recombination centers because the de-excitation from the excited states of the activator leads to luminescence.

The scintillation mechanism of inorganic scintillators can be divided into three main processes: 1) energy conversion of creation of electron-hole pairs, 2) thermalization and migration of electron-hole pairs and energy transfer to luminescent centers, and 3) recombination of electron-hole pairs and luminescence. A schematic of luminescence mechanism in inorganic scintillator is shown in Figure 2-6.

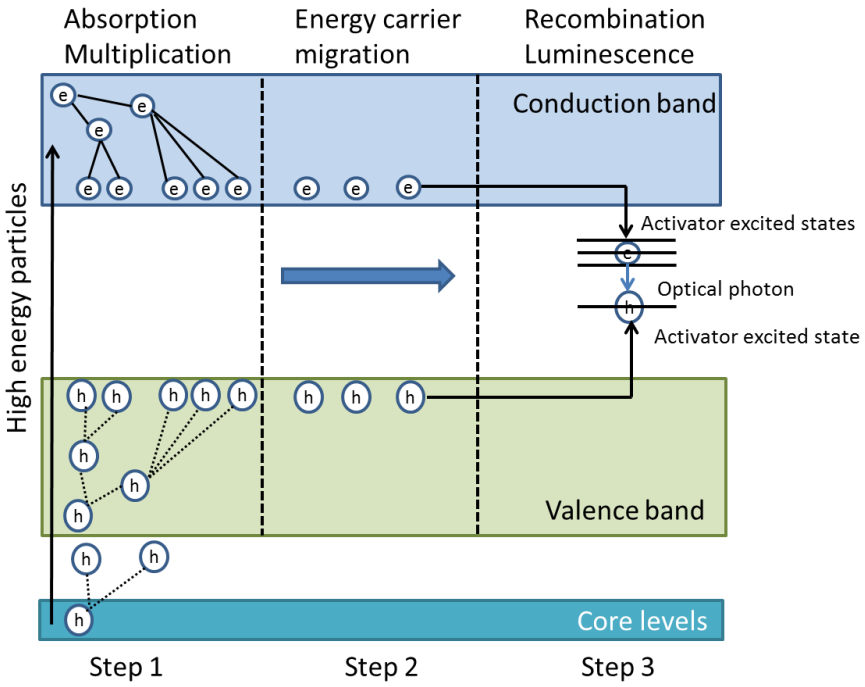

Figure 2-6 Schematic of various steps of scintillation mechanism in inorganic scintillator

When the incident radiation is absorbed by the scintillator material, there is a creation of primary electron-hole pairs due to the elevation of electrons from the valence to the conduction band. The excited electrons are free to migrate through the crystal and in the process lose it energy creating other electron-hole pairs through inelastic electron-electron scattering and Auger processes. These secondary electrons are also free to travel through the crystal creating further electron-hole pairs. This process of electrons and holes multiplication continues until the electron energies become less than the ionization threshold. At the end of this process the electrons and holes thermalize to the bottom of the conduction band and the top of the valence band respectively. In the next step, the electrons and holes migrate and recombine at the luminescence center. If the electron upon recombining with the hole at the luminescence can create an excited configuration with an allowed transition to the ground state, it will de-excite with an emission of a photon. Whereas, if the transition to the ground state is forbidden, such states require an additional increment of energy to raise them to a higher lying state from which the de-excitation to the ground state is possible. This process results in the emission of photons with slower decay time called phosphorescence. Phosphorescence is not beneficial to scintillation applications due to its production of background light or after glow.[20]

When an electron and hole recombine at an activator site, certain radiation-less transition or transition without the emission of visible photons are also possible between some excited states and the ground state. This process is called quenching and results in the diminished scintillation light yield. Furthermore, the electron-hole pair may migrate together in a loosely associated configuration known as an exciton. These excitons can travel to a luminescent center and de-excite to the ground state producing scintillation light in the process. This phenomenon is common in wide band-gap oxide and halide scintillators. Scintillation mechanism in some common inorganic scintillators are shown in Table 2-2.

Table 2-2 Radiative transitions in some scintillators

Scintillator	Type	Emission transition
NaI(Tl^{+})	Extrinsic(activated)	6p-6s
$LaBr_3$(Ce^{3+})	Extrinsic(activated)	5d-4f
Gd_2O_3(Eu^{3+})	Extrinsic(activated)	4f-4f
Semiconductors CdS(In), ZnO (Ga)	Extrinsic(activated)	Excitonic
CeF_3	Intrinsic (self-activated)	5d-4f
BaF_2	Intrinsic (self-activated)	Core-valence band
CsI	Intrinsic (self-activated)	Self-trapped exciton
$CdWO_4$	Intrinsic(self-activated)	Charge transfer

2.3.2 Organic Scintillators

Organic scintillators are typically an aromatic hydrocarbon compound which contain benzene ring structures interlinked in various ways. Organic scintillators are available as crystal, liquid and plastic scintillators. Organic crystals are composed of organic molecules held together by van der Waals force between molecules. The most common organic crystal scintillators are anthracene, stilbene and naphthalene. Anthracene has the highest light output of all organic scintillators. However, its response is anisotropic and difficult to grow in large size. Organic liquid scintillators are made by dissolving organic

scintillating fluors and a wavelength shifter in organic solvent such as toluene, xylene and benzene. The typical solutes are scintillating fluors such as p- terphenyl, PBD, PPO and wavelength shifter such as POPOP. The wavelength shifter is added to match the spectral sensitivity range of a PMT. The plastic scintillators are organic scintillators in which the primary fluorescent emitter, called a fluor, is suspended in a polymer matrix called a base. The organic plastic scintillators are the interest of this dissertation.

The fluorescence process in organic scintillators arises from the transitions in the energy levels of a single molecule and therefore can be observed independently of the physical state. For example, anthracene is observed to fluoresce as a solid polycrystalline material, as a vapor or as a part of a multicomponent solution. The scintillation in all three types of organic scintillators is due to the de-excitation of π electrons in an aromatic organic compound such as a benzene ring. π electrons are delocalized electrons occupying π orbitals, which corresponds to the double bond structure in an aromatic molecule. π bonds are formed by the overlap of p orbitals between two adjacent atoms. These bonds are usually weaker than sigma bonds, which form bonding orbitals directly between the nuclei of the bonding atoms, resulting in greater overlap and a strong sigma bond. π electrons are of special interest in organic scintillator as their de-excitation often leads to fluorescence.[21] The π electronic energy level of an aromatic molecule is illustrated in Figure 2-7.

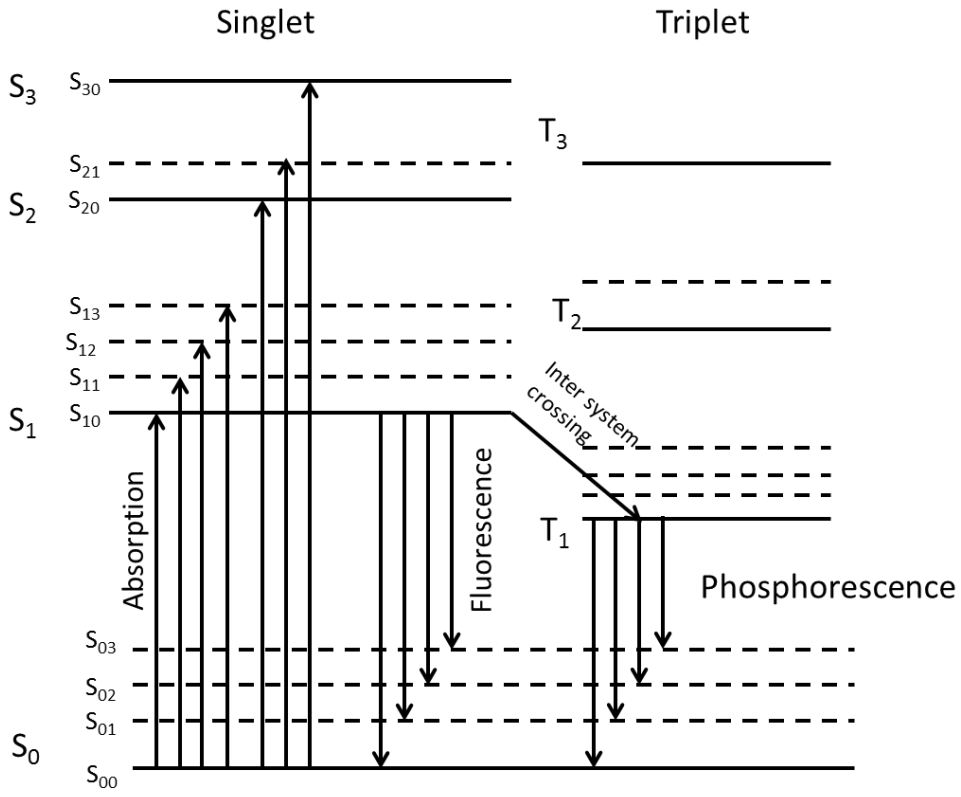

Figure 2-7 Energy level diagram of an organic molecule with π- electron structure.[22]

The fluorescence molecule in the organic scintillator absorbed the energy and get excited into any one of a number of excited states. As shown in Figure 2-7 S_0, S_1,S_2 and S_3 are the singlet states where as T_1, T_2, T_3 are the triplet states of an excited molecule. A singlet is an electronic state with zero total angular momentum and a triple state is an electronic state with a non-zero total angular momentum. Each electronic state is subdivided into various vibrational states with much finer energy spacing and represented by a second subscript in Figure 2-7. Since the space between the two vibrational states is large compared to the average thermal energy, nearly all the molecules at room temperature are in the S_{00} state. The higher singlet electronic states, such as S_3 or S_2, will

quickly de-excite (on the order of picosecond) to the S_1 state through radiationless internal conversion. Furthermore, the excess vibrational energy will release through lattice vibrations producing a population of excited molecules in the S_{10} state. The molecule will undergo the transition from excited S_{10} to one of the vibrational state of the ground state S_0, emitting a photon in the process. This transition, if allowed takes place at times of the order of nanosecond. However, some excited singlet states may transition into a triplet states through non-radiative transition known as intersystem crossing. The transition from T_1 to S_0 is a delayed light emission process known as phosphorescence. [16, 22, 23]

As observed in Figure 2-7, the energy of the photon emitted in transition from lowest excited S_{10} to the ground state S_0 is lower than the minimum energy required for excitation. This difference in energies of the absorbed photon and emitted photon is called Stokes shift and is important to avoid self- absorption of emitted photons.

In the case of plastic scintillators, the incoming high energy radiation deposits its energy in the polymer base such as polystyrene and polyvinyl toluene. This will excite a primary electron and populate one of the many excited states. After excitation, the primary electron may de-excite to a lower energy level and excite nearby electrons through inelastic electron-electron scattering, forming an electron cascade. This process will continue until the primary electron is no longer capable of further exciting the secondary electrons. The energy transfer will occur between the polymer base and fluor molecule. This is possible because the excited electronic states of the fluor molecule lie at the lower energy level than those of polymer base. The energy transfer process is dependent on the scintillator type. In a plastic scintillator, the energy transfer is due to the long range dipole-dipole energy interaction known as Foster Resonance Energy Transfer (FRET). FRET is a distance based energy transfer principle, in which a donor fluorophore in an excited electronic state may transfer its excitation energy to a nearby acceptor chromophore through a non-

radiative process. In principle, if the fluorescence emission spectrum of the donor molecule overlaps with the absorption spectrum of the acceptor molecule, and the two are within a minimal spatial distance, the donor can transfer its excitation energy to the acceptor. The efficiency of energy transfer is inversely proportional to the sixth power of the distance between donor and acceptor molecules. Figure 2-8 shows the Jablonski diagram of Forster resonance energy transfer principle. The energy transfer from polymer base to the fluor is important because the fluor contains aromatic molecule in which the de-excitation of π electrons to ground state is highly likely to emit an optical photon.

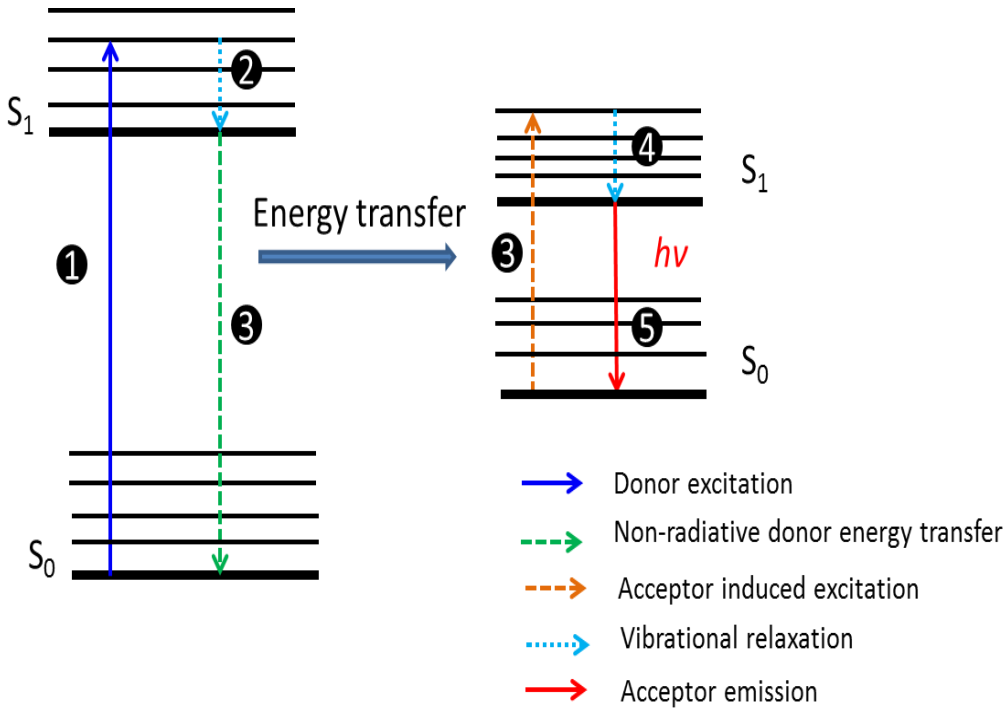

Figure 2-8 Jablonski diagram of Forster Resonance Energy Transfer.

2.4 Composite Scintillators

Both inorganic and organic scintillators have their advantages and disadvantages. Inorganic scintillators have high light efficiency and relatively good energy resolution whereas fast decay times, ease of manufacture and cost effectiveness makes organic scintillators an attractive alternative. However, none of these scintillator types combine the basic scintillators requirements such as high light yield, good energy resolution and fast decay time. This necessitates the search for a new scintillator type to combine the advantages of both inorganic and organic scintillators. With the development in nanotechnology, nanocomposite scintillators have emerged as a promising scintillator type, combining the properties of both inorganic and organic scintillators. An ideal composite scintillator would have high light yield, good energy resolution and fast decay time to combine with the easiness to manufacture and cost effectiveness. Various approaches have been utilized to fabricate composite scintillators by loading high-Z materials.

Since the middle of the last century, composite loaded with high – Z organometallic compounds to increase the Z_{eff} and density have been reported.[7, 24-29] However, composite scintillators fabricated in this manner suffered from luminescence quenching and loss of optical transparency. Recently, Rupert et al. demonstrated enhanced gamma stopping power using bismuth organometallic compound as a high density filler in polyvinylcarbazole polymer.[30] However, it has been reported that high – Z organometallics compound are thermally unstable.[31, 32]

With the development in nanotechnology, inorganic nanoparticles and quantum dots have been heavily studied as a filler to increase the density of plastic scintillators.[33-38]. It has been reported that the loss of optical transparency in the conventional composite scintillators made by mixing the micron size inorganic filler and organic matrix was due to

the mismatch of the refractive index between the filler and the organic matrix. [39] However, Mickigney et al. reported that the sufficiently small size of nano-filler could lead to the minimized optical scattering even with a large mismatch of refractive index.[38] Several techniques have been reported to fabricate quantum dot embedded nanocomposite scintillators for gamma ray spectroscopy. For example, Dai et al. used sol-gel method to fabricate composite scintillator by embedding CdSe/ZnS quantum dots in lithiated ^{6}LiOH gels. The resulting scintillators are transparent and highly fluorescent producing scintillation under alpha particle excitation.[40] Gamma ray excitation studies of CdSe/ZnS quantum dots were performed by embedding quantum dots in nanoporous glass matrix by Latent et al. Their studies shows better energy resolution of 59-KeV gamma ray from americium-241 than that of NaI single crystal.[36] However, the efficiency of the nanocomposite scintillator is so low that the spectrum was recorded over a three day acquisition time. Manickaraj et al. fabricated transparent silica-glass and polymer nanocomposite embedded with 0.5 wt% CdTe quantum dots. Nanocomposites were tested under irradiation using a ^{241}Am radionuclide source. However, the counting rate of only 18-30 counts/second was obtained from the nanocomposite samples.[41] Composite film of CdSe/ZnSe core/shell quantum dots dispersed in conjugated polymer was fabricated by spin coating method. However, they were too thin to attenuate high energy gamma rays, since the mean free path of an X-ray or gamma-ray in solid matter ranges from tens of microns to tens of centimeters depending on their energy.[42] Kang et al. synthesized CdTe quantum dots embedded in polyvinyl alcohol and polymethyl methacrylate (PMMA) matrix for X-ray imaging. Polymerizable surfactant, octadecyl-p-vinylbenzyl dimethylammonium chloride (OVDAC) was used to extract aqueous CdTe quantum dots from water into methyl-methacrylate monomer.[34] However, no reports have been found on sufficient loading of quantum dots to produce the photo peak under gamma excitation.

Also, most of the quantum dots embedded nanocomposites emit in the region where the quantum efficiency of commonly used PMT's are low.[42-44]

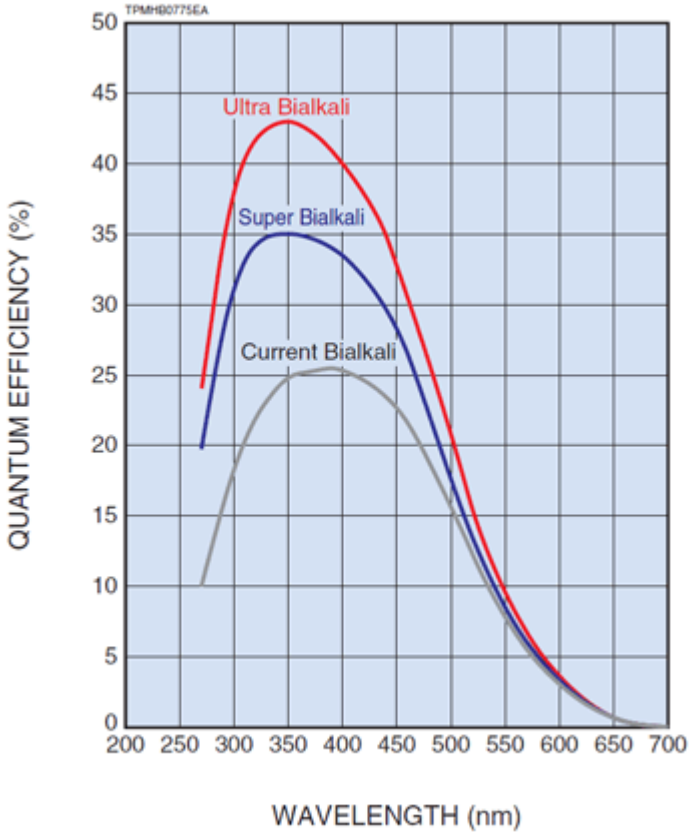

Figure 2-9 Quantum efficiency of versus wavelength of various photocathode from Hamamatsu.[18]

High density rare earth nanoparticles were also heavily studied as nano-filler for nanocomposite scintillators. Feller et al. used oleic acid as both a ligand and an organic matrix to synthesized $Ce_xLa_{1-x}F_3$ nanocrystals embedded transparent nanocomposite.[45] However, the nanocomposites exhibit limited light yield as well as the low mechanical strength of oleic acid matrix limits its application. Kang et al. used similar method to

synthesize oleic acid coated BaF_2-Ce nanophosphors and embedded into epoxy matrix with closely matched index of refraction.[46] However, the nanocomposites showed significant loss of transparency at nanoparticles loading concentration of less than 10 wt%. Yao et al. used LaF_3:Ce nanoparticles loaded in to ORMOSILs for scintillator application.[35] Sahi et al. reported luminescence enhancement of PPO/PVT scintillator by embedding oleic acid coated CeF_3 nanoparticles under UV and X-ray excitation.[47] However, at loading concentration higher than 10 wt% nanocomposite lose transparency resulting into diminished light yield. Cai et al. fabricated nanocomposite scintillator by embedding non-fluorescent Gd_2O_3 nanocrystals in PVT matrix. The nanocomposite are highly transparent even at high nanoparticles loading concentration of 31 wt% and exhibit a beta light yield more than twice that of conventional plastic scintillator. It was suggested that the wide band gap of Gd_2O_3 gamma photosensitizer helps to avoid the luminescence quenching in nanocomposites. Whereas the small size of nanocrystals, small difference of index of refraction between nanocrystals and polymer matrix as well as the multifunctional ligand helps to maintained the transparency of the nanocomposite.[32] However, the Recently, Liu et al. fabricated nanocomposite for gamma ray spectroscopy by embedding HfO_2 nanoparticles in PVT matrix. The nanocomposite exhibit high light transmittance even at a loading concentration as high as 40 wt%. The 20 wt% HfO_2 loaded nanocomposite produced a deconvoluted photopeak with energy resolution ≤ 8% for 662 keV Cs-137 gamma radiations. It was suggested that the high Z- value of Hf resulting in increased photoelectric cross-section is responsible for the production of photopeak. However, it was reported that the gamma light yield and photopeak resolution did not improve with large size nanocomposite or with the higher nanoparticle loading. [48]

Our group has shown that the nanocomposites of rare earth based nanoparticles and semiconductor quantum dots can combine the high density and efficiency of rare earth

based nanoparticles with the fast decay of quantum dots for scintillation application. [49, 50]. However, it is still a big challenge to fabricate a nanocomposite scintillator with a desired transparency at a concentration high enough to produce a photo peak under gamma ray excitation, especially for the bulk size.

In this work, we have synthesized Cerium (Ce^{3+}) doped rare earth fluoride nanoparticle as a high density nano filler to fabricate nanocomposite scintillator for radiation detection. Ce^{3+} ion has emission within the UV region and a peak ranging from 310 to 360 nm in rare earth fluoride host. This emission is in the region where the efficiency of the PMT is low as shown in Figure 2-9. This affects the efficiency of the scintillators. To overcome this problem, we have used quantum dots or organic dye to shift the emission of Ce^{3+} in rare earth fluorides to longer wavelength through FRET energy transfer principle. We have also used organic polymers such as polyvinyl toluene, polystyrene and poly (methyl methacrylate) as organic matrix to embed nanoparticles to fabricate the nanocomposite scintillator.

Chapter 3

Nanocomposites Characterization Instrumentation

3.1 Introduction

Different characterization instrumentations are used to evaluate the inorganic nanoparticles and nanocomposite scintillators. Powder X-ray diffraction (XRD) is used to structurally characterize the as synthesized nanoparticles. The size of the nanoparticles is determined using transmission electron microscopy (TEM) and scanning electron microscopy (SEM). Photoluminescence spectroscopy and ultraviolet-visible spectroscopy (UV-Vis) are used to study the optical properties of nanoparticles and nanocomposite scintillators. Fourier transform infrared spectroscopy (FTIR) is used to characterize the organic coating on the nanoparticles surface. Thermogravimetric analysis (TGA) is used to study the amount of organic coating on the surface of nanoparticles. X-ray excited optical luminescence and gamma ray spectroscopies are used to measure the radiation response of the nanoparticles and nanocomposite scintillators. The characterization tools used are described in the following sections.

3.2 Powder X-ray Diffraction

. X-ray powder diffraction measurement is a method for measuring characteristic X-ray diffraction angles and intensities from randomly oriented powder crystallite sample irradiated by a monochromatic X-ray beam. X-ray diffraction is based on the constructive interference of two scattered monochromatic X-rays. The interaction of the incident monochromatic rays with the sample produces constructive interference when conditions satisfy Bragg's law ($n\lambda = 2d \sin \Theta$) which is discuss in the following subsection.

By scanning the sample through an angle θ of incident X-ray beams form 0 to 90^{o}, all possible diffraction directions of the lattice can be attained due to the random orientation of the powdered material. This allows identification of the material as each of these angles is associated with a different atomic spacing and each material has a set of unique d spacing. Therefore the X-ray powder diffraction method can be used for the qualitative and quantitative evaluation of crystal forms.

The instrument used to performed X-ray diffraction is called diffractometer as shown in Figure 3-1. It consists of an X-ray tube, a monochromator, a collimator, a sample stage and an X-ray detector. An X-ray tube uses a filament to produce electron which are then accelerated to bombard a target. Copper, molybdenum, cobalt and tungsten are some common target materials. When the target material bombarded with electrons accelerated from the cathode filament, two types of X-ray spectra are produced.

The first is called continuous spectra. In this process radiation is emitted by the high-speed electrons themselves as they are slowed or even stopped in passing near the positively charged nuclei of the anode material. This radiation is often called white radiation, since it consists of a range of wavelengths of X-rays with minimum wavelength and intensity (measured in counts per second) dependent on the target material and the voltage across the X-ray tube. White radiation is also called bremsstrahlung, German for “breaking radiation”.

The second type of spectra, called the characteristic spectra. In this process radiation is emitted by the electrons of the anode atoms when incoming electrons from the cathode knock electrons near the nuclei out of orbit and they are replaced by other electrons from outer orbits. Each of these electronic transitions produces an X-ray with a wavelength that depends on the exact structure of the atom being bombarded. A transition from the L - shells to the K- shell produces a Kα X-ray, whiles the transition from an M -

shell to the K- shell produces a K_β X-ray. The spectrum of frequencies given off with any particular anode material thus consists of a continuous range of frequencies emitted in the first process, and superimpose on it a number of sharp peaks of intensity corresponding to discrete frequencies at which X rays are emitted in the second process. The sharp peaks constitute the X-ray line spectrum for the anode material and will differ for different materials. [51]

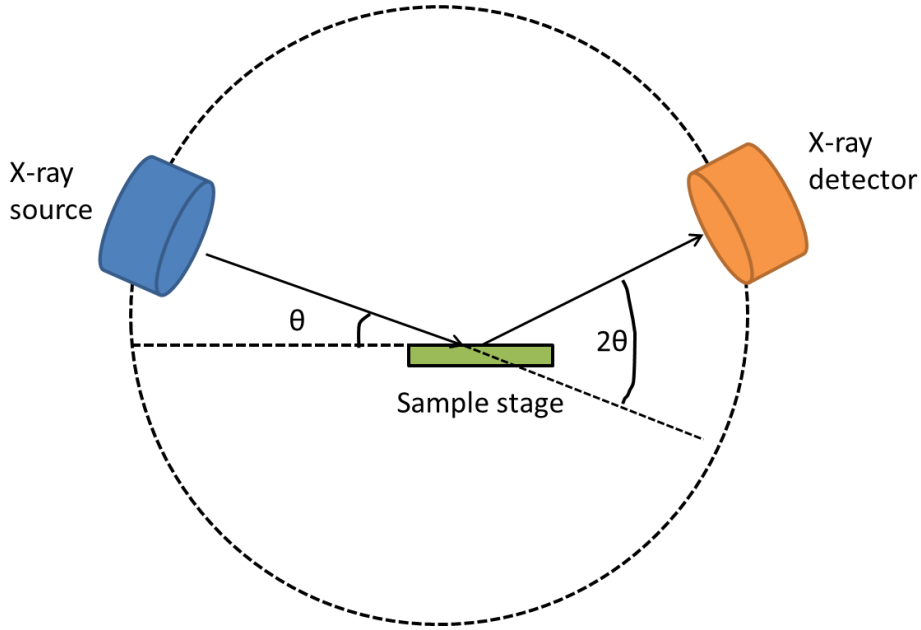

Figure 3-1 Diagram of X-ray diffraction instrument.

The X-rays are then energy selected using a monochromator and guided to the sample using a collimator. A powdered mineral sample is placed on a sample stage so that it can be irradiated by monochromatic X-ray beam. To detect the diffracted X-rays, an electronic detector is placed on the other side of the sample from the X-ray tube, and it is allowed to rotate to produce angles from 0 to 90°. The instrument used to rotate both the X-ray tube and the detector is called a goniometer. The goniometer keeps track of the

angle θ, and sends this information to a computer, while the detector records the rate of X-rays coming out the other side of the sample (in units of counts/sec) and sends this information to the computer.

Bragg's Law

Bragg's scattering, produces diffraction peaks in X-ray diffraction. Bragg diffraction occurs when X-ray is scattered by the atoms of a crystalline material and undergoes constructive interference satisfying the condition given by

$$n\lambda = 2d \sin \theta \quad (3.1)$$

Where n is the positive integer and λ is the wavelength of X-ray, d is the distance between successive crystal planes and Θ is the scattering angle. A schematic of Bragg's scattering is shown in Figure 3-2 below. Each crystalline material has a unique diffraction pattern. This unique diffraction pattern allows identifying crystalline species using XRD.

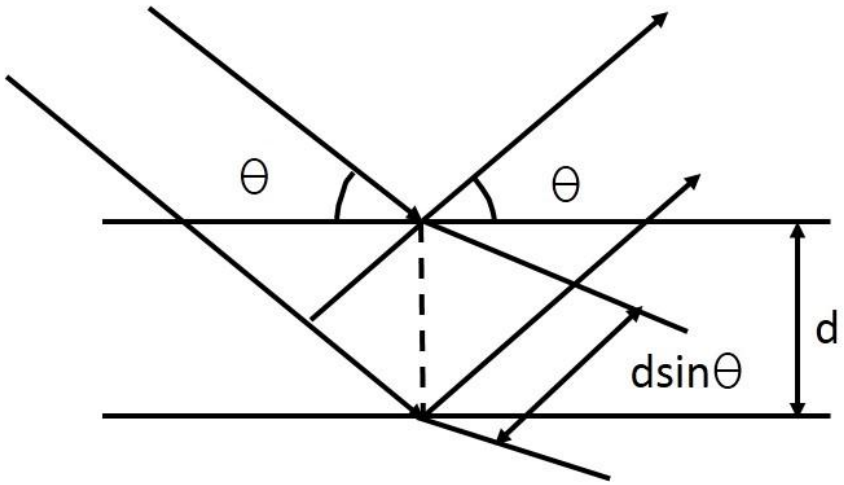

Figure 3-2 Diagram of Bragg scattering in a crystal.

Scherrer Equation

According to Bragg's law, constructive interference at angle θ occurs only at the condition given by equation (3.1). If only Bragg scattered X-rays are detected in the diffractometer, then a delta function should be expected for diffraction peaks at angles where Bragg scattering occurs. However, the diffraction peaks observed in XRD has a finite width. The peak broadening may be due to the instrumental effect, beam divergence, crystal size or the crystal imperfections. In case of large crystal, the distance between two successive crystal planes may not be the same resulting in crystal imperfection. As a result of this some X-rays Bragg diffracts and some do not. Furthermore, X-rays diffracted at different crystal planes would have different path lengths. The difference in path lengths causes destructive interference of the X-rays. If instrumental factors are corrected and considering an ideal crystal with infinite crystal planes, for each X-rays that did not Bragg diffracted, there would always be a crystal plane which diffracts an X-ray resulting in complete destructive interference. Therefore, only Bragg scattered X-rays are detected in the diffractometer resulting in the delta function. Whereas, in case of small crystals there may not be enough crystalline planes for complete destructive interference of the non- Bragg scattered X-rays. Therefore, the contribution of non-Bragg scattered X-ray along with the instrumental error resulting in broadening of diffraction peaks in XRD pattern. If instrumental factors are zero, for a small crystal with diameters below 100 nm, the width of the peak observed in XRD pattern can be used to estimate the size of the crystal. [52] For small crystals, the Scherrer equation given below can be used to relate the full width at half maximum (FWHM) of a diffraction peak at angle θ.

$$D = \frac{K\lambda}{\beta \cos\theta} \tag{3.2}$$

Where, D is the particles size, K is a dimensionless shape factor, λ is the wavelength of X-ray, β is the FWHM value of diffraction peak and Θ is the Bragg angle. Figure 3-3 shows the peak broadening of XRD in case of small size crystal.

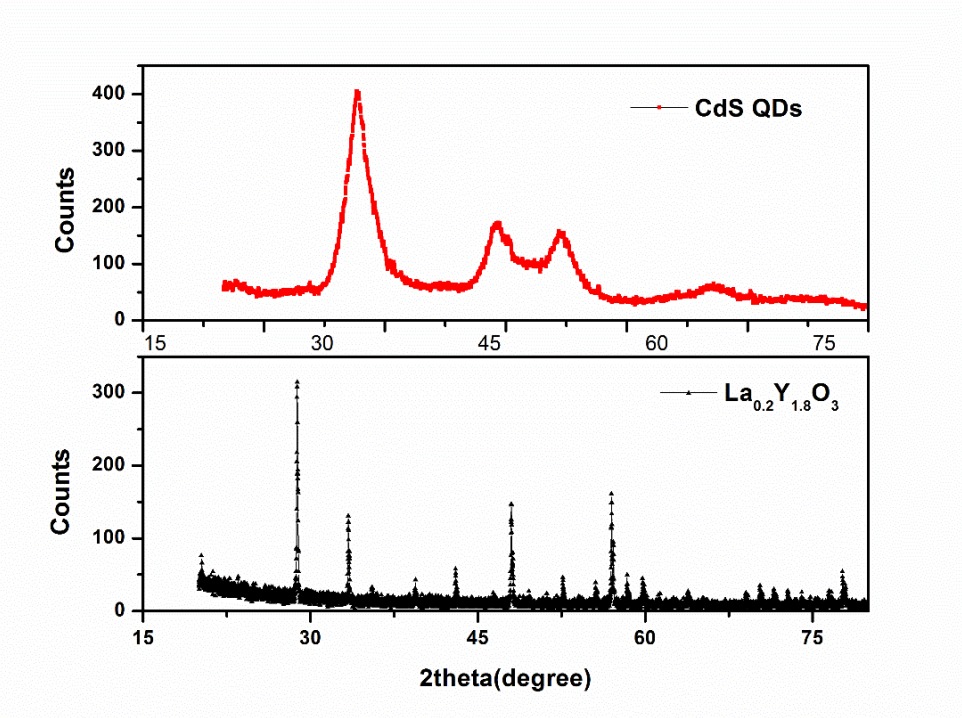

.

Figure 3-3 XRD pattern of CdS quantum dots of about 5 nm (red) and bulk size $La_{0.2}Y_{1.8}O_3$ ceramic (black).

3.3 Transmission Electron Microscopy

Transmission electron microscope (TEM) is an important characterization tool for imaging nanomaterials to obtain quantitative information of particle size and morphology.

TEM images the transmission of a focused electron beam in an ultrathin sample, forming a magnified image in an analogous way to a light microscope. However, TEM is capable of image at a very high resolution compared to light microscope due to the small wavelength of electrons. The block diagram of TEM is shown in Figure 3-4. TEM is enclosed in a vacuum chamber with the air pumped out. Typically, the pressure inside is of the order of 10^{-4} Pa or less. Electron gun is the source of the electron in the TEM. High voltage (typically 100-300 kV) is applied to produce the electron beam in the TEM. There are three main types of electron guns- tungsten hairpin, Lanthanum hexaboride (LaB_6) and field emission gun. Condenser aperture lies directly below the electron gun and helps to clean or maintain the beam size by physically cutting down the beam. The size of this aperture should be chosen, depending on the types of materials. If material is easy to penetrate, then small condenser aperture is good whereas for materials that are hard to penetrate, large aperture is required. Small aperture results in the loss of intensity and vice versa.

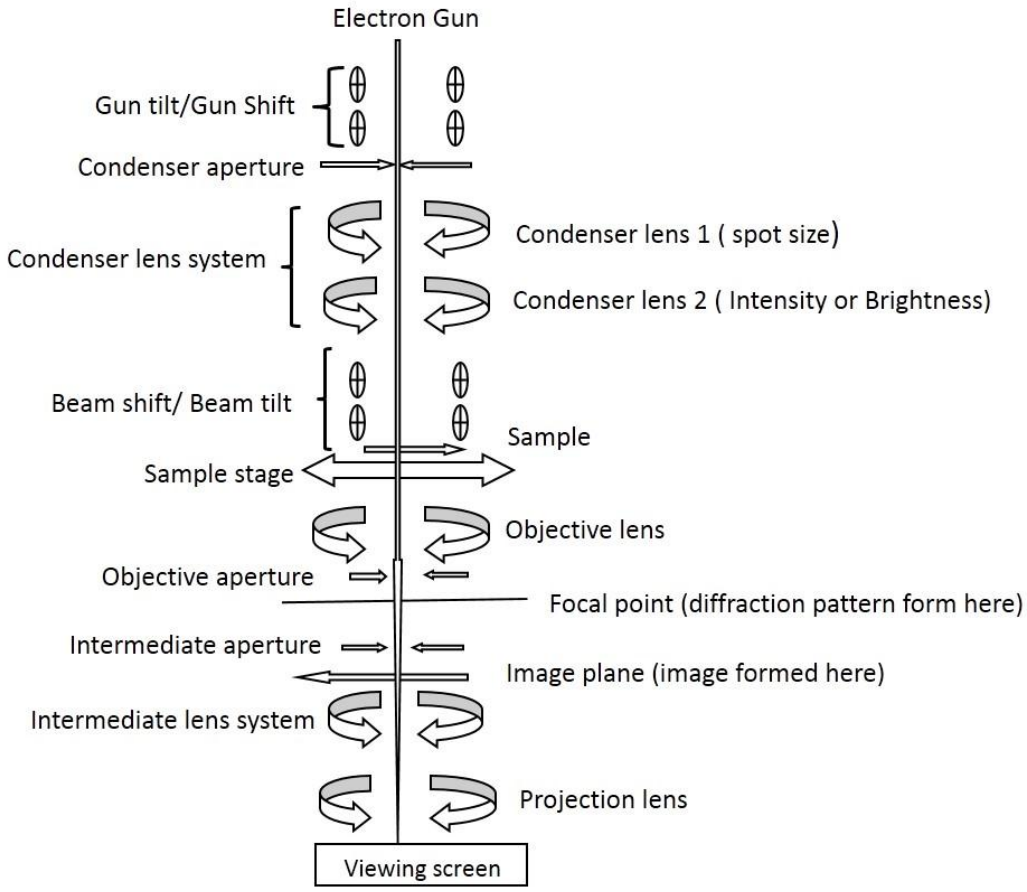

Figure 3-4 Block diagram of a transmission electron microscope.[53]

The electrons are then focused onto the sample by using condenser lens system. Objective aperture also called beam selector helps to select the beam i.e. transmitted beam or diffracted beam. The electrons transmitted through the sample are focused by an objective lens which lies just below the sample stage. The electron beam focus through the objective lens formed image at the front image plane of the objective lens. The image formed at the front image plane of the objective lens is inverted. So, the lens system called intermediate lens is used to flip the as formed image of the sample. Finally, Projection lenses are used to project the image in the screen. Number of projection lenses varies

depending on TEM manufacturer. The electron intensity at the viewing screen is recorded by a charge-coupled device (CCD). Amplitude and phase variation in the transmitted electron beam provide contrast that is a function of the sample thickness and the sample material. Heavier atoms scatter more electrons and therefore have a smaller electron mean free path than lighter atoms.[53] Successful imaging of nanoparticles using TEM depends on the contrast of the sample relative to the background. For nanoparticles imaging, TEM samples are prepared for imaging by drying nanoparticles on a copper grid that is coated with a thin layer of carbon.

In this work, a JEOL 1200 EX S TEM and Hitachi H-9500 high resolution TEM are used. JEOL TEM has an accelerated voltage of 120 kV and a point resolution of 0.34. Hitachi H-9500 is an ultra-high resolution TEM with an accelerated voltage of 300 kV and a point to point resolution of 0.18 nm.

3.4 Scanning Electron Microscopy

Scanning Electron Microscope (SEM) is like a confocal microscope using electron as a probing source, capable of producing high resolution image. The large depth of field that can be obtained in SEM images is one of the most valuable features. SEM can be operated in different imaging mode and each mode can give information about the different properties of the material. SEM images have a characteristic three-dimensional appearance and are useful for judging the surface structure of the sample. SEM is considered as a relatively rapid, inexpensive and non-destructive approach of surface analysis. SEM can be coupled with many analytical instruments such as energy dispersive X-ray analysis (EDX) to perform compositional characterization of the material.

There are three main components of SEM: Electron gun, lens system and imaging system as shown in Figure 3-5. The purpose of electron gun is to produce a stable beam

of electrons of adjustable energy. Typically, electron energy used for SEM ranges from 5KV to 40K V. SEM Lens system consists of three main lenses- condenser lens, objective lens, and scan lens. Electromagnetic lenses are used to demagnify the beam size and to focus the beam on the specimen. The beam current exiting from the gun is first reduced by passing through the pin- hole, and then it passes through the condenser lens system, which condensed the beam to produce the appropriate beam size. The objective lens is used to focus the beam onto the specimen surface and contribute additional demagnification of the beam.

Interaction between the electron beam and sample surface produces emission of electrons from sample surface that will be useful for image formation. These interactions are responsible for a multitude of signal types such as backscattered electrons, secondary electrons, X-rays, Auger electrons, cathadoluminescence. As the beam electrons enter the specimen, they interact as negatively charged particles with the electrical fields of the specimen atoms. The positive charge of the protons is highly concentrated in the nucleus, whereas the negative charge of the atomic electrons is much more dispersed in a shell structure. The beam electron-specimen atom interaction can deflect the beam electrons along a new trajectory without a significant change in the energy of the beam electron (elastic scattering, with no kinetic energy loss). This elastically scattered electron are called backscattered electron (BSE), providing an important class of information for SEM imaging. The probability of elastic scattering increases strongly with atomic number *Z,* approximately as Z^2 because heavier atoms have a much stronger positive charge on the atomic nucleus, and decreases as the electron energy increases, approximately as $1/E^2$. Since BSE are sensitive to atomic weight, backscattered electron imaging (BEI) can be used in case when composition sensitivity image is desired. The backscattered electrons increases with increasing atomic number and so higher atomic number elements will appear brighter in

the image. Elements widely separated in the atomic number will result in the greatest contrast. BEI image can also be used in TOPO (refer to topology) mode. In this mode, backscattered electron intensity is mapped based on the height difference in the sample surface. It is dependent upon the number of secondary electrons and backscattered electrons reaching the detectors after being emitted from different areas of the specimen. Therefore, TOPO mode is useful when enhanced topological information is desired.

Simultaneously with elastic scattering, the beam electrons lose energy and transfer this energy in various ways to the specimen atoms (inelastic scattering), but this transfer takes place gradually so that the beam electrons propagate through many atom layers into the specimen before losing all their energy. This inelastic scattering gives rise to useful imaging signals such as secondary electrons (SE) and analytical signals such as X-ray. Secondary electron emission is fast and extremely sensitive to surface topology, making it ideal for surface image formation. The image formed by the secondary electron are called Secondary Electron image (SEI) and it is typically referred as SEM image.

These electrons signal emitted by the sample surface while scanning is collected by the detectors. There are different detectors to collects different electron signal, like there is a backscattered detector to collect the BSE and a secondary electron detector for the collection of secondary electrons.[54]

In this work, a Hitachi S-500H cold field emission SEM is used. This is an ultra-high resolution SEM with a cold field emission source. It has a resolution of 0.6nm at 30 kV and 3.5 nm at 1 kV in secondary electron image.

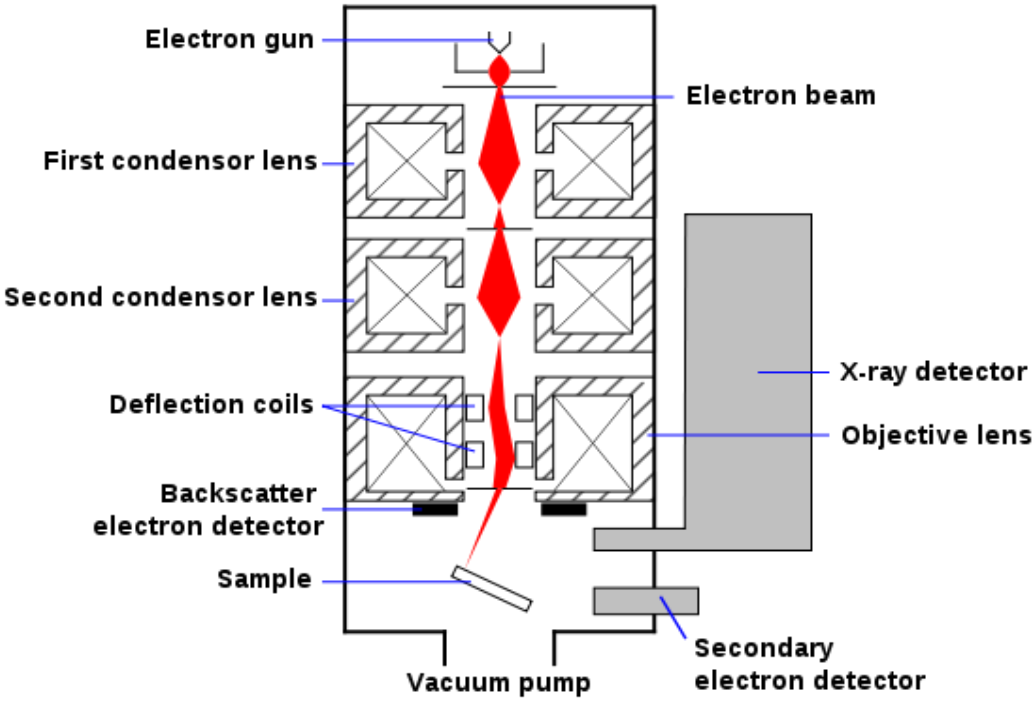

Figure 3-5 Block diagram of scanning electron microscope[54]

3.5 Fourier Transform Infrared Spectroscopy

Fourier transform infrared spectroscopy (FTIR) is a measurement technique, which used infrared radiation to characterize molecular compounds. When the sample is irradiated with infrared, it absorb radiation causing the chemical bonds in the sample to vibrate. The presence of chemical bond is necessary to produced infrared spectrum. Functional groups absorb infrared radiation at a specific wavenumber regardless of the structure of the molecule. Presence of different functional groups can be identified by looking at the different absorption peak in the infrared spectrum.

Michelson interferometer is the main component in FTIR spectroscopy as shown in Figure 3-6. Interferometer is composed of one beam splitter, which can divide the incoming infrared radiation into two beams. The beam splitter transmits one half of the

beam and reflects the other half. The two split beams strike two mirrors; one of which is fixed and the other is movable, and then recombine at the beam splitter after a path difference has been produced. This beam then passes through the sample before reaching the detector. The function of moving mirror is to generate the interference between two reflected beams by changing the distance travelled by one beam. Because of the interference, the intensity of each beam passing to the detector and returning to the source depends on the difference in path of the beams in the two arms of the interferometer. The variation in the intensity of the beams passing to the detector and returning to the source as a function of the optical path difference gives a spectrum called interferogram. An interferogram is the sum of sinusoidal waves with a range of wavelengths and is converted using Fourier transformation to infrared single spectrum.[55]

Fourier transformation is a mathematical tool which transfers information between a function in the time (t) domain and its corresponding frequency (ω) domain and given as

$$F(\omega) = \left(\frac{1}{\sqrt{2\pi}}\right) \int f(t) \exp(-i\omega t)\, dt \qquad (3.3)$$

Fast Fourier transform (FFT) is used to converts the intensity versus path difference spectrum to the intensity versus wavenumber spectrum. It is the spectrum of absorbance or transmittance versus wavenumber. It includes both spectra from the sample and the background. Background spectrum is the spectrum obtained without having sample in the sample holder. This spectrum is from the different parts from the instrument like source, detector, mirror and surrounding environment. To get rid of the signals from instrument itself and different molecules like water, CO_2 present in the environment, this background spectrum is subtracted from the sample spectrum.

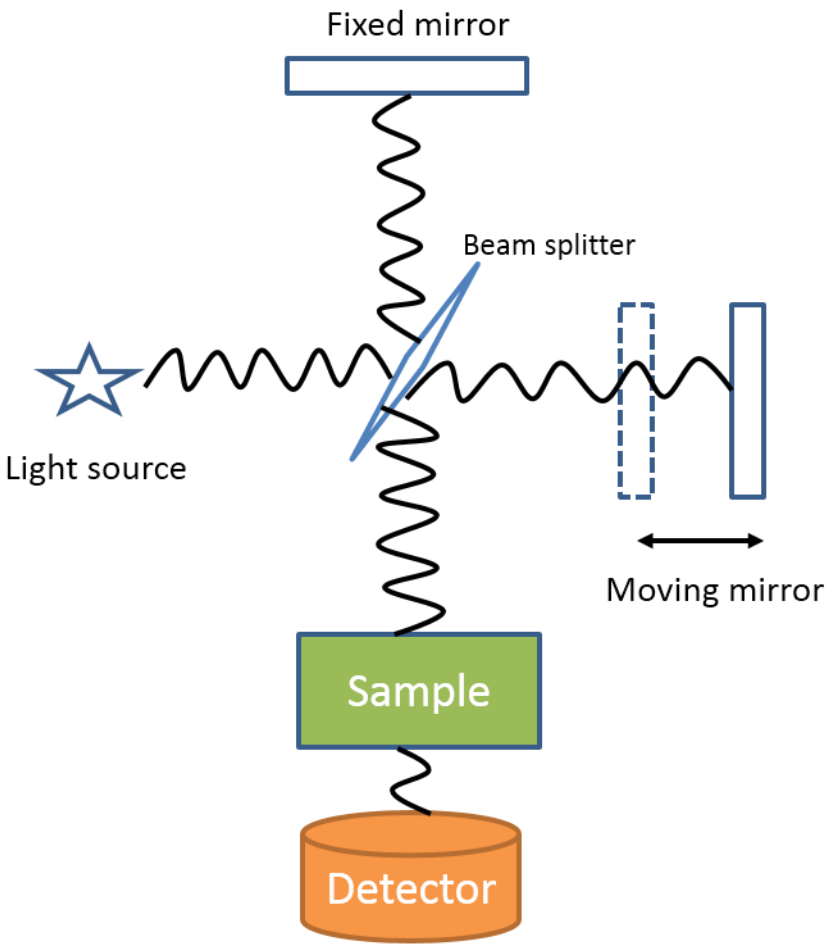

Figure 3-6 Schematic diagram of a Michelson interferometer.

In this work, Thermo Nicolet 6700 FTIR spectrometer is used. This spectrometer is able to collect spectra in the mid-IR, far-IR and near-IR spectral ranges. In this frequency range, absorption peaks due to organic compounds are readily observable.

3.6 Thermogravimetric Analysis

Thermogravimetric analysis is a method of thermal analysis which provide quantitative measurement of mass of a sample as a function of temperature (with constant heating rate) or as a function of time (with constant temperature or constant mass loss). TGA is commonly used to characterize materials that exhibit either mass loss or gain due to decomposition, oxidation, or dehydration. It is an especially useful technique for the study of polymeric materials, including thermoplastics, thermosets, elastomers, composites, plastic films, fibers, coatings and paints. TGA is used for applications such as materials characterization through analysis of characteristic decomposition patterns, study of degradation mechanisms and reaction kinetics, determination of inorganic/organic content in a sample, determination of moisture content in organic and inorganic materials, Oxidative stability, determination of filler content in polymers.

TGA consists of a precise balance loaded with the sample and a programmable furnace. In TGA sample is placed in a small crucible typically made of aluminum or platinum. TGA crucible with sample is balanced with a reference crucible on another balance in a separate chamber. The furnace can be programmed either for a constant heating rate or for heating to acquire a constant mass loss with time. The atmosphere in the sample chamber may be purged with an inert gas to prevent oxidation or other undesired reactions. The furnace is heated electrically and equipped with a thermocouple to monitor accurate measurements of the temperature by comparing its voltage output with that of the voltage-versus-temperature table stored in the computer's memory. [56]The weight of the sample is plotted against temperature or time to illustrate thermal transitions in the material. In this work TGA is used to characterize the amount of organic coating on the surface of inorganic nanoparticles. For this purpose, organic coated inorganic

nanoparticles are heated up to 900 degree Celsius under nitrogen atmosphere. A schematic diagram of TGA is shown in Figure 3-7.

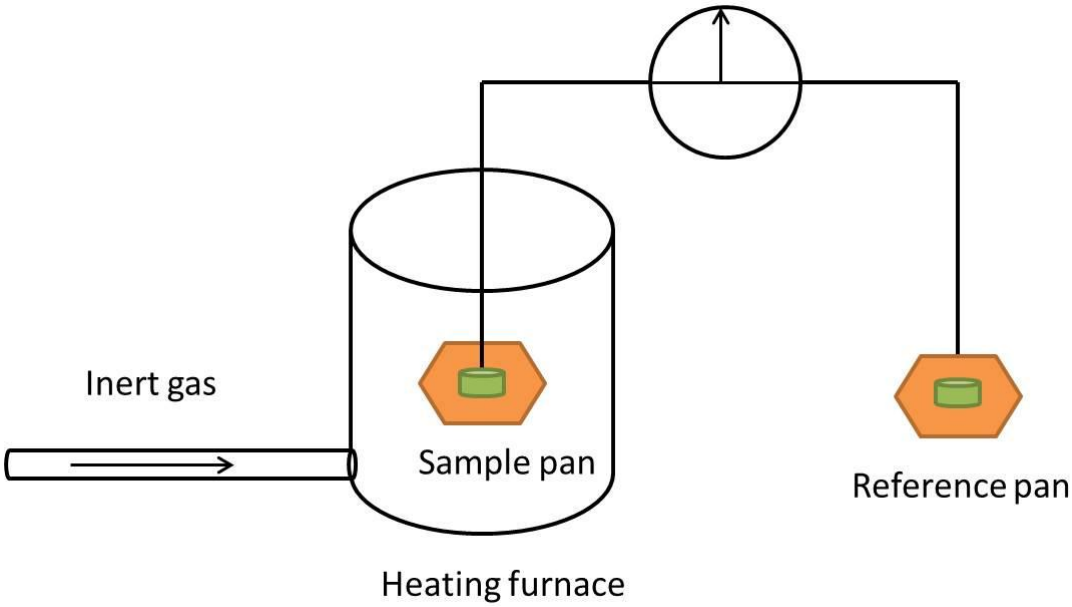

Figure 3-7 Schematic of a thermogravimetric analysis system.

In this work, thermogravimetric analysis instrument from Shimadzu, TGA-50 and SDT Q600 V20.9 Build 20 are used to measure the organic content on the surface of nanoparticles.

3.7 Photoluminescence Spectroscopy

Photoluminescence spectroscopy is a contactless, nondestructive method of probing the electronic structure of materials. Photoluminescence monitors the emission of photons from materials, under photoexcitation. When the sample is excited by photons of a specific wavelength, the sample may absorb the optical photons and photo-excitation can occur. In photo-excitation, valence electrons from the ground state moves to a higher

electronic state. When these electrons return to the equilibrium state, the excess energy is released and includes the emission of light (a radiative process) or may not (a non-radiative process). The radiative transition of electron from excited state to the ground state is divided in to two categories, fluorescence and phosphorescence depending on the nature of the excited state. In excited singlet sates, the electron in the excited state is paired to the second electron in the ground sate orbital. Consequently, return to the ground state is spin allowed and occurs rapidly by the emission of a photon. A typical fluorescence lifetime is in nanosecond. Phosphorescence is the emission of light from excited tripled states in which the electron in the excited state has the same spin orientation as the ground-state electron. Transition to the ground state is forbidden and the emission rates are slow, so that phosphorescence lifetimes are typically milliseconds to seconds. The emission occurs at a lower energy than the absorption because some of the absorbed energy is then dissipated during the process of internal energy transitions such as vibrational relaxation. The energy difference between the maximum of the excitation band and that of the emission band is called the Stokes shift. If the excitation and emission peaks are close together (small stoke shift), then the emission from the sample may be reabsorbed sample itself. This decreases the quantum efficiency of the sample. For scintillation application, it is desirable to have large a stoke shift to minimize self-absorption of luminescence. The emission spectrum (PL) and excitation (spectrum PLE) of $La_{0.6}Ce_{0.4}F_3$ nanoparticles is shown in Figure 3-8. The Stokes shift for $La_{0.6}Ce_{0.4}F_3$ nanoparticles is found to be 38 nm.

In a photoluminescence measurement, both the emission and excitation spectra can be measured. An emission spectrum is the wavelength distribution of the emission, measured at a single constant excitation wavelength. Conversely, an excitation spectrum is the dependence of emission intensity, measured at a single emission wavelength, upon the excitation wavelength. The emission spectrum is measured with a photoluminescence

emission (PL) setup and the excitation spectrum is measured with a photoluminescence excitation (PLE) setup. In PL setup a particular wavelength is selected to excite the sample and the emission is monitored within the specified wavelength range. In case of PLE set up, an emission wavelength is selected to measure the wavelengths of the optical photons that stimulate the emission.

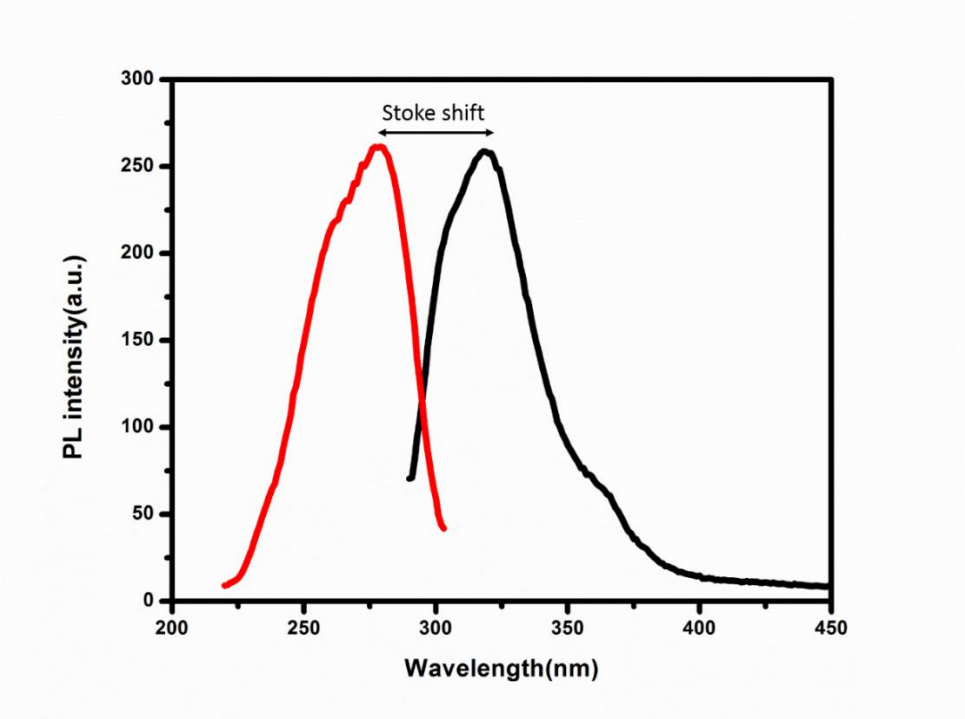

Figure 3-8 Photoluminescence emission and excitation spectrum of La0.6Ce0.4F3 nanoparticle. The stoke shift is about 38 nm.

In this work we used a SHIMADZU RF-5301 PC Spectrofluorometer to measure the PL and PLE of the nanoparticles and nanocomposite scintillators. A block diagram of spectrofluorometer is shown in Figure 3-9. In general, a spectrofluorometer consists of a light source, an excitation monochromator, a sample compartment, an emission monochromator and a detector. A xenon lamp is used as a light source to produce photons

(in the range of 220-990 nm in Shimadzu RF-5301 PC). The light source sends out light at the excitation wavelength of a sample. Before it reaches the sample, the light passes through the excitation monochromator, which transmits a wavelength selected for the excitation spectrum measurement while blocking other wavelengths. The light from the excitation monochromator passes through the sample contained in the sample compartment and excites the sample. Following excitation, the sample emits light at an emission wavelength longer than the excitation wavelength. The emitted light passes through the emission monochromator positioned at a right angle to the excitation light. The emission monochromator minimizes light scatter and screens the emission light before it reaches the detector. The detector measures the emitted light and displays the fluorescence spectrum of the sample.[57]

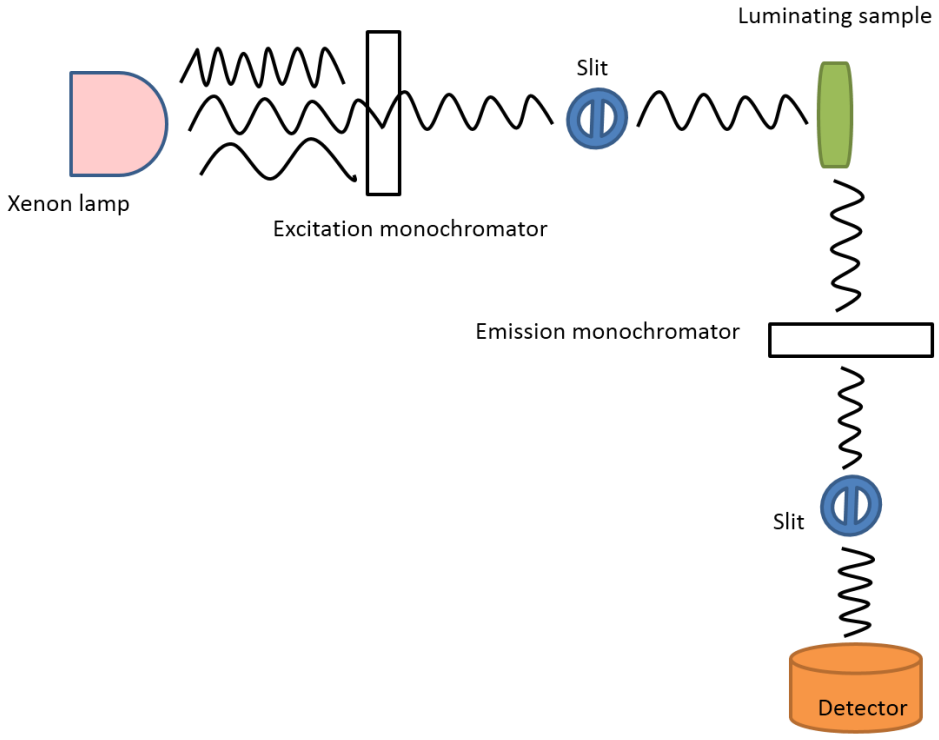

Figure 3-9 Block diagram of a typical spectrofluorometer.

3.8 Ultraviolet-Visible Spectroscopy

Ultraviolet-Visible spectroscopy (UV-Vis) is an optical characterization tool used to measure the photon absorption in a sample in the ultraviolet-visible spectral range. This technique measures the electronic transitions form the ground state to the excited state and is complimentary to fluorescence spectroscopy. In this work, SHIMADZU UV-2450 spectrophotometer is used to measure the absorption and transmittance of the nanoparticles, scintillating dye and nanocomposite scintillators. In general, an UV-Vis spectrophotometer contains, an electromagnetic radiation source, diffraction grating, sample cell and a detector. A combination of a deuterium lamp for the UV region of the spectrum and tungsten or halogen lamp of the visible region is used to cover the entire UV-Vis spectral range. Light from the UV-Vis light source is separated in to its component wavelengths by a diffraction grating and slit. By moving the dispersing element or the exit slit, radiation of only a selected wavelength leaves the monochromator through the exit slit. The wavelength selected light is then divided into two separate paths by a beam splitter, where one of the light beams passes through the sample and the other passes through the reference sample in the sample cell. The reference sample contains only the solvent used for dispersing the sample. The two light beams are then collected and compared using a detector. The detector is typically a photomultiplier tube, a photodiode, a photodiode array or a charge-coupled device (CCD). The intensity the sample cell (I), intensity of the reference cell (I_0) and absorbance (A) for the given wavelength is related by Beer-Lambert law given as

$$A = -\log\left(\frac{I}{I_0}\right) \tag{3.4}$$

The absorbance calculated is corresponds to a given wavelength and the UV-Vis spectrophotometer repeat this procedure for the entire range of selected wavelengths to produce a spectrum of absorbance vs wavelength.[58] For accurate measurement of absorption, it is required that the concentration of the sample is low to avoid any discrepancies due to light scattering. A schematic of UV-Vis spectrophotometer is shown in Figure 3-10.

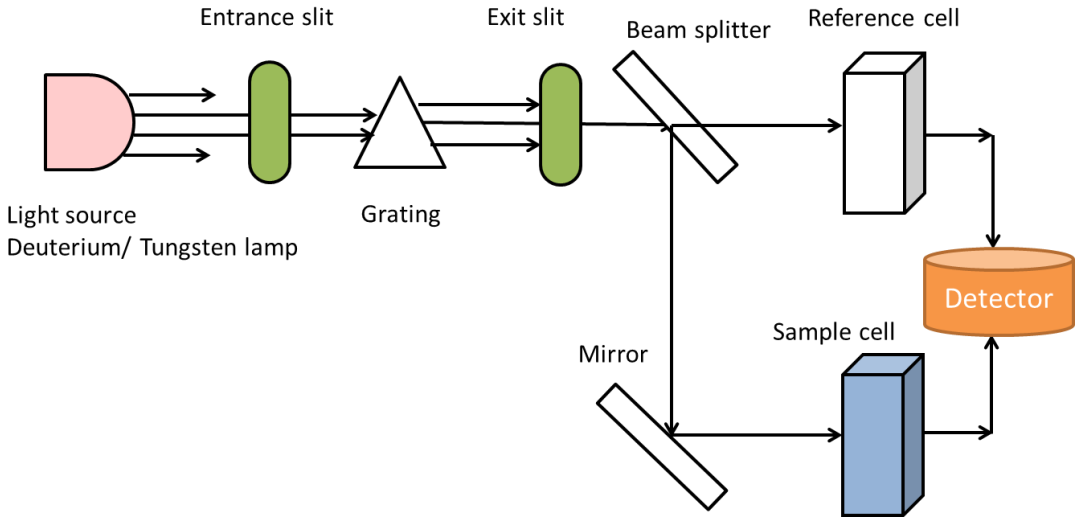

Figure 3-10 Schematic of a UV-Vis spectrophotometer.

3.9 X-ray Excited Optical Luminescence

X-ray excited optical luminescence (XEOL) is an optical characterization technique in which photoemission from the sample is measure under X-ray irradiation. In this work, RX-650 Faxitron X-ray cabinet system is used for X-ray irradiation. The outline drawing of Faxitron Standard X-ray tube is shown in Figure 3-11. It consists of an X-ray tube along

with an X-ray generator to supply the X-rays. Current is fixed at 3 mA. The acceleration voltage can be tuned with a maximum value of 130 kV_p. The current supplied by the X-ray generator is used to heat up a filament to produce the electrons. The electrons are then accelerated through the high voltage to bombard a tungsten target producing both characteristic and bremsstrahlung X-rays. The angle of the anode is 20 ° and the focal spot size is 0.5 mm. The X-ray tube is equipped with a 0.76 mm beryllium window to allow a full spectrum of soft X-ray output.

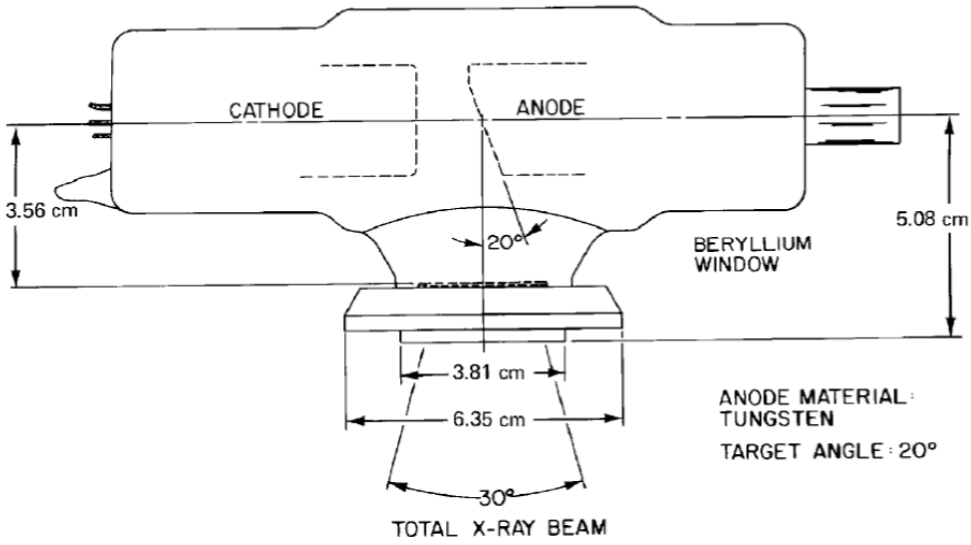

Figure 3-11 An outline diagram of Faxitron standard X-ray tube.[59]

The X-rays will excite the sample and the sample gives out luminescence upon de-excitation and the luminescence spectra were recorded using QE65000 spectrometer from Ocean Optics Inc. coupled to the X-ray cabinet. The spectrometer separates the light into individual wavelength components using a grating monochromator and the intensity of the individual wavelength components is then recorded by a charge-coupled device.

Typically, X-ray tube is operated with 3 mA current and 90 kVp voltage. The output from a typical XEOL experiment is the intensity distribution of the scintillation light versus wavelength as shown in Figure 3-12.

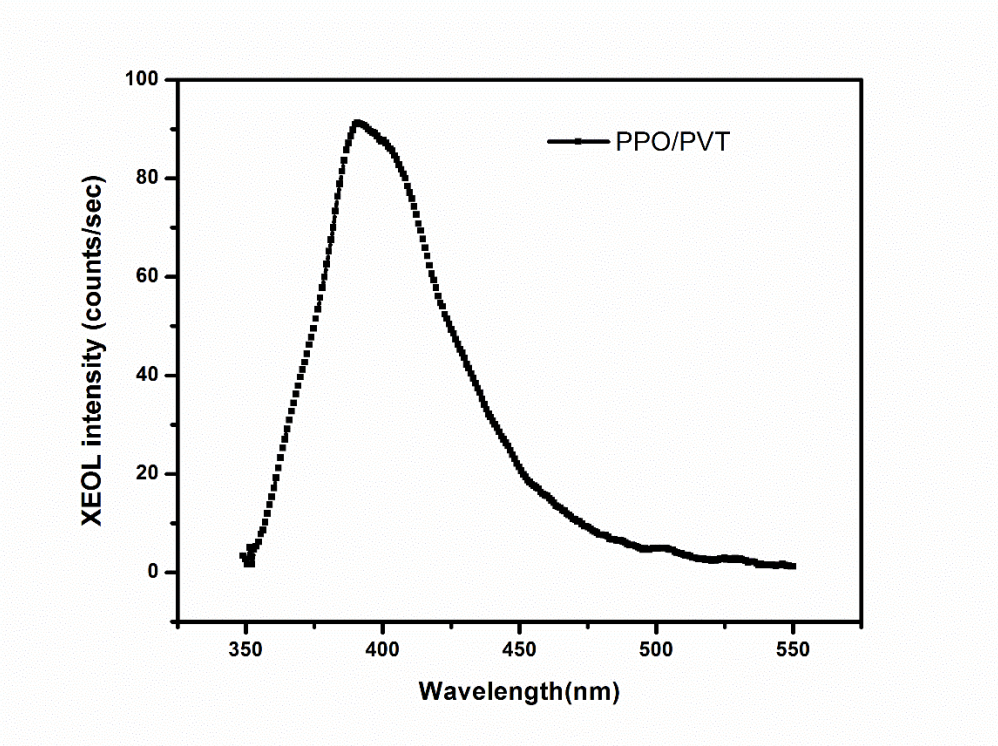

Figure 3-12 XEOL spectrum of PPO embedded in PVT matrix.

3.10 Gamma ray spectroscopy

Gamma ray spectroscopy is the study of energy spectrum of gamma-ray sources produce by the scintillator materials. Gamma ray spectroscopy requires a scintillator, preamplifier, an amplifier, High voltage supply and a multichannel analyzer. The block diagram of gamma ray spectroscopy setup is shown in Figure 3-13. To detect scintillation photons, a scintillator is attached to the base of the photomultiplier tube using optical gels to minimize the photons loss.

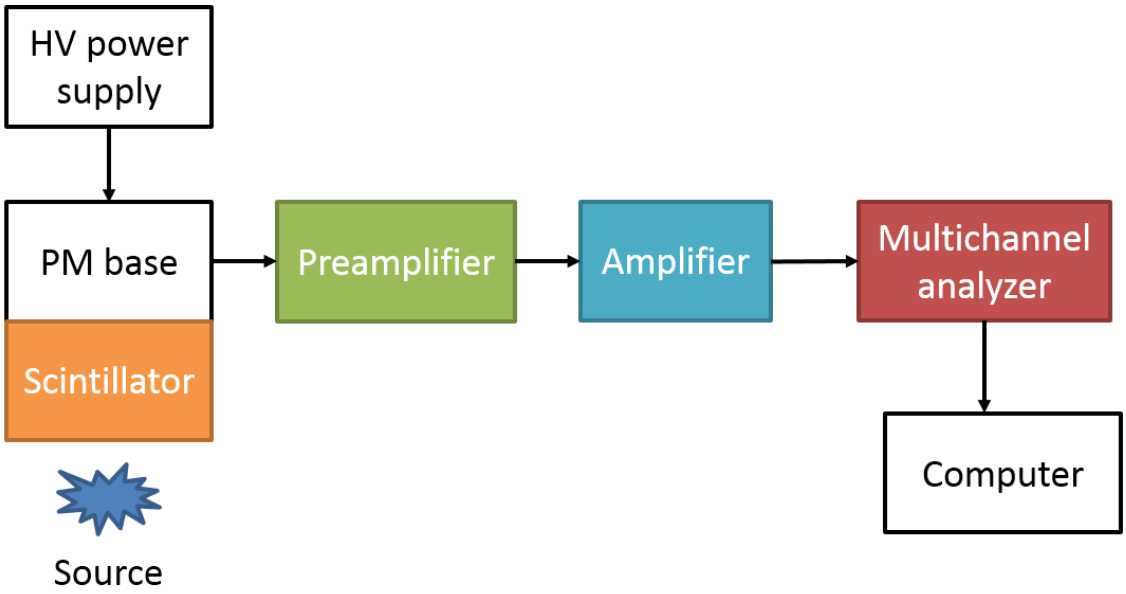

Figure 3-13 Block diagram of a gamma ray detector.

The photomultiplier is connected to the high voltage power supply to accelerate the electrons created as a result of gamma ray interaction with the scintillator. The details of gamma ray interaction with scintillator and electron multiplication with photomultiplier tube has been discussed in chapter 2. The anode of photomultiplier is connected to a charge-sensitive preamplifier which converts the current pulse to a voltage pulse with amplitude proportional to the amount of energy deposited by gamma source into the scintillator. The preamplifier is connected to an amplifier which amplifies and shapes the gamma ray pulse to meet the requirement of the pulse height analysis instrumentation that is connected to the amplifier. The main amplifier accepts the low-voltage pulse from the

preamplifier and amplifies it into a linear voltage range that is 0 to 10V for most high-quality amplifiers. The amplified pulses are shaped to optimize the signal –to-noise ratio and to meet the pulse-shape requirements of the pulse-height-analysis electronics. The output of the amplifier is connected to a multichannel analyzer (MCA) operating in the pulse-height analysis mode. A pulse height analyzer or a MCA measures the height of each input pulse. The analog-to-digital converter (ADC), performs the pulse-height analysis in the MCA. The analog voltage pulse from the amplifier is converted in to a binary number that is proportional to the amplitude of the input pulse. A maximum positive height of the pulse is set in the MCA using ADC and channel number for each pulse can be calculated using the height of the pulse. The pulse height analyzer then counts the number of pulse in each channel and a plot of the counts in each channel versus the channel number to produce the distribution of the pulse heights.

In this work, The scintillation response was measured using a super bi-alkali Hamamatsu PMT R6231-100 biased at 900V. PMT output was further amplified with Hamamatsu preamplifier C6438 and shaped with a spectroscopy Ortec amplifier Model 671. Multi-channel analyzer was a Canberra MPII. For some measurement, Ortec model 113 preamplifier, Ortec-575 as amplifier and Ortec MCA 926 multichannel analyzer were used. Scintillation timing was measured using gamma excitation (Cs-137) and PMT at 900V and output of the preamplifier applied to a digital oscilloscope (Picotech).

Chapter 4

Optical and Scintillation Properties of CeF_3 Nanoparticles and CeF_3/ZnO Nanocomposite

4.1 Introduction

A good scintillator should have a fast decay time for time resolution, high light yield for energy resolution and high density for high stopping power[60-62]. Extensive researches have been done on the scintillator development based on the application of Ce^{3+} ion as a luminescence center. The allowed 5d-4f transition in Ce^{3+} ion makes Ce^{3+} doped luminescence materials fast and efficient scintillators[63]. However most of the researches are done on the single crystals. Single crystals are expensive to grow in desire shape and size. Also most Ce^{3+} ion activated scintillators emit in the ultraviolet (UV) region at which the quantum efficiency of photomultiplier tubes (PMTs) is below 25%[64]. This could significantly reduce the light output and the detection sensitivity.

Cerium Fluoride (CeF_3) single crystal is known as heavy inorganic scintillator. It was discovered as a scintillator material in 1989 by W.W. Moses and S. E. Derenzo.[65] CeF_3 has hexagonal phase structure, high density (6.16 g/cm^3), non-hygroscopic and transmitting light from 300 nm to 5000 nm.[66] CeF_3 single crystal shows dominant emission band with peak at about 340 nm. This emission is due to 5d-4f transition in Ce^{3+} ion. CeF_3 has light yield of 4000 ph/MeV and a fast decay time of 27 ns. High density and fast decay time make CeF_3 a promising scintillator material.

The development of nanotechnology has open up a new field in materials research. Nanoparticles can be synthesized using easy techniques resulting in particles with at least one dimension less than 100 nm. Small size of the nanoparticles helps reducing the light scattering when embedded in polymer matrix. Moreover, ease of fabrication makes nanoparticles a cost effective alternative to single crystals. Nanoparticles can also be doped with other ions to tune the optical properties. Nanoscale luminescence

materials are potential scintillators for radiation detection and preliminary investigations on several rare earth doped fluoride nanoparticles have indicated their potentials for radiation detection[67]. Mckigney et al. reported the enhancement in light yield of YSO-Ce nanophosphors compared to its bulk counterpart under X-ray excitation.[38]

Nanoparticles of semiconductor also called quantum dots (QDs) shows size dependent optical properties. In addition to tunable emission, QDs also reported to have very high quantum efficiency The unique physical properties of Semiconductor nanocrystals (Quantum dots) have attracted tremendous interest in wide range of application from medical imaging[68, 69], biosensing[70], optoelectronic devices[71] to solar cells[72]. Recently, radiation detection has emerged as an area of interest for quantum dots (QDs) application[73]. However, there have been very few published studies on the radiation detection based on colloidal QDs. For examples, It has beenreported that scintillation performance of luminescent polymer has been improved in CdSe/ZnSe core-shell QDs/ polymer composite under electron-beam excitation using cathodoluminescence[42] and that the energy resolution of CdSe/ZnS core-shell QDs/glass nanocomposite is increased over a standard NaI scintillator by the factor of 2 when irradiated with 59 keV gamma ray[36]. Quantum dots based nanocomposite materials could be a promising material for radiation detection because of their short luminescence life time and high quantum efficiencies as a consequence of quantum size confinement[74]. Also, the emission of quantum dots is size dependent, so the output wavelength can be tuned to the sensitivity of the PMTs or avalanche photodiodes (APD). However, the stopping power of most QDs is low and their scintillation luminescence is very weak[75]. The combination of high stopping power of inorganic scintillator with QDs could potentially lead to a new class of scintillator. Recently, we have reported that energy

transfer based nanocomposites are new and promising scintillators for radiation detection[73, 75].

Zinc Oxide (ZnO), a wide band gap (3.37 eV) semiconductor with large exciton binding energy (60 meV) has been known as a fast scintillator[76]. However it has relatively low light yield[77] and low density. The nanocomposite scintillators based on energy transfer from Ce^{3+} doped nanoparticles proposed by us [[75], [73]] could overcome these shortcomings.

In this chapter we report the synthesis and optical studies of CeF_3 nanoparticles and CeF_3/ZnO nanocomposites. We have used easy one step wet chemistry method to synthesis CeF_3 nanoparticles. Poly ethylene glycol bis(carboxymethyl) ether as a surface coating agent. To overcome the detection limitation of Ce^{3+} emission of CeF_3 using PMT we synthesized CeF_3/ZnO nanocomposite and studied the optical and scintillation properties of nanocomposite.

4.2 Experimental

4.2.1 Synthesis of PEG coated Cerium Fluoride (CeF_3) Nanoparticles

CeF_3 nanoparticles were synthesized using easy one step wet chemistry method as shown in Figure 4-1. First, 2 mmole of cerium nitrate hexahydrate is dissolved in 40 ml DI water. 400 µl Poly (ethylene glycol) bis(carboxymethyl) ether is added as a surfactant to the nitrate solution and then stirred at room temperature for 15 minutes. In another beaker 1 ml hydrofluoric acid is mixed with 39 ml of DI water and then added dropwise to the above slurry and then kept stirring at room temperature for 30 minutes. After 30 min of stirring, the mixture is heated for 2 h and 30 m at 95 ˚C. CeF_3 nanoparticles were then centrifuged, washed with DI water for several times and dried overnight at 45˚c under vacuum.

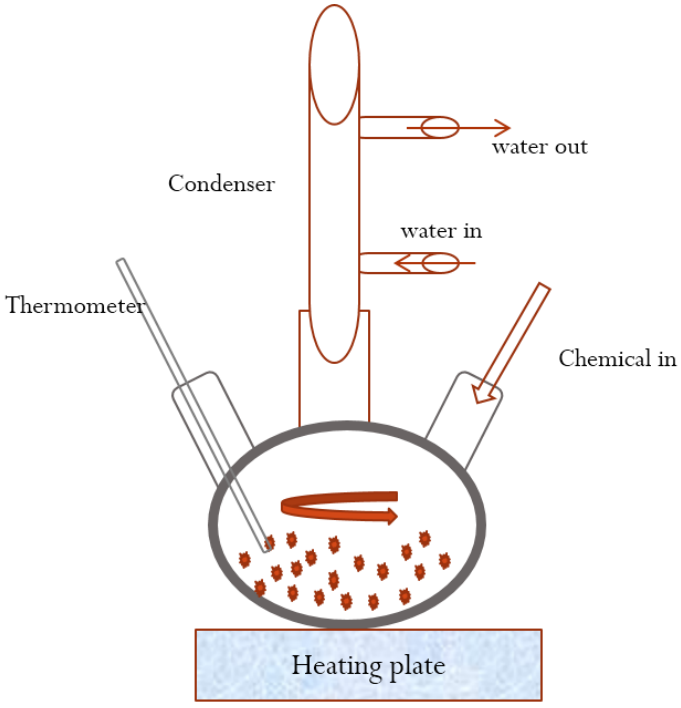

Figure 4-1 Schematic of wet chemistry synthesis method.

4.2.2 Cerium Fluoride/ Polyvinyl Alcohol (PVA) Nanocomposite

PVA beads were dissolved in water by heating up to 70°C to make PVA gels. Desire amount of CeF_3 nanoparticles were dispersed in water and added to PVA gels. The nanoparticles were mixed in PVA gels using vortex mixture and ultra-sonication. Finally the nanoparticles/PVA gels are cast on the petri dish and dry at 40 °C for 24-36 hours.

4..2.3 Cerium Fluoride Semitransparent Disc

The as synthesis CeF_3 nanoparticles were dry and grind using mortar and pestle. The powders were pressed into green body using Specac hydraulic pressing system to obtain a semitransparent disc of CeF_3 nanoparticles. Semitransparent disc of CeF_3 nanoparticles were tested for radiation detector.

4.2.4 Synthesis of Zinc Oxide (ZnO) Nanoparticles

The colloidal ZnO nanoparticles were synthesized in methanol using similar method reported by Sun et al[78]. To synthesize ZnO nanoparticles, 0.08 M potassium hydroxide in methanol is refluxed and stirred for 30 min at 60 ˚C. After refluxing, 0.04 M Zinc acetate dihydrate (ZAD) in methanol is added dropwise while stirring. The ZnO sol was then aged at 60˚c for 2 h with continuous stirring and refluxing. The colloidal ZnO nanoparticles appear clear under room light but emit green under UV-light.

To synthesize the colloidal ZnO nanoparticle in ethanol, 1mmole Zinc acetate dehydrate is dissolved in 20 ml ethanol by heating to 60 ˚C. In another beaker 3mmole potassium hydroxide (KOH) is dissolved in 20 ml ethanol by heating the solution to 50 ˚C. Now, KOH- ethanol solution is added dropwise to ZAD-ethanol solution and then kept stirring for 1 h at room temperature. The as obtained ZnO nanoparticles are well dispersed in ethanol.

To synthesize ZnO nanoparticles in water/ethanol mixture, firstly 0.5 ml oleic acid as a surfactant is dissolved in 20 ml ethanol. Secondly, 1.5 mmole zinc nitrate hydrate is dissolved in 40 ml DI water and added to the oleic acid-ethanol solution dropwise at room temperature. Finally 4 mmole sodium hydroxide (NaOH) is dissolved in 15 ml water and added dropwise to the above solution at once while stirring and then heated at 80 ˚C for 1 h. The resulted powder is washed with toluene and ethanol mixture several time to remove all the impurities.

ZnO nanoparticles in water (ZnO-W_1) is synthesized by first dissolving zinc acetate in 10 ml DI water. In another beaker 2mmole KOH is dissolved in 40 ml DI water and added dropwise to the zinc acetate solution. Finally, 100 µl polyethylene glycol is added and stirred at room temperature for 30 min. After stirring for 30 min, the solution is added to an

autoclave and heated at 120 ˚C for 6 hrs. The as obtained sample is washed several times with water and ethanol before drying in oven.

Another sample of ZnO nanoparticles in water (ZnO-W_2) is synthesized by dissolving, 1 mmol zinc acetate in 20 ml DI water. In another beaker 2 mmol KOH is dissolved in 100 ml DI water. NaOH solution is heated to 50 ˚C and zinc acetate solution is added dropwise to NaOH heated solution. Finally 120 µl thioglycerol is added and the solution is stirred at room temperature for 3 h. The precipitate is separated using centrifuged and washed several times with water and ethanol.

4.2.5 Synthesis of CeF_3/ (ZnO) Nanocomposite

CeF3/ZnO nanocomposite scintillators were prepared using a two-step wet chemistry synthesis. First, CeF_3 and colloidal ZnO nanoparticles were synthesized as mention above. Secondly, the as prepared CeF3 nanoparticles were added to the colloidal ZnO nanoparticles and ultra-sonicated for 10 min. Hexane and isopropanol were added to the CeF_3/ZnO sol and kept it in refrigerator overnight to precipitate. The volume ratio of colloidal ZnO nanoparticles: isopropanol: hexane was 1:1:5. The product was centrifuged and then dries at 45 ˚c under vacuum.

4.2.7 Zinc Oxide/ PMMA Nanocomposite

First, 0.1 M zinc acetate dihydrate (ZAD) is refluxed in ethanol at 80 °C for two hours under magnetic stirring. 600 µl monoethanolamine (MEA) is added to the refluxed ZAD ethanol solution and stirred at 80 °C for 10 mins. 1ml of the above solution, and 2,2′-azobisisobutyronitrile (AIBN) is added to 2 ml methyl methacrylate (MMA) in a glass vial and mixed it using ultra sonication and vortex mixture. After mixing, the glass vial is

incubated at 70 °C for 36 h. The final ZnO/PMMA monolith can be obtained by cooling down to room temperature and breaking the glass vial carefully.

4.2.8 CeF3/ZnO/PMMA Nanocomposite

To synthesize CeF_3/ZnO/PMMA nanocomposites, CeF_3 nanoparticle, AIBN and refluxed solution of ZAD and MEA is added to MMA in a glass vial and mixed it using ultra-sonication and vortex mixture. After mixing, the glass vial is incubated at 70 °C for 36 h. The final CeF3/ZnO/PMMA monolith can be obtained by cooling down to room temperature and breaking the glass vial carefully.

4.2.9 Materials Characterization Instrumentations

After drying for overnight, ZnO nanoparticles, CeF3 nanopartcles and CeF3/ZnO nanocomposites were examined by X-ray diffraction (Cu Kα X-ray). The particles size was estimated using Scherer's equation. Transmission electron microscope (JEOL 1200EX) was used to determine the size of nanoparticles. Optical absorption of colloidal ZnO and CeF_3 nanoparticles were recorded with SHIMADZU UV-2450 spectrophotometer. Photoluminescence emission (PL) and excitation (PLE) were taken on a SHIMADZU RF-5301 PC Spectrofluorometer. Fourier transform infrared spectroscopies (FTIR) studies were performed using Thermo Nicolet 6700 FTIR spectrometer X-ray luminescence was measured in a light-proof X-ray cabinet equipped with optic fiber connection to an outside detector. X-ray irradiation (90 kV and 5 mA) was performed using a Faxitron RX-650 X-ray cabinet (Faxitron X-Ray Corp, IL, USA). The luminescence spectra were recorded using a QE65000 spectrometer (Ocean Optics Inc, Dunedin, FL), connected to the X-ray chamber using a 600 μm core diameter, P600-2-UV-Vis fiber optic (Ocean Optics Inc, Dunedin, FL. The scintillation response to gamma source was measured using a super bi-

alkali Hamamatsu PMT R6231-100 biased at 900V. PMT output was further amplified with Hamamatsu preamplifier C6438 and shaped with a spectroscopy Ortec amplifier Model 671. Multi-channel analyzer was a Canberra MPII.

4.3 Results and Discussion

4.3.1 PEG coated CeF_3 nanoparticles

Photoluminescence of as synthesized CeF_3 nanoparticlesis measured in water and in powder form. Photoluminescence measurement shows no significant change in emission and excitation spectra of CeF_3 nanoparticles in water and powder.

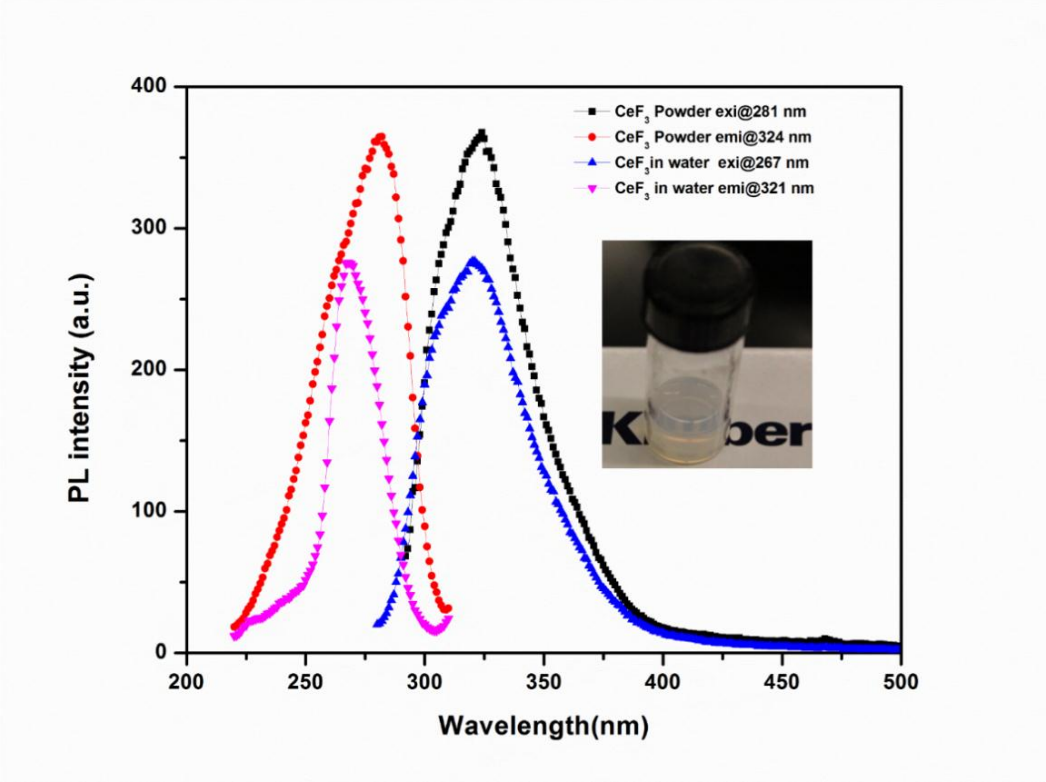

Figure 4-2 Photoluminescence emission (PL) and excitation (PLE) of PEG coated CeF3 powder and in water. Inset shows the 30 wt% CeF3 nanoparticles in 1ml water.

In water, CeF_3 shows emission with peak at 321 nm when excited at 267 nm. This emission is due to the *5d-4f* transition of Ce^{3+} ion.[79] In CeF_3 single crystal, emission at about 340 nm has been reported by different authors. The shift in emission may be due to the surface defects in CeF_3 nanocrystals as a result of low temperature synthesis. In powder sample, the photoluminescence peak is shifted by 3 nm as shown in Figure 4-2. Phase structure of the as synthesized CeF_3 nanoparticles is characterized using X-ray diffraction (XRD). XRD pattern of CeF_3 nanoparticles matches well with the JCPDS 8-45 profile for CeF_3 with hexagonal phase structure as shown in Figure 4-3. The size of the nanoparticles is estimated using Scherrer's equation (3.2). The XRD peak (300) is used to estimate the size of the nanoparticles.

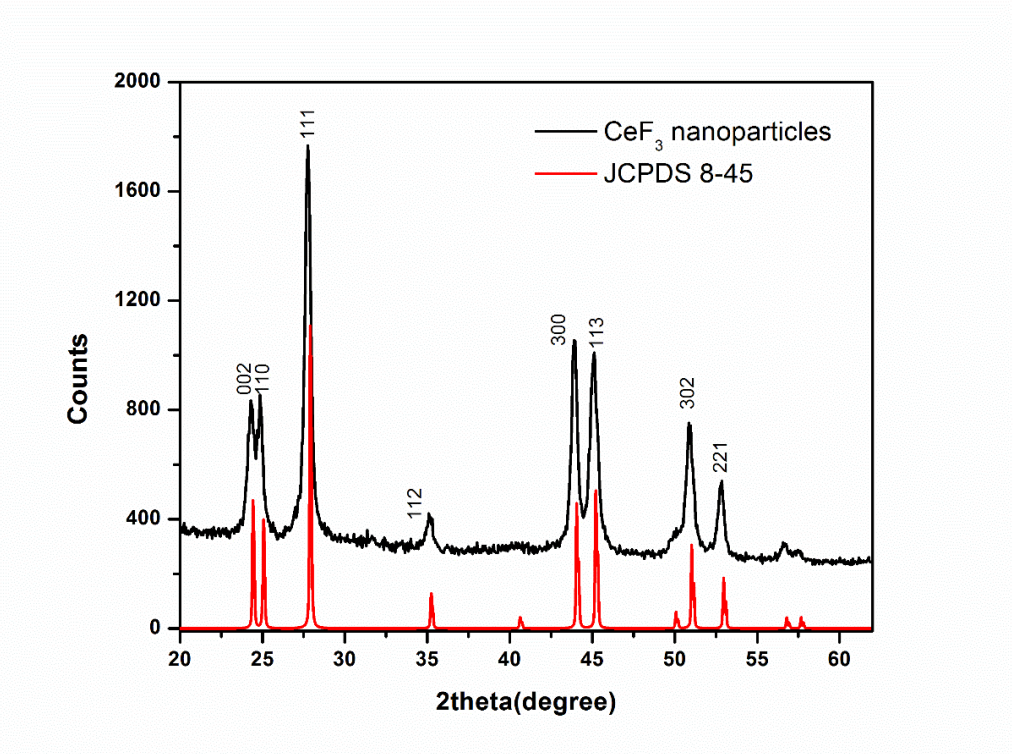

Figure 4-3 XRD pattern of as synthesized CeF3 nanoparticles and JCPDS 8-45 as a reference profile.

The estimated size of the nanoparticles is 30 nm. Transmission electron microscopy (TEM) image is obtained to confirm the size of the nanoparticles. TEM image in Figure 4-4 shows the nanoparticles with average size of about 30 nm, with some large nanoparticles of about 50 nm. As synthesis CeF_3 nanoparticles is highly dispersible in water. The inset in figure 5.1 shows the 30 wt% CeF_3 nanoparticles dispersed in 1ml water. Figure 4-5 shows the UV-Vis absorption spectrum of PEG coated CeF_3 nanoparticles. Four peaks were detected from 200-250 nm are associate with the 4f-5d transitions. Multiple peaks correspond to the splitting of $4f^1$ ground state into $^2F_{5/2}$ and $^2F_{7/2}$ due to spin-orbit interaction. Also the spin-orbit interaction cause splitting of 5d energy level into five levels as reported in the past.[80, 81]

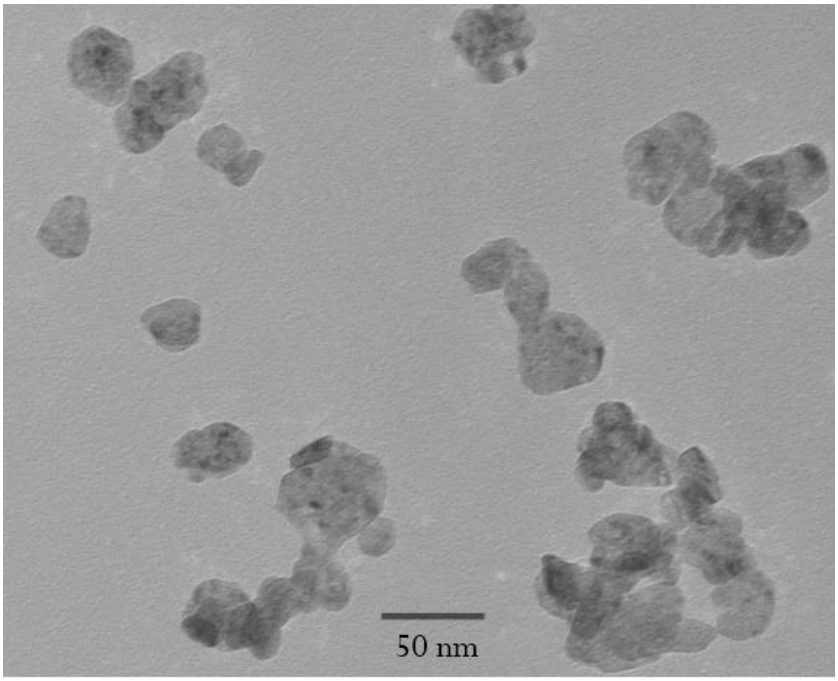

Figure 4-4 TEM image of PEG coated CeF3 nanoparticles.

Figure 4-6 shows the X-ray excited optical luminescence (XEOL) of PEG coated CeF_3 nanoparticles. XEOL spectrum shows peak at around 300 nm and a shoulder at 324 nm. It has been reported that the peak at 300 nm is attributed to the transition from lowest 5d energy level to ground 4f energy level. The emission at 324 nm has been reported as emission due to the perturbed Ce^{3+} ions. The perturbation could be due to the defects or impurities arises as a result of organic surfactant.[12] It has been reported that the CeF_3 crystal shows dominant emission at 340 nm under gamma-excitation.[12]

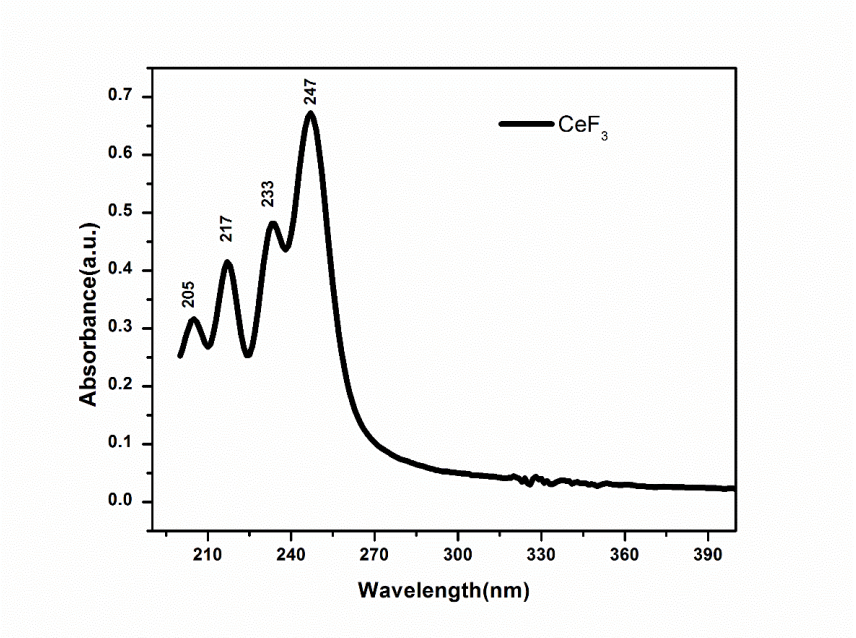

Figure 4-5 UV-Visible absorption spectrum of PEG coated CeF3 nanoparticles.

The fluorescence quantum yield (QY) of a fluorophore is the ratio of photons absorbed to the photons emitted through fluorescence. The QY of a fluorophore is determined relative to a reference compound of known QY. If the same experimental

condition are maintained for absorption and emission measurements for the two samples then the QY is calculated as

$$\Phi_x = \Phi_{st}\left(\frac{Grad_x}{Grad_{st}}\right)\left(\frac{\eta_x^2}{\eta_{st}^2}\right) \quad (4.1)$$

Where, the subscripts st and x denote standard and test sample respectively, Φ is the fluorescence quantum yield, Grad is the gradient form the plot of integrated fluorescence intensity versus absorbance and η is the refractive index of the solvent.

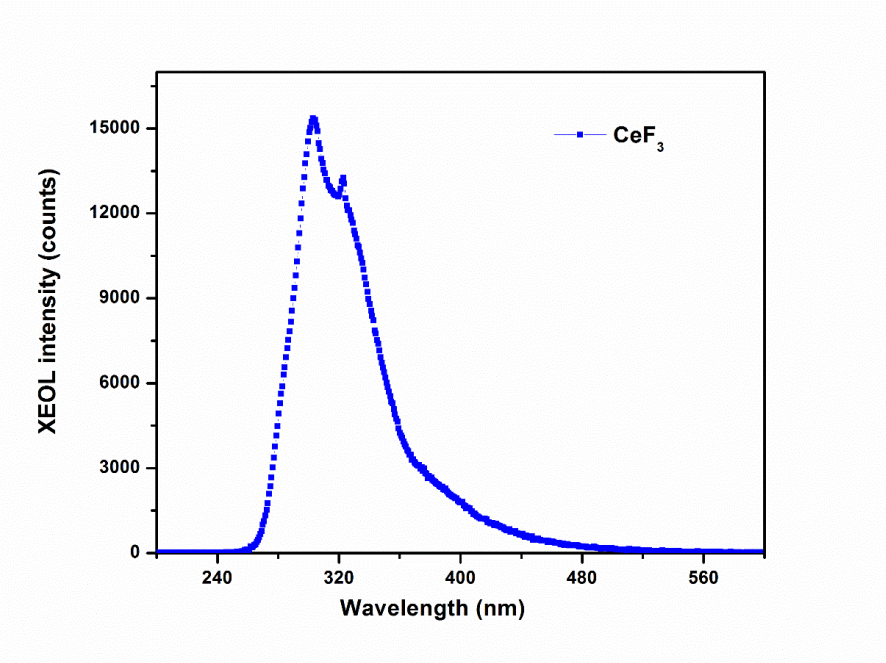

Figure 4-6 XEOL spectrum of as synthesized CeF3 nanoparticles.

Relative fluorescence quantum yield (QY) of the as synthesized CeF_3 nanoparticles was calculated using D-tyrosine and L-tryptophan as known reference sample. Quantum efficiency of D-tyrosine is known as 0.13 in water at 23 °C when excited at 275 nm and 0.12 in water for L- tryptophan at 275 nm excitation. Two known reference samples were used to cross check the measured value of QY.

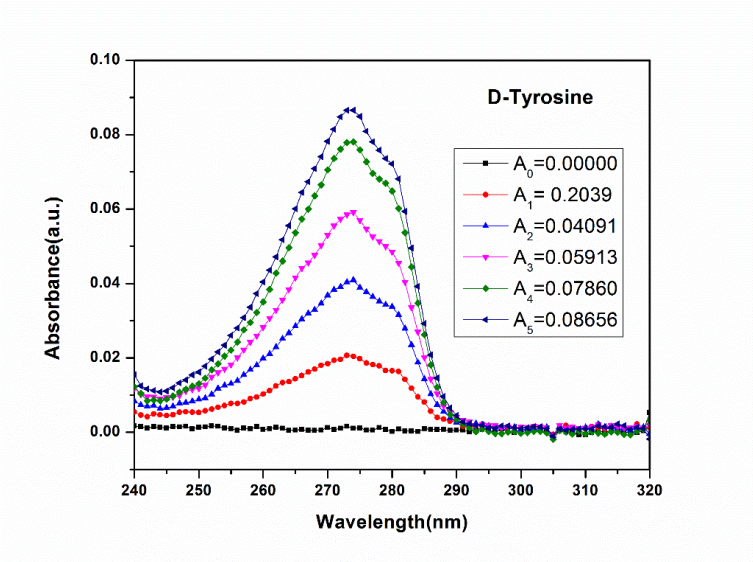

Figure 4-7 UV-Vis absorption spectra of different concentrations of D-tyrosine in water.

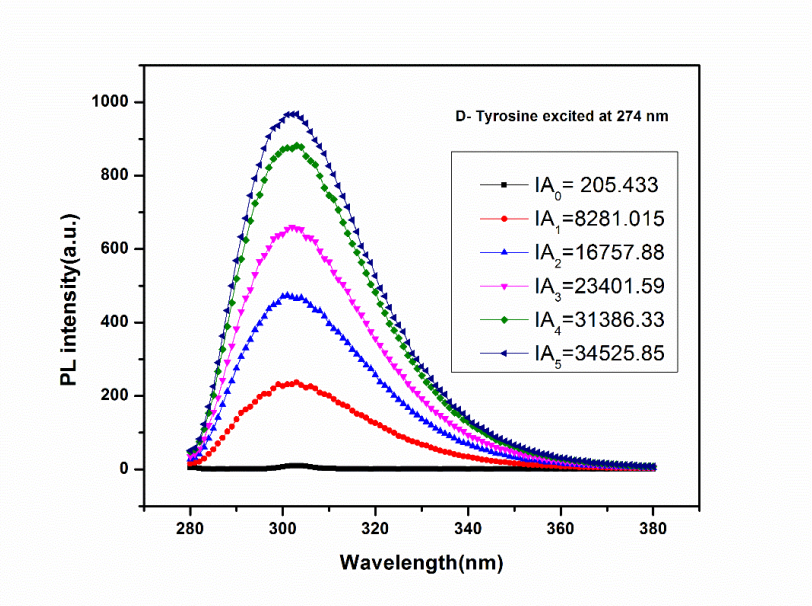

Figure 4-8 Photoluminescence emission spectra of different concentrations of D-tyrosine in water at 274 nm excitation.

To measure the relative quantum efficiency of CeF_3 nanoparticles in water, CeF_3 nanoparticles, tyrosine and tryptophan were dispersed in water at very low concentrations. UV-visible absorption spectrum is obtained at 5 different concentrations for tyrosine, tryptophan and CeF_3 nanoparticles as shown in Figure 4-7, 4-9 and 4-11 respectively. To avoid the light scattering, absorbance should be below 0.1 on and above the excitation wavelength of known reference samples and CeF_3 nanoparticles. Photoluminescence spectra are collected at all 5 different concentrations for tyrosine, tryptophan and CeF_3 nanoparticles at the same experimental conditions for each sample as shown in Figure 4-8, 4-10 and 4-12 respectively. In this study CeF_3 nanoparticles were excited at 250 nm.

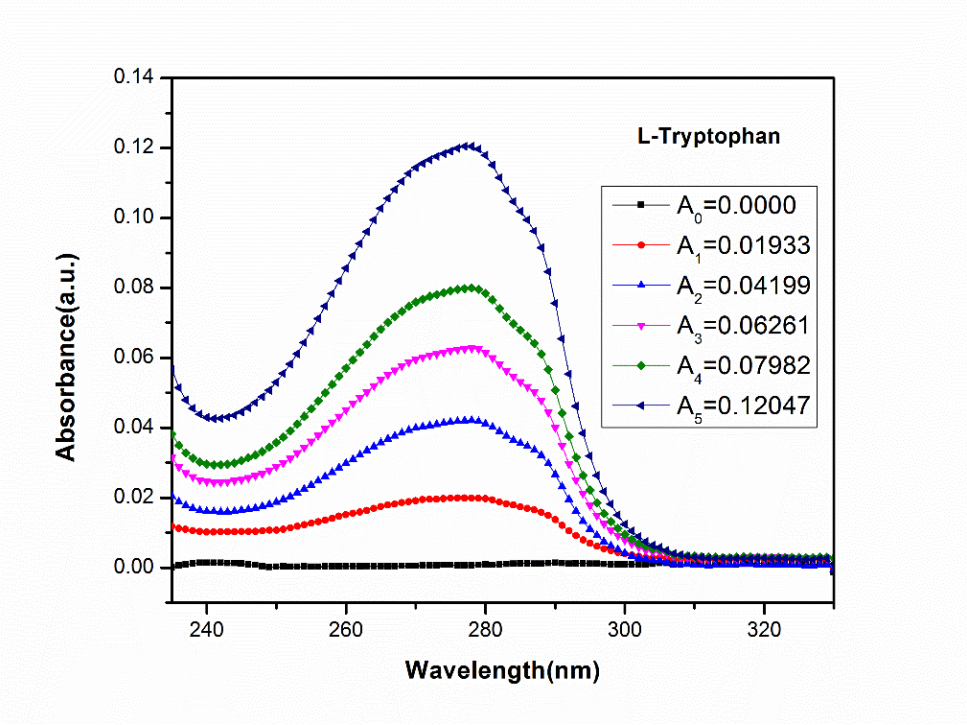

Figure 4-9 UV-Vis absorption spectra of different concentrations of tryptophan in water.

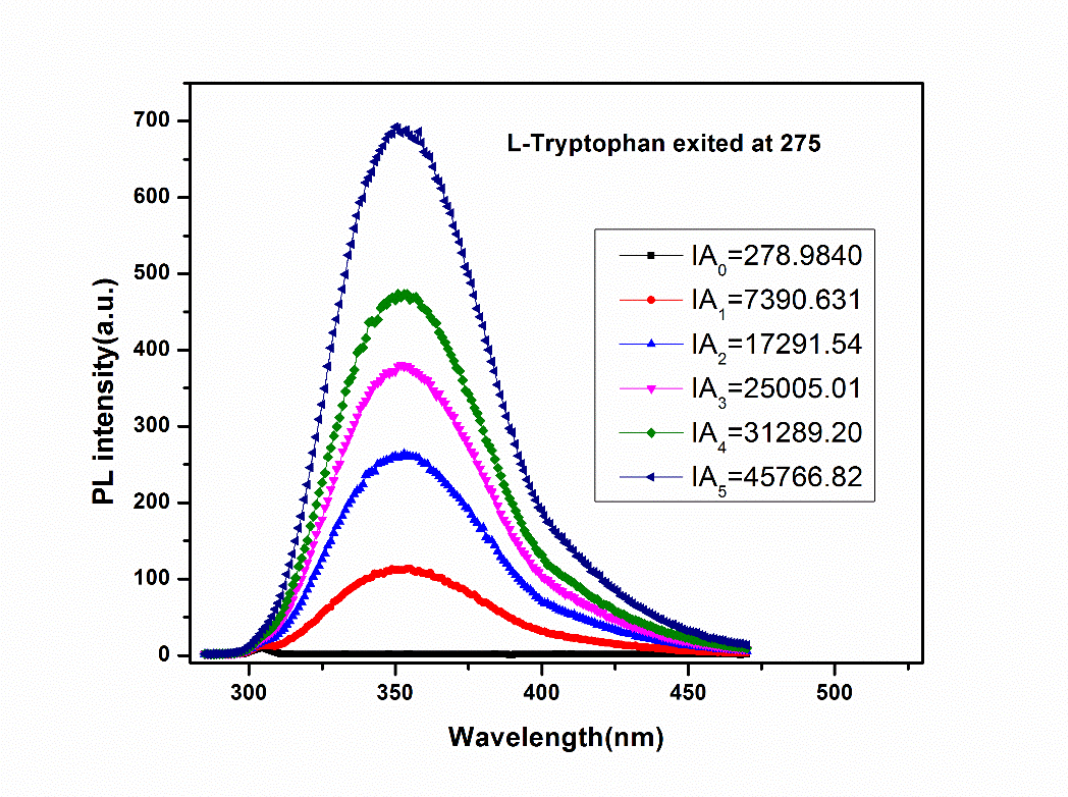

Figure 4-10 Photoluminescence emission spectra of different concentrations of L-tryptophan in water at 275 nm excitation.

Photoluminescence integrated area is calculated for each emission spectra. Then the emission integrated area (IA) versus absorbance (A) of the two standard sample and CeF_3 nanoparticles are plotted as shown in figure. The change in emission with absorbance is a straight line as shown in Figure 4-13. The QY is determined using equation (4.1). To cross check the obtained value of QY, QY of L-tryptophan is calculated as 12 % using D-tyrosine which matches well with the reference value. The QY for CeF_3 nanoparticle in water excited at 250 nm is calculated as 11% using the two known reference samples.

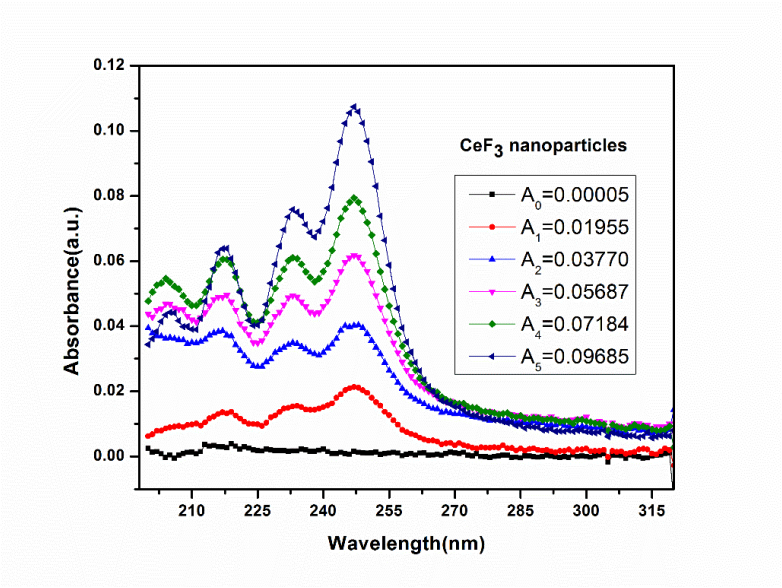

Figure 4-11 UV-Vis absorption of different concentration of CeF3 nanoparticles in water.

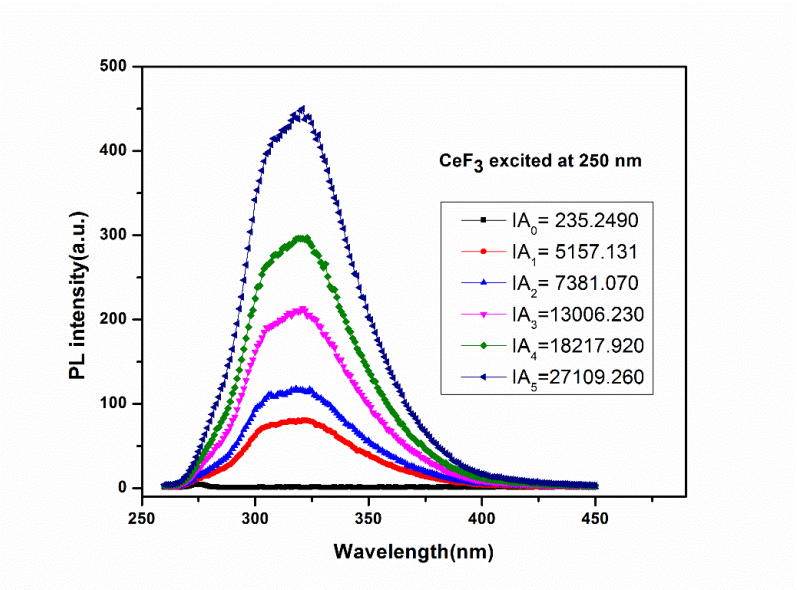

Figure 4-12 Photoluminescence emission spectra of different concentration of CeF3 nanoparticles in water excited at 250 nm.

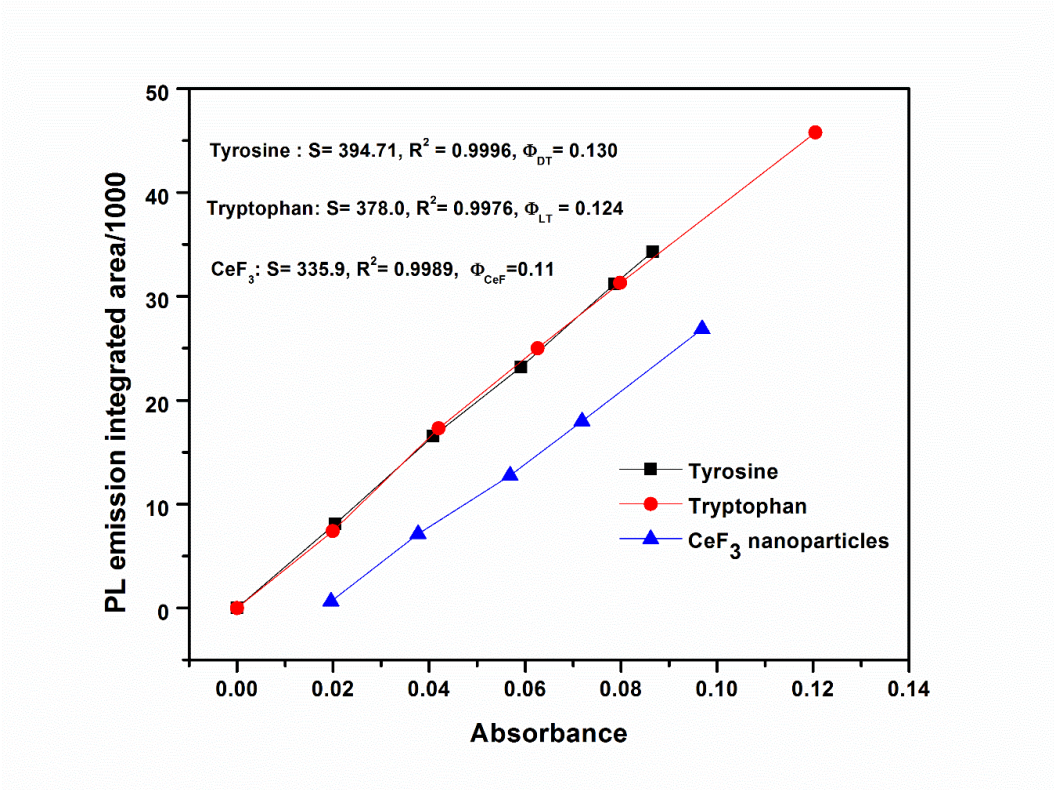

Figure 4-13 Plot of emission integrated area versus absorbance for tyrosine, tryptophan and CeF3 nanoparticles to calculate the relative QY of CeF3 nanoparticles in water.

For gamma radiation testing nanoparticles are required to embed in transparent matrix such as polymer or glass. As the as synthesized PEG-coated CeF_3 are highly dispersible in water, polyvinyl alcohol (PVA) which is a water soluble polymer was used as a matrix. Nanoparticles were embedded as describe in the experimental section. This sample of CeF_3-PVS film was fabricated by casting thick solution of CeF_3-PVA in petri dish. Photoluminescence of CeF_3-PVA shows the characteristics emission of CeF_3 nanoparticles as shown in Figure 4-14. However, the sample showed no scintillation when excited with gamma ray using Ba-133 (356 keV) and Cs-137(662 keV). This is due to the small thickness of PVA film, which is not enough to stop high energy gamma radiations.

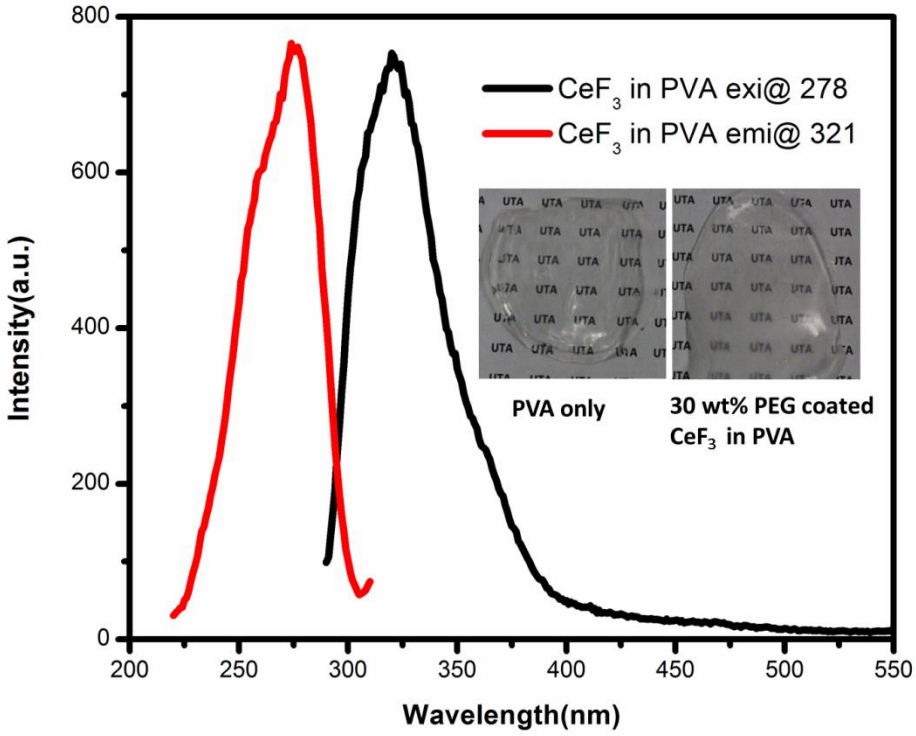

Figure 4-14 Photoluminescence emission and excitation of CeF3 nanoparticles embedded PVA. Inset shows the photo of neat PVA and 30 wt% CeF3 loaded PVA thin film.

The optical transmittance of PVA film and CeF_3 loaded PVA film is shown in Figure 4-15. PVA film shows, light transmittance higher than 80% above 400 nm. However, the light transmittance decreases to about 60% in the region of CeF_3 emission. In case of 30 wt% CeF_3 loaded PVA film, light transmittance is about 40%.

To test the scintillation response of CeF_3 nanoparticles, we have also fabricated a semitransparent disc of CeF_3 nanoparticles by pressing nanoparticles using hydraulic pressing system from Specac. Scintillation response to relatively low energy Ba-133 (356

eV) and high energy Cs-137 (662 keV) were tested by placing the CeF_3 disk in the base of the PMT using optical grease. The pulse height spectra of Ba-133 and Cs-137 obtained with CeF_3 semitransparent disk is shown in Figure 4-16 and 4-17 respectively. Unlike CeF_3-PVA film, CeF_3 disk shows scintillation counts when excited with gamma source. This is due to the increased stopping power of CeF_3 disk due to high nanoparticles concentration and increased thickness of the sample.

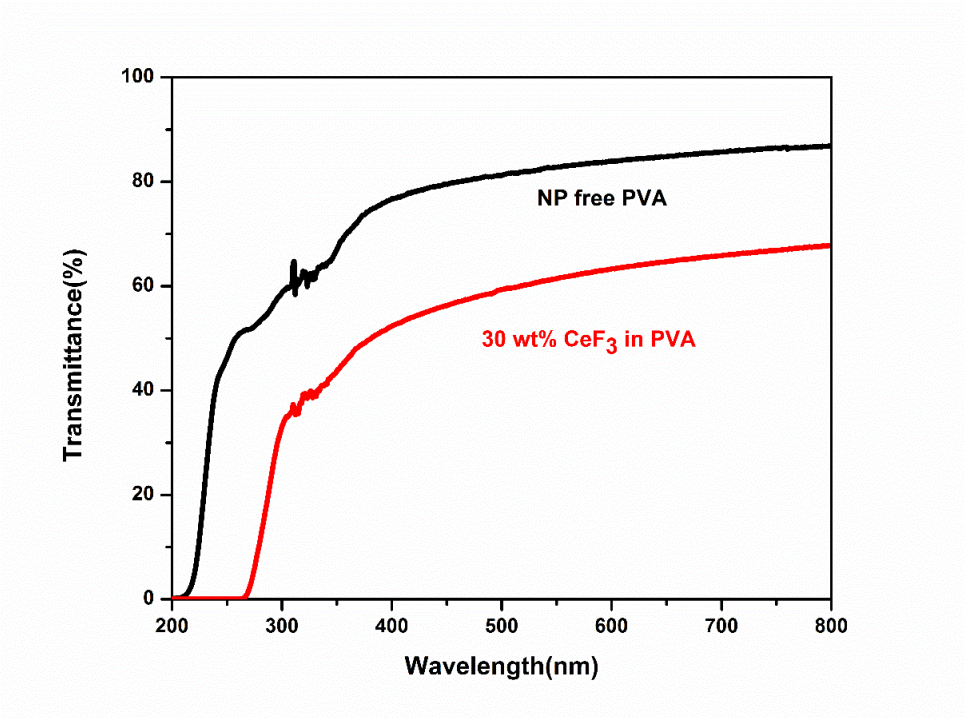

Figure 4-15 Optical transmission of PVA film and 30 wt% CeF3 loaded PVA film.

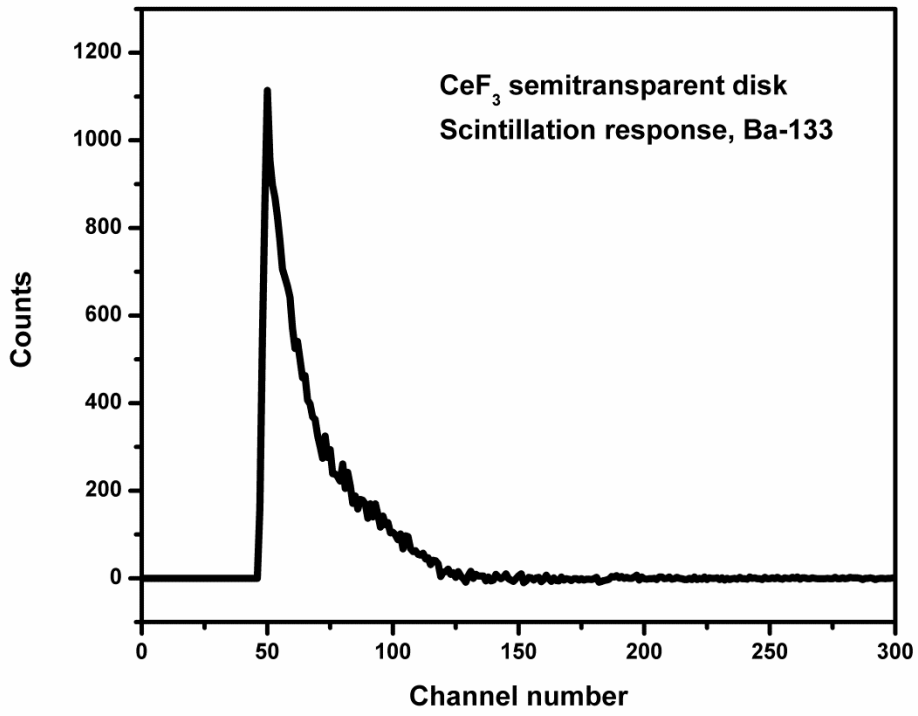

Figure 4-16 Pulse height spectrum of Ba-133 obtained using CeF3 disk.

However, there are no evidences of photopeak for both low energy gamma and high energy gamma ray source. This could be due to factors such as small size of the test sample especially the thickness of the sample and low transparency. In addition to the sample factor, CeF_3 has emission peak at around 325 nm where the detection efficiency of the photomultiplier tube is low.

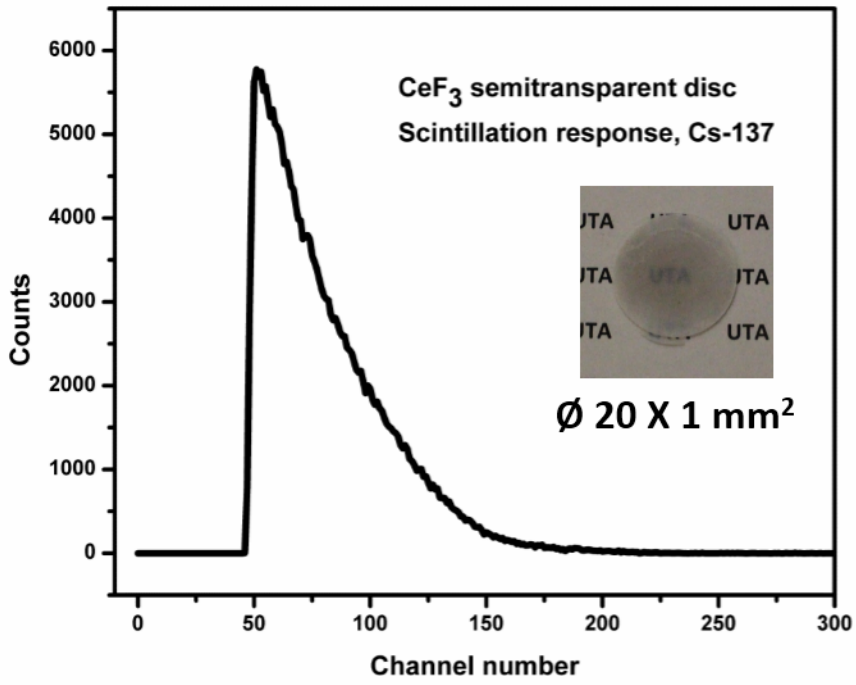

Figure 4-17 Pulse height spectrum of Cs-137 obtained using CeF3 semitransparent disk.

To overcome the problem of low PMT detection efficiency in the region of CeF_3 emission, we have used zinc oxide (ZnO) semiconductor nanoparticles to synthesize CeF_3/ZnO nanocomposite. ZnO has size dependent band edge emission at around 385 nm and defect related emission in visible range. CeF_3/ZnO is expected to show emission of ZnO due to fluorescence resonance energy transfer (FRET) energy transfer from CeF_3 to ZnO, which will be discussed in next section.

4.3.2 CeF_3/ZnO Nanocomposite

Zinc Oxide (ZnO) nanoparticles have strong absorption in UV region and overlaps well with the emission of CeF_3 nanoparticles. Moreover, the size dependent optical absorption of ZnO nanoparticles can be tuned as a result of quantum confinement. In this work we have synthesized ZnO nanoparticles using different method.

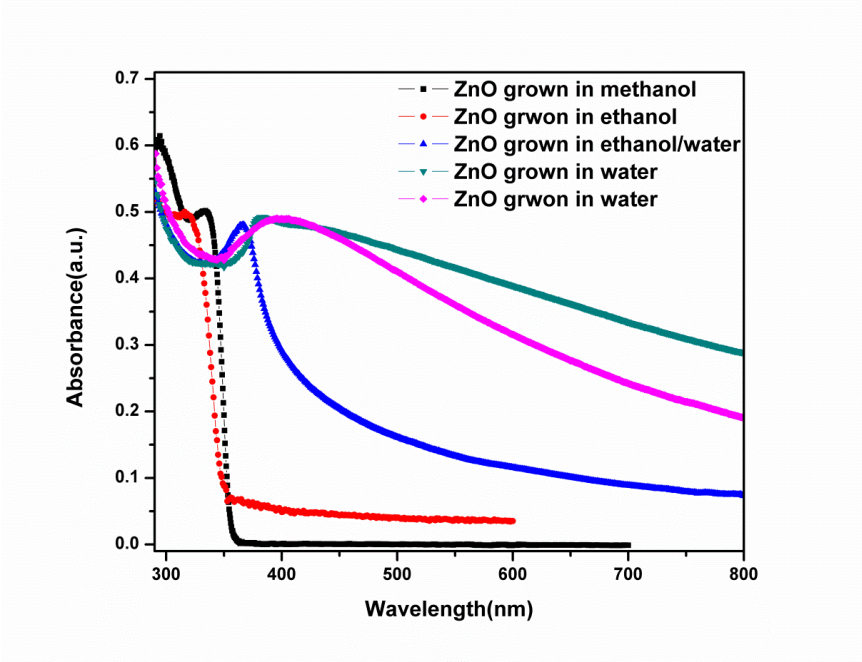

Figure 4-18 UV-Vis optical spectra of ZnO nanoparticles synthesized in different solvent.

Figure 4-18 shows the optical absorption spectra of ZnO nanoparticles synthesize using different method. ZnO nanoparticles synthesized in alcohol (methanol or ethanol) shows optical absorption with peak at shorter wavelength compared to the one synthesized in water. ZnO nanoparticles synthesized in mixed solvent of water and ethanol shows peak at the intermediate wavelength.

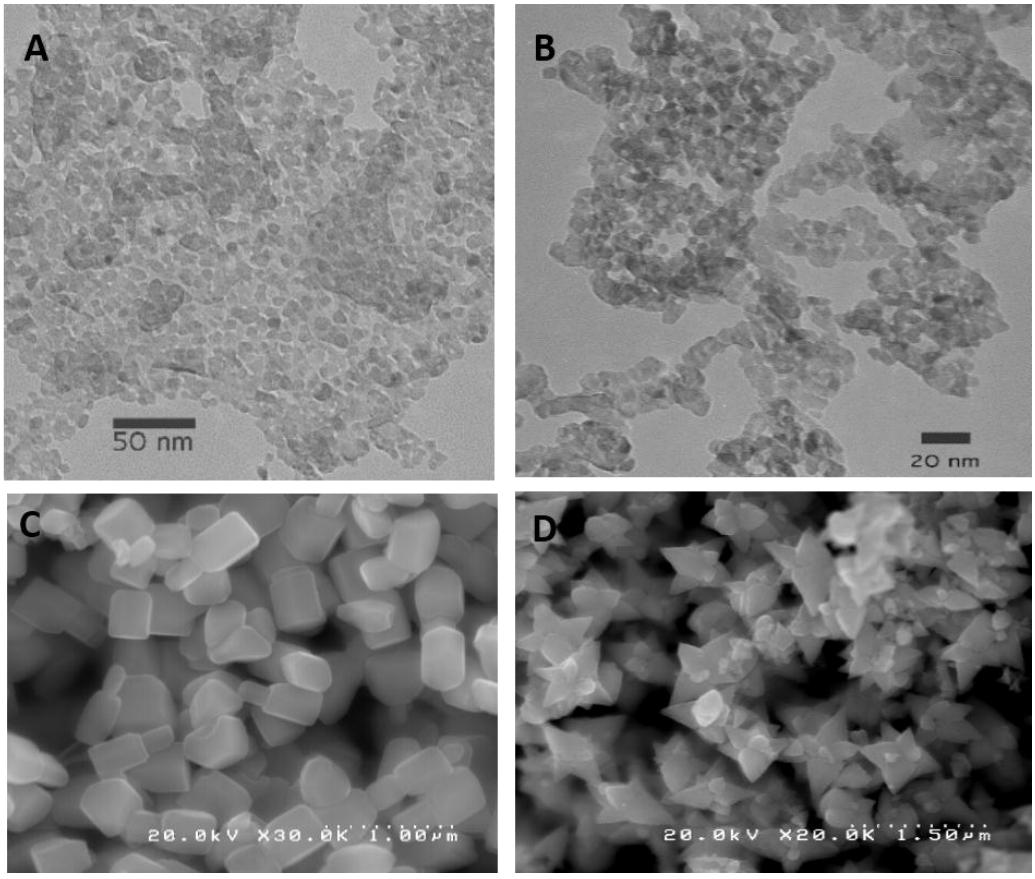

Figure 4-19 ZnO nanoparticles synthesized in different solvents (A) ZnO nanoparticles synthesized in methanol, (B) ZnO nanoparticles synthesized in ethanol, (C) ZnO nanoparticles synthesized in water (ZnO-W1), (D) ZnO nanoparticles synthesized in water (ZnO-W2).

This is due to the small size of ZnO nanoparticles synthesized in alcohol. The sizes of ZnO nanoparticles synthesized in different solvent were determined using scanning electron microscope and transmission electron microscope. Figure 4-19 shows the SEM and TEM image of ZnO nanoparticles synthesized in different solvent. ZnO nanoparticles synthesized in alcohol produce very small nanoparticles with size around 5 nm whereas nanoparticles synthesized in water produce large size particles with size around few

hundred nanometers. Also, nanoparticles synthesized in alcohol show uniform size distribution compared to the one synthesized in water.

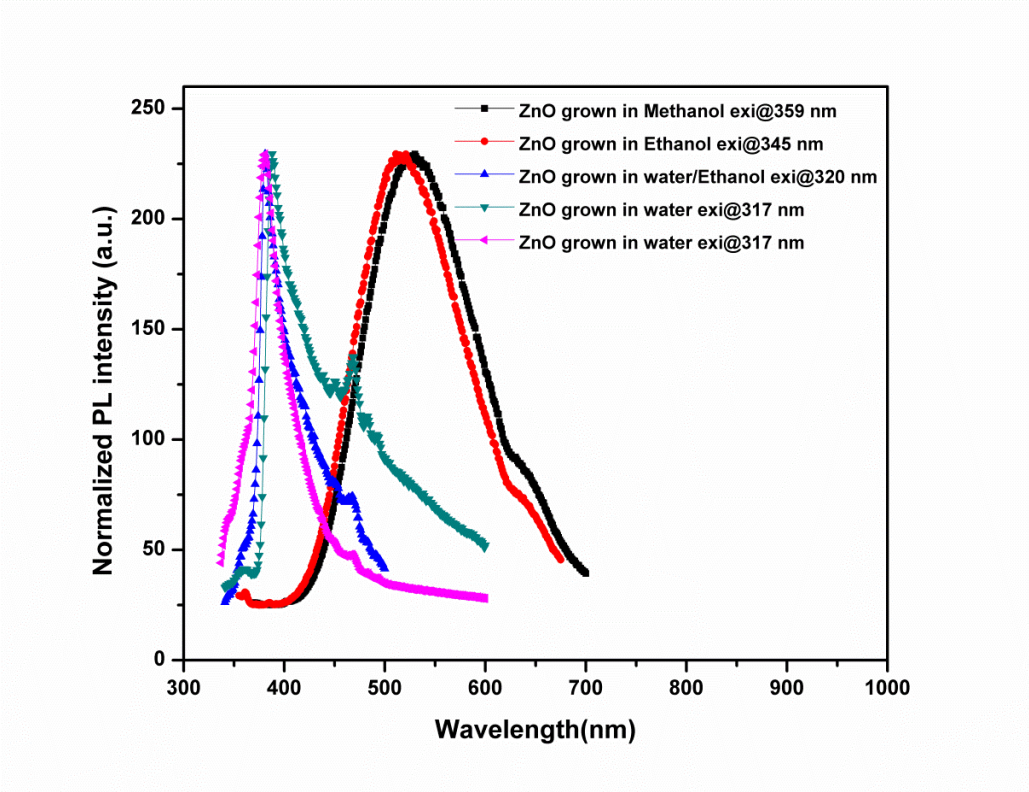

Figure 4-20 Photoluminescence emissions of ZnO nanoparticles synthesized in different solvents

Photoluminescence of ZnO nanoparticles synthesized in different solvent were measured as shown in Figure 4-20. ZnO nanoparticles synthesized in alcohol show dominant defect related emission, whereas nanoparticles synthesized in water and mixed solvent shows dominant band-edge emission. The green band emission corresponds to the singly ionized oxygen vacancy in ZnO and result from the recombination of a photo generated hole with the single ionized charge state of this defect.[82]

Figure 4-21 shows the XRD patterns of ZnO nanoparticles synthesized in different solvents. XRD pattern of all the ZnO nanoparticles matches well with the standard hexagonal wurtzite phase structure which is most the most stable structure of ZnO at ambient condition.

.

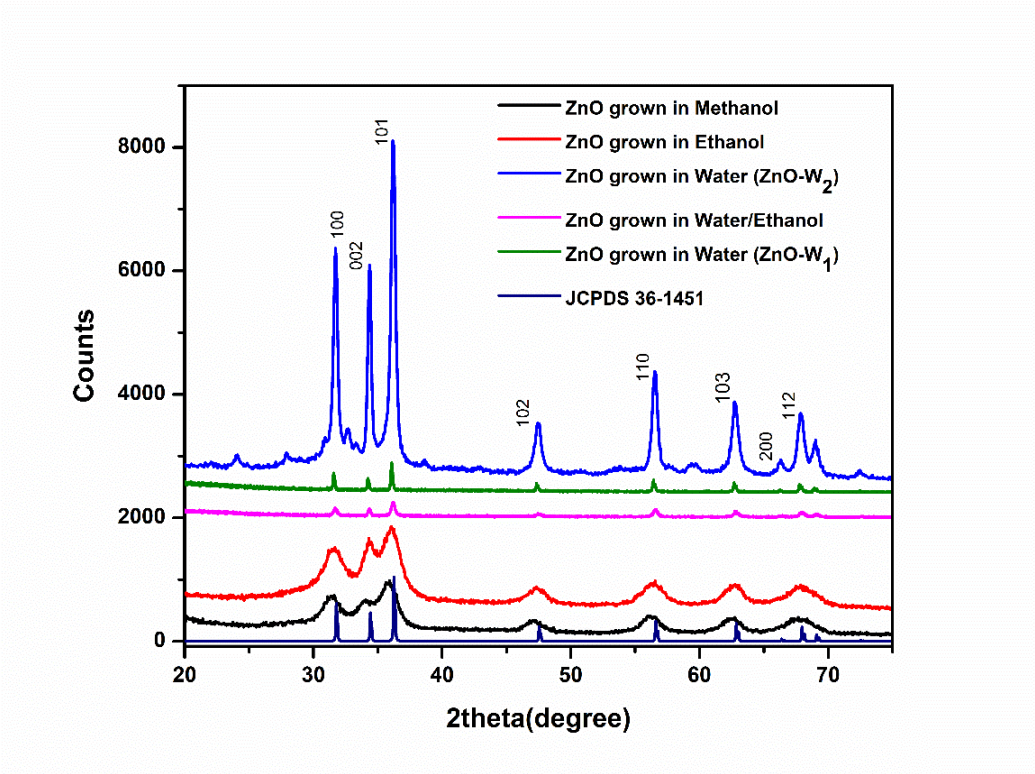

Figure 4-21 XRD pattern of ZnO nanoparticles, synthesized in different solvents.

ZnO nanoparticles synthesized in methanol and ethanol shows peaks broadening due to small size of nanoparticles.

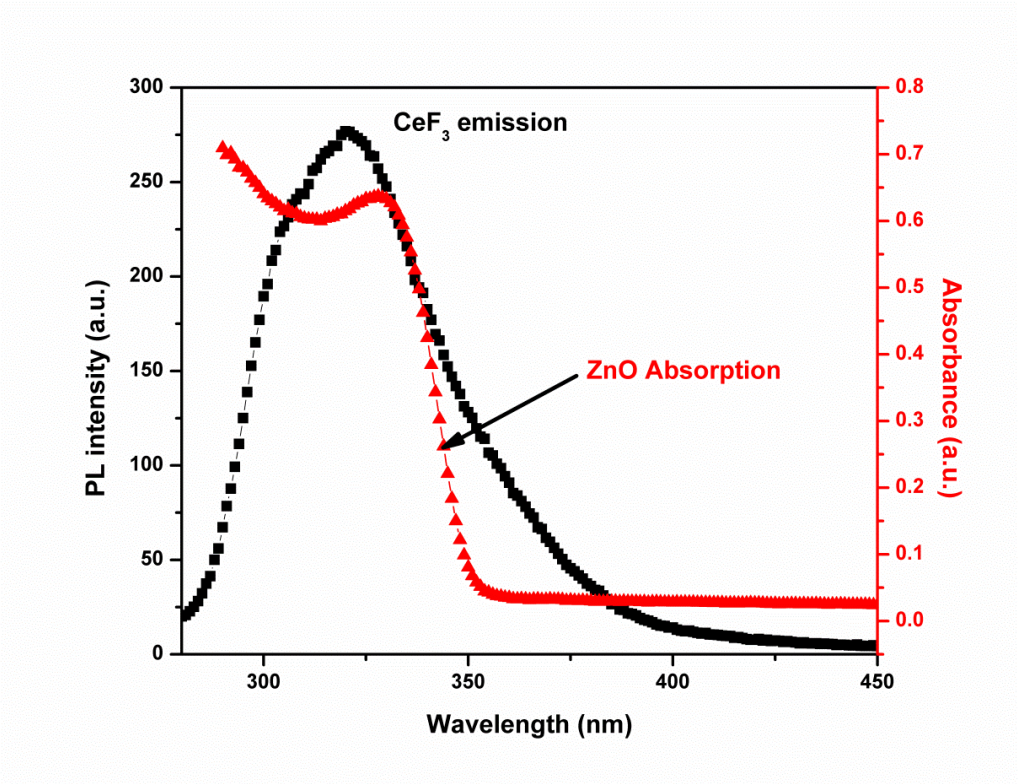

Figure 4-22 FRET overlapping of CeF3 emission and ZnO absorption.

Figure 4-22 shows the optical absorption spectrum of colloidal ZnO nanoparticles synthesized in methanol and emission spectrum of CeF_3 nanoparticles measured at room temperature. ZnO nanoparticles show the absorption peak at around 335 nm which is blue shifted compared to that of bulk ZnO as a result of quantum size confinement[83]. The emission peak in CeF_3 nanoparticles at around 325 nm is attributed to the 5d-4f transition of Ce^{3+} ion[84]. The emission peak of CeF_3 nanoparticles is overlapped largely with the absorption peak of ZnO nanoparticles fulfilling the condition for FRET energy transfer. Thus, it may expect that there would be efficient energy transfer from CeF_3 to ZnO in CeF_3/ZnO nanocomposites if the two nanoparticles are close enough. Figure 4-23 shows the photoluminescence emission of ZnO QDs and CeF_3/ZnO nanocomposites, both

excited by 290 nm excitation wavelength. ZnO nanoparticles have an emission peak at 366 nm and defect emission at 510 nm.

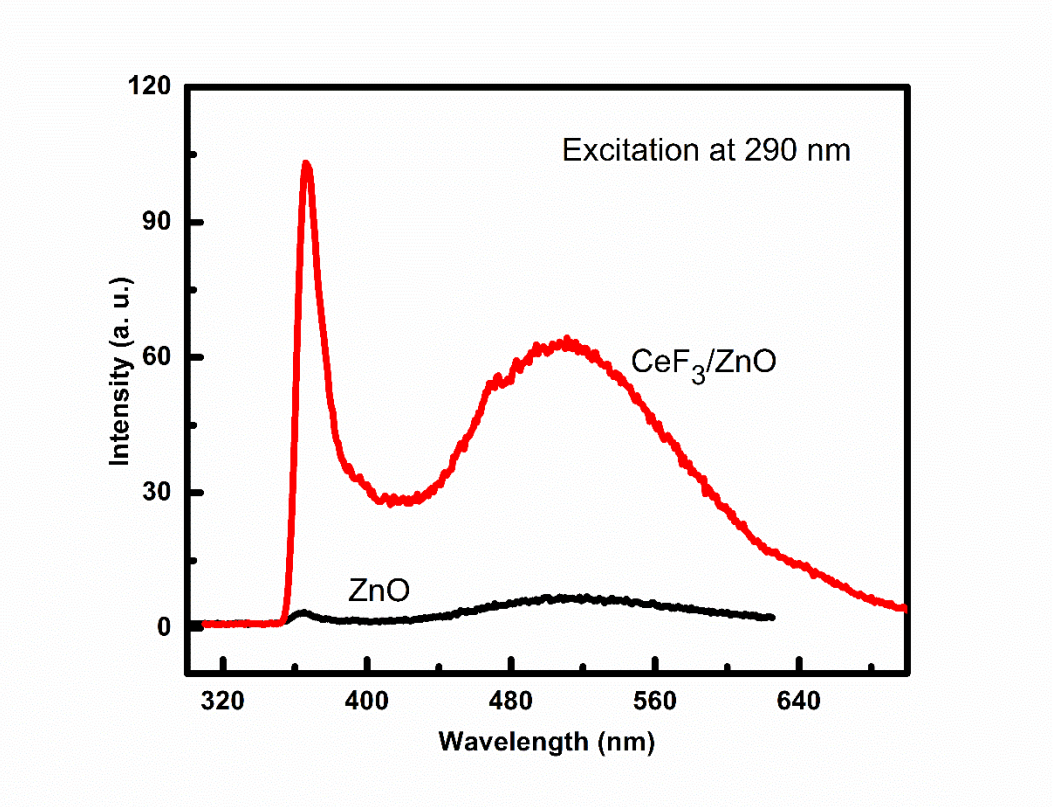

Figure 4-23 Photoluminescence emissions of ZnO nanoparticles and CeF3/ZnO nanocomposite excited at 290 nm.

Emission peak at 366 nm is attributed to the band edge excitonic emission and green emission is due to the oxygen vacancies[85] in ZnO. Due to the quantum confinement, the excitonic peak is significantly shifted to shorter wavelength as compared with that in bulk ZnO.[86] CeF_3/ZnO nanocomposites show a large enhancement in the photoluminescence of ZnO nanoparticles as compared to ZnO nanoparticles only. The enhancement for the excitonic emission is almost 30 times and the enhancement for the defect green emission is more than 10 times.

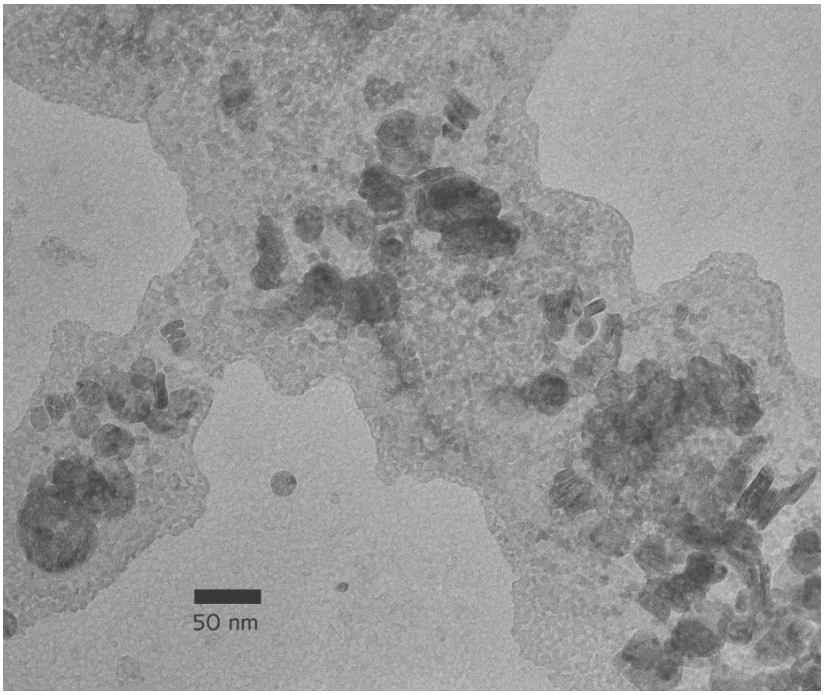

Figure 4-24 TEM image of CeF3/ZnO nanocomposite.

. In CeF_3/ZnO nanocomposites, the emission from CeF_3 nanoparticles is not observed. The quenching of CeF_3 emission and the enhancement of ZnO emission in CeF_3/ZnO nanocomposites indicate that there is energy transfer from CeF_3 to ZnO nanoparticles. As the quenching of CeF_3 emission is almost 100 % and this might indicate that the energy transfer efficiency is almost 100 %. As the FRET energy transfer efficiency depends on the distance between donor and acceptor. This high transfer efficiency is due to the large overlap of CeF_3 emissions with the ZnO absorption, as well as the two kinds of nanoparticles are closely together in the nanocomposites. To see the distance between two nanoparticles TEM image of nanocomposites was taken as shown in Figure 4-24. TEM image shows ZnO and CeF_3 are separated by less than 5 nm. This shows that FRET energy transfer from CeF_3 to ZnO is possible by bringing the nanoparticles close together.

.

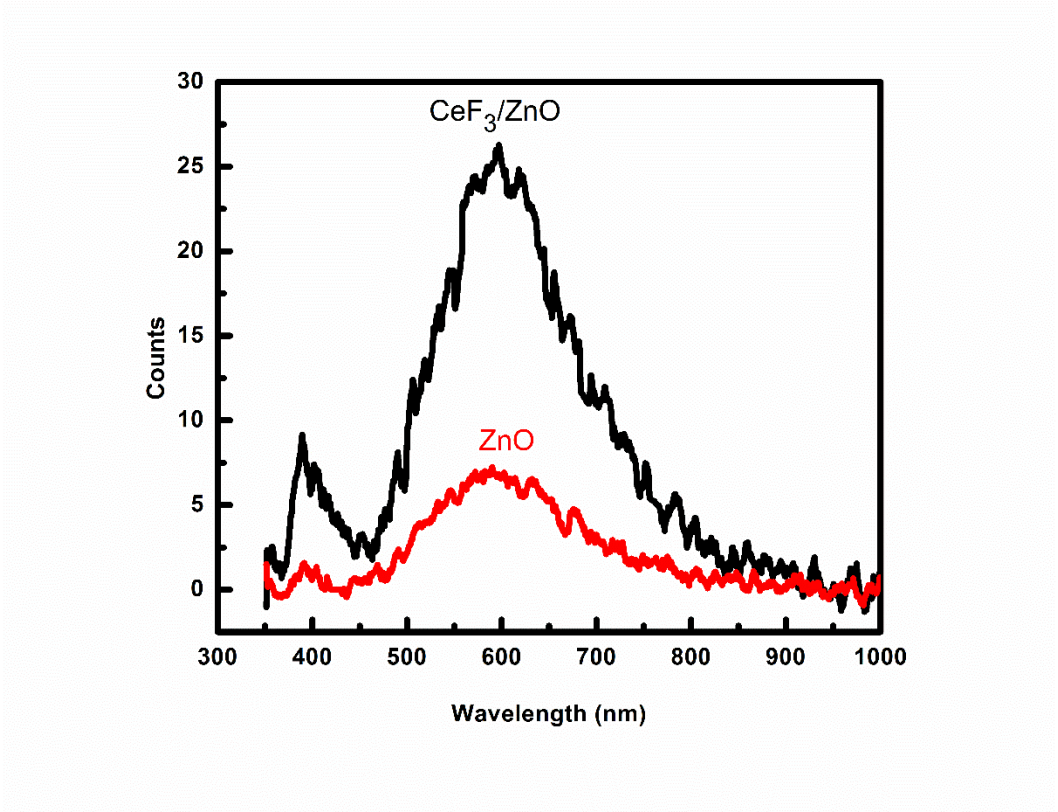

Figure 4-25 X-ray excited optical luminescence (XEOL) spectra of ZnO and CeF3/ZnO nanocomposite.

As pointed out that ZnO is a promising material for radiation detection due to its high exciton binding energy, fast decay lifetime, good stability and environmentally friendly[87]. The energy transfer in CeF_3/ZnO nanocomoposites might enhance the X-ray excited luminescence or scintillation luminescence for radiation detection. For that, we investigated X-ray excited luminescence as shown in Figure 4-25. Obviously, the X-ray excited luminescence of ZnO nanoparticles in CeF_3/ZnO nanocomposites were enhanced about 4 times both in the exciton and the defect emissions by comparing to that of X-ray excited luminescence from ZnO nanoparticles. Here we should point out that the exciton

emission in the X-ray excited luminescence is weaker in intensity than the defect emission and both the exciton and the defect emissions are shifted about 20 nm to longer wavelength by comparing with their photoluminescence emissions. This is because the photodetector for the X-ray excited luminescence system has lower sensitivity in UV range. The other possibility is that the defect emission is stronger because more defects were created by X-ray irradiation during the measurement.

We also noticed that the enhancement in photoluminescence is much higher than in X-ray luminescence. The reasons are not very clear yet. One possible reason is that the two luminescence processes excited by light and by X-ray are different. In photoluminescence, the UV or visible light excites the luminescence centers to higher energy states, then relax to the emitting state and return to the ground state to produce luminescence. In X-ray luminescence, absorption of X-ray photons produces energetic electrons and holes. These electrons and holes transfer their energy to the luminescence centers to excite them to higher energy states, then relax to the emitting state and return to the ground state to produce luminescence. Thus, the X-ray luminescence is more complicated than photoluminescence, and also involves electrons, holes and defects. In this case, it is understandable that energy transfer enhancement in X-ray luminescence is weaker than in photoluminescence.

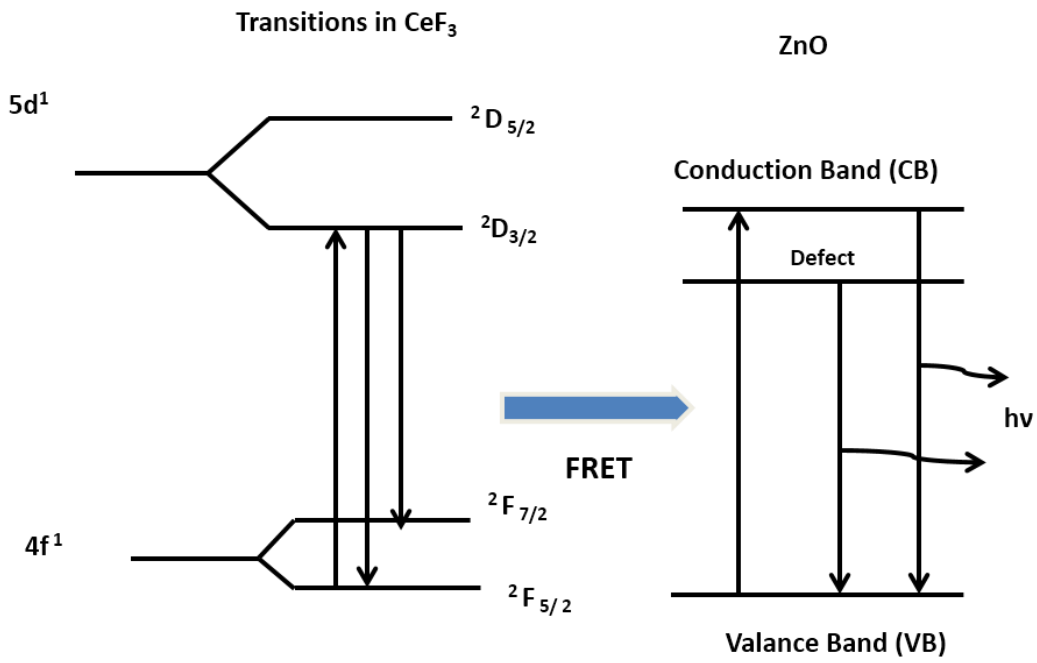

Figure 4-26 Schematic of FRET energy transfer from CeF3 to ZnO.

The energy transfer mechanism from CeF_3 to ZnO nanoparticles can be explained through the energy level diagram as shown in Figure 4-26. Under 290 nm excitation, CeF_3 nanoparticles emits light with peak at 334 nm due to 5d-4f transition, which is in resonance with the excitation spectrum of ZnO nanoparticles. If the two nanoparticles come close together then CeF_3 nanoparticles transfer its energy to the ZnO nanoparticles through dipole-dipole transition. The energy transfer mechanism exited by X-ray should be similar but the efficiency might be different because some point defects or color centers are created by X-ray irradiation and these defects would influence the luminescence and energy transfer efficiencies.[88-96]

Figure 4-27 shows the XRD pattern of the as synthesis ZnO nanoparticles and CeF3 nanoparticles along with CeF3/ZnO nanocomposite. Peak broadening is due to the small size of the particles. The average size of the ZnO nanoparticles is estimated to be about 5 nm by the (101) peak using the Scherer's equation, D= 0.9 λ/ β Cosθ, where D is the average size of the particles, λ is the X-ray wavelength (1.5406 Å), θ is the diffraction angel and β is FWHM of an observed peak. In the XRD pattern of as synthesis CeF_3 nanoparticles, can be indexed to the hexagonal phase of CeF_3. The particle size is estimated to be about 10 nm using the (300) peak. The particles size of ZnO and CeF_3 are closely matches with the size obtained from TEM image.

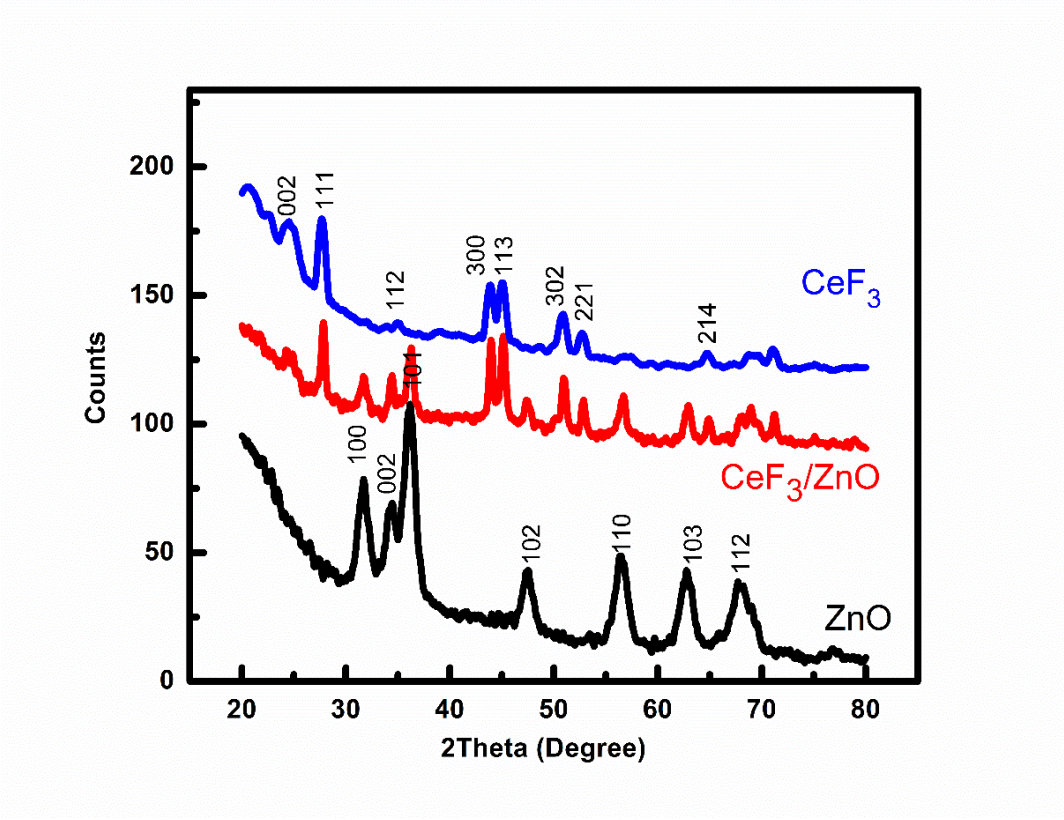

Figure 4-27 XRD patterns of CeF3 nanoparticles, ZnO nanoparticles and CeF3/ZnO nanocomposite.

For radiation detection, the materials must be stable or have high radiation hardness. The XRD patterns of CeF_3/ZnO nanocomposites before and after X-ray irradiation for 5 and 10 minutes are displayed in Figure 4-28. Their XRD profiles are almost identical and the diffraction line intensities are almost the same. This indicates that these nanocomposites are very stable under X-ray irradiation at the dose rate we have in the lab. The high radiation hardness of these materials means they are potentially good for radiation applications.

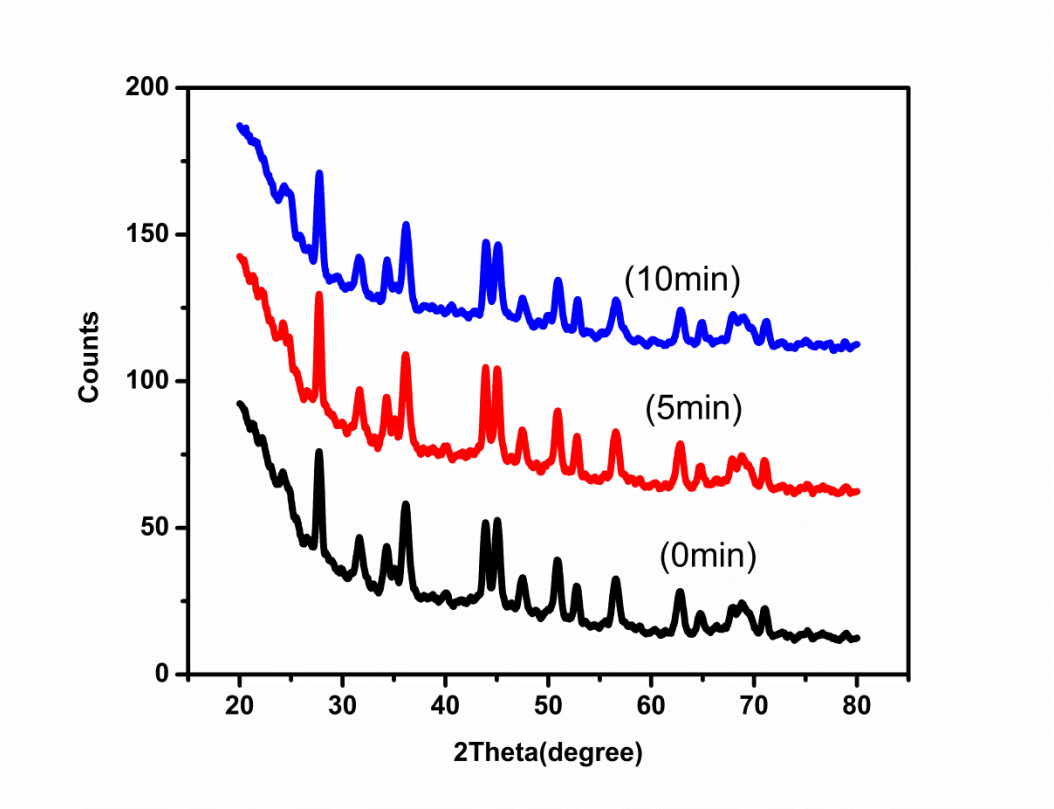

Figure 4-28 XRD pattern of CeF3/ZnO after exposure to X-ray for different time.

For gamma ray spectroscopy, ZnO and CeF_3/ZnO transparent nanocomposites were fabricated by in-situ synthesis of ZnO and CeF_3/ZnO in PMMA. ZnO-PMMA shows

blue emission with peak at 450 nm as shown in Figure 4-29. The emission of transparent ZnO-PMMA matches well with the high detection efficiency region of the PMT. CeF_3/ZnO nanocomposites were fabricated by adding the as synthesis CeF_3 nanoparticles during the in-situ synthesis of ZnO-PMMA nanocomposite.

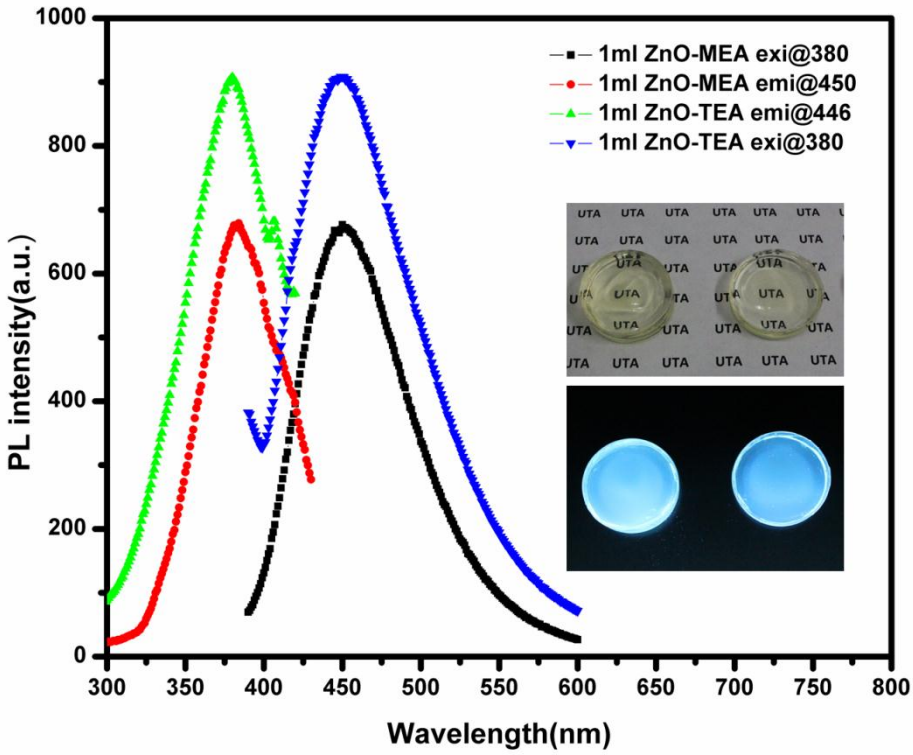

Figure 4-29 Photoluminescence of transparent ZnO/PMMA nanocomposites.

The photoluminescence of CeF_3/ZnO/PMMA is shown in Figure 4-30. The CeF_3 nanoparticles loaded nanocomposites shows slight enhancement in photoluminescence at very low nanoparticles loading. However, further increase in nanoparticles loading shows luminescence quenching in the nanocomposites. Moreover, at higher than 1 wt% CeF_3

loading, air bubbling appears during the polymerization process. The final products obtained with higher loading were filled with air bubbles. The final product didn't show scintillation counts when tested under 662 keV gamma source. This could be due to the small amount of inorganic nanoparticles presence in the nanocomposite as well as loss of transparency of PMMA matrix as shown in Figure 4-31. CeF_3/ZnO/PMMA nanocomposite shows light transmittance of 30% compared to 60% light transmittance in case of ZnO/PMMA nanocomposite.

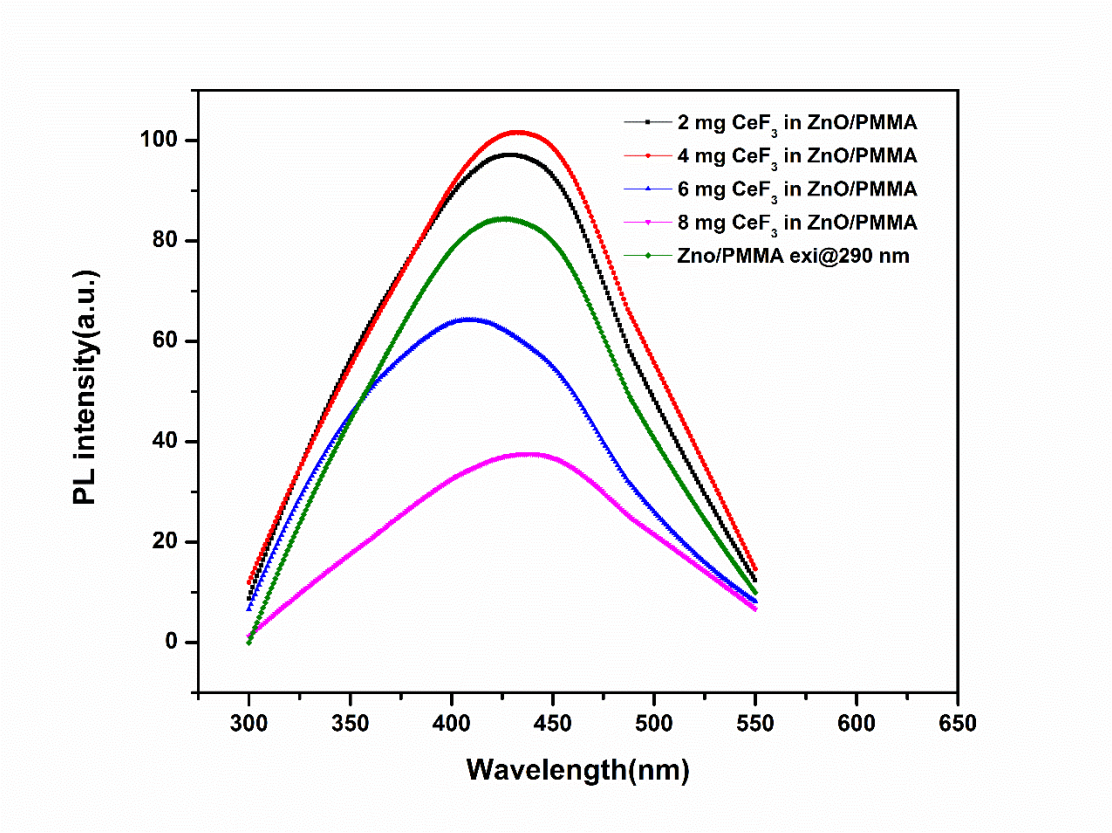

Figure 4-30 Photoluminescence of different amount of CeF3 nanoparticles in transparent ZnO/PMMA nanocomposites.

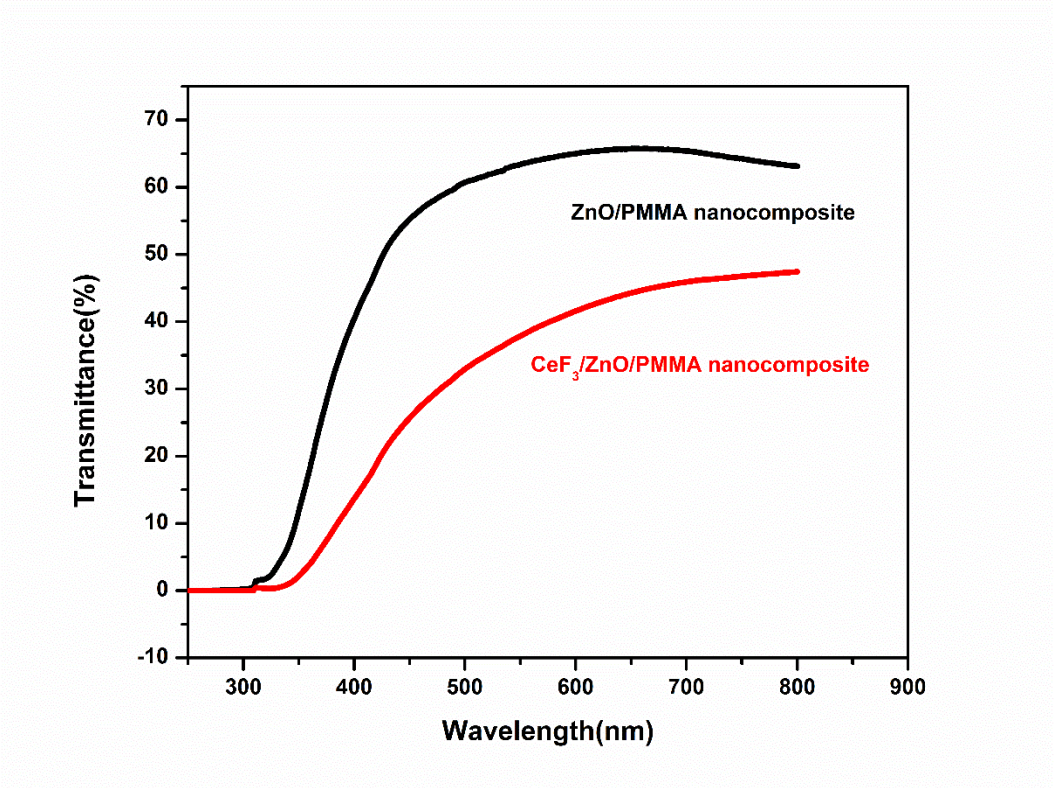

Figure 4-31 Optical transmittance of ZnO/PMMA and CeF3/ZnO/PMMA nanocomposite

4.4 Summary

In summary, CeF3/ZnO nanocomposites were successfully synthesized using a two-step wet chemistry method and large energy transfer was observed from CeF_3 to ZnO nanoparticles in the nanocomposites. Consequently, the photoluminescence of ZnO nanoparticles is enhanced more than 30 times and the X-ray excited luminescence is enhanced more than 4 times in the nanocomposites by comparing with that of ZnO nanoparticles only. The nanocomposites are very stable under X-ray irradiation. These energy transfer based nanocomposites are potentially promising for radiation detection,

solid state lighting, biological sensing, and solar cell enhancement as well as light sources for photodynamic activation for therapeutic applications. For radiation detection, CeF_3/ZnO is embedded in to PMMA matrix to produce transparent CeF_3/ZnO/PMMA nanocomposites by in-situ bulk polymerization method. The as fabricated nanocomposite show slight enhancement in the photoluminescence of ZnO/PMMA nanocomposites. However, at higher CeF_3 loading nanocomposites shows luminescence quenching. Moreover, no scintillation counts were observed from the as fabricated nanocomposites. This is due to the small quantity of inorganic nanoparticles in the nanocomposites. In the next chapter, we have used hydrophobic organic surfactant to coat the surface of nanoparticles to improve the nanoparticles dispersion into polymer matrix. We have used free radical bulk polymerization method to fabricate thicker sample for scintillation testing. The as coated CeF_3 nanoparticles were embedded in PVT matrix along with organic dye PPO to fabricate CeF_3/PPO/PVT nanocomposite for radiation detection.

Chapter 5

Oleic Acid coated CeF_3 Nanoparticles Embedded PPO/PVT Scintillators

5.1 Introduction

The development of high-performance scintillating materials is essential for precision calorimetry in high energy physics[97], medical imaging[98] and industries.[99] The most frequently considered characteristics of scintillators are efficiency of energy conversion, stopping power, luminescence decay time, spatial resolution, and physical and chemical stability.[8] Currently applied inorganic crystalline scintillators are not only limited by their high cost and scalability issues, but also limited by other intrinsic drawbacks. For example, high purity germanium must be operated at liquid nitrogen temperature, while sodium iodide crystal is highly hygroscopic. On the other hand, plastic scintillators based on polymeric materials are cheap and easy to manufacture, but have low light yield and low density.[30] Also, it has been reported that the plastic scintillator loses its optical and mechanical properties as the radiation doses increases.[100] These limit the application of plastic scintillator for high energy gamma-ray detection. Hence, the drawbacks of conventional inorganic and organic scintillators necessitate new generation of scintillators which could combine high performance of inorganic scintillating materials with scalability of polymer materials. One practical approach is to make nanocomposite materials which consist of high density and high-performance scintillating nanoparticles embedded in a polymer matrix maintaining the transparency of the matrix.

Transparent nanocomposites can be obtained by index matching of the filler and the matrix. However, literature reported that sufficiently small size of the filler could lead to minimized optical scattering even with a large mismatch of refractive index.[38] Based on this, many approaches have been taken to make composite materials consisting of high Z nanomaterials embedded in different matrix (polymer or glass) for scintillator application.

The main goal is to enhance the luminescence of nanocomposites by incorporation of high Z material, so that it can be used for gamma ray spectroscopy. Early development of composite scintillators used grinding method, but resulting in materials that were not transparent.[39] Kang et al. used index matching of nanoparticles and the polymer matrix to make nanocomposites with high transparency.[46] Polymer composite film with BiI_3 and conjugated polymer reported by Zhong et al. exhibits photoluminescence quenching due to the charge transfer from the polymer matrix to BiI_3.[101] Feller et al. used oleic acid as both a ligand and a matrix to achieve high nanoparticle loading while keeping the transparency up to 70 %.[45] Cai et al. used non-fluorescent Gd_2O_3 nanocrystals dispersed in PVT matrix and reported enhanced luminescence due to fluorescent resonance energy transfer (FRET) from the matrix to the fluor.[32] Also, nanoporous glass were used as a matrix for CdSe/ZnS core/shell quantum dots by Latent et al., which shows better energy resolution of 59-KeV americium-241 than that of NaI single crystal.[36] Yao et.al loaded LaF3:Ce nanoparticles in to ORMOSILs for scintillator application.[35] It has also been reported that the energy transfer based nanocomposite material could be a potential material for the radiation detection.[49, 50] In this work we have used nanoparticles of known heavy scintillator materials along with known scintillating organic fluor as fillers and polyvinyl toluene (PVT) as a matrix. The nanocomposites show enhancement in the luminescence due to FRET energy transfer from the nanoparticle to the organic fluor.

In the last decade rare earth fluoride nanoparticles were extensively studied for various applications.[102-106] Among the rare earth fluorides, cerium fluoride (CeF_3) nanoparticles have been of particular interest due to the Ce^{3+} emission. CeF_3 nanoparticles were synthesized using different techniques from hydrothermal[107], solvothermal[108], extraction method[109], microwave[110], sonication assisted method[111], reverse

micelles route[112], microemulsion[113, 114] to wet chemistry[104]. First identified as a scintillator in 1989, CeF_3 is known as an appealing scintillating material due to its high density and short decay time.[65] However, the emission of CeF_3 lies within UV range, which is not suitable for direct detection by photomultiplier tube and photodiode. Therefore, a wavelength shifter is needed to transfer the emission energy from CeF_3 to higher wavelength. For this purpose, 2, 5-diphenyloxazole (PPO) is selected due to its appropriate luminescent properties. Furthermore, PPO has already been widely used as a fluor in plastic scintillators. Here, we have chosen PVT as an organic polymer matrix that has been widely used as a base for plastic scintillator due to its ease of fabrication and low cost. We have synthesized CeF_3 nanoparticles coated with oleic acid and embedded these nanoparticles into the polymer matrix along with PPO to make nanocomposites scintillators. Enhancement in the luminescence of PPO has been observed under ultraviolet (UV) and X-ray excitation.

5.2 Experimental

5.2.1 Synthesis of Cerium Fluoride Nanoparticles

In this work, CeF_3 nanoparticles were synthesized via a precipitation reaction. Briefly, 30 mmol sodium fluoride (NaF) was dissolved into 80 mL of D.I water and mixed with 80 mL of ethanol solution containing 1.5 ml oleic acid. The mixture was heated to 80 °C under vigorous stirring with purging of argon gas. 10 mmol of $Ce(NO_3)_3.6H_2O$ was then dissolved into 60 mL of DI water and added into the above mixture dropwise. The reaction was kept as 80 °C for 4 hrs and then allowed to cool in the air. The precipitates were collected by centrifugation and washing with ethanol for three times and then dried at 50 °C for 12 hrs under vacuum.

5.2.2 Preparation of CeF_3/PPO/PVT Nanocomposites

After removal of the polymerization inhibitor from PVT monomers using a silica column, benzoyl peroxide (as the free radical initiator) (0.1 wt %) and PPO (0.5 wt %) were dissolved in PVT monomer solution and subjected to ultrasonication for 20 min. Then, different concentration (wt %) of CeF_3 nanoparticles were added into the above mixture and further sonicated for 45 min. During the first 45 min of incubation process at 75 °C, the CeF_3 nanoparticle-contained PVT monomer solution were agitated with vortex mixture for several times to ensure a good dispersion of CeF_3 nanoparticles in the monomer. After these treatments, the polymerization of PVT monomers has been sufficiently initiated so that the enhanced viscosity would prevent CeF_3 nanoparticles from aggregation. The composite was then allowed to be incubated at 75 °C for 90 hrs and then cooled down to room temperature. Free-standing CeF_3/PPO/PVT composites were then obtained after removing from the glass container.

5.2.3 Instrumentation for Materials Characterization

The HRTEM images of the particles were obtained using a JEOL JEM-2100 electron microscope with accelerating voltage of 200 kV. Optical absorption was recorded with SHIMADZU UV-2450 spectrophotometer. Photoluminescence emission (PL) and excitation (PLE) were taken on a SHIMADZU RF-5301 PC Spectrofluorometer. X-ray Excited Optical Luminescence (XEOL) was measured in a light-proof x-ray cabinet equipped with optic fiber connection to an outside detector. X-ray irradiation (90 kV and 5 mA) was performed using a Faxitron RX-650 X-ray cabinet (Faxitron X-Ray Corp., IL, USA). The luminescence spectra were recorded using a QE65000 spectrometer (Ocean Optics Inc., Dunedin, FL) connected to the X-ray chamber using a 600 μm core diameter, P600-2-UV-Vis fiber optic (Ocean Optics Inc., Dunedin, FL). XRD were recorded using a

Siemens Kristalloflex 810 D-500 X-ray diffractometer operating at 40 kV voltage and 30 mA current with a radiation beam of λ = 1.5406 Å. Fourier transform infrared spectroscopies (FTIR) studies were performed using Thermo Nicolet 6700 FTIR spectrometer.

5.3 Results and Discussion

The XRD pattern of oleic acid coated CeF_3 nanoparticles (OA-CeF_3) is shown in Figure 5-1 and matches with the hexagonal phase of crystalline CeF_3.

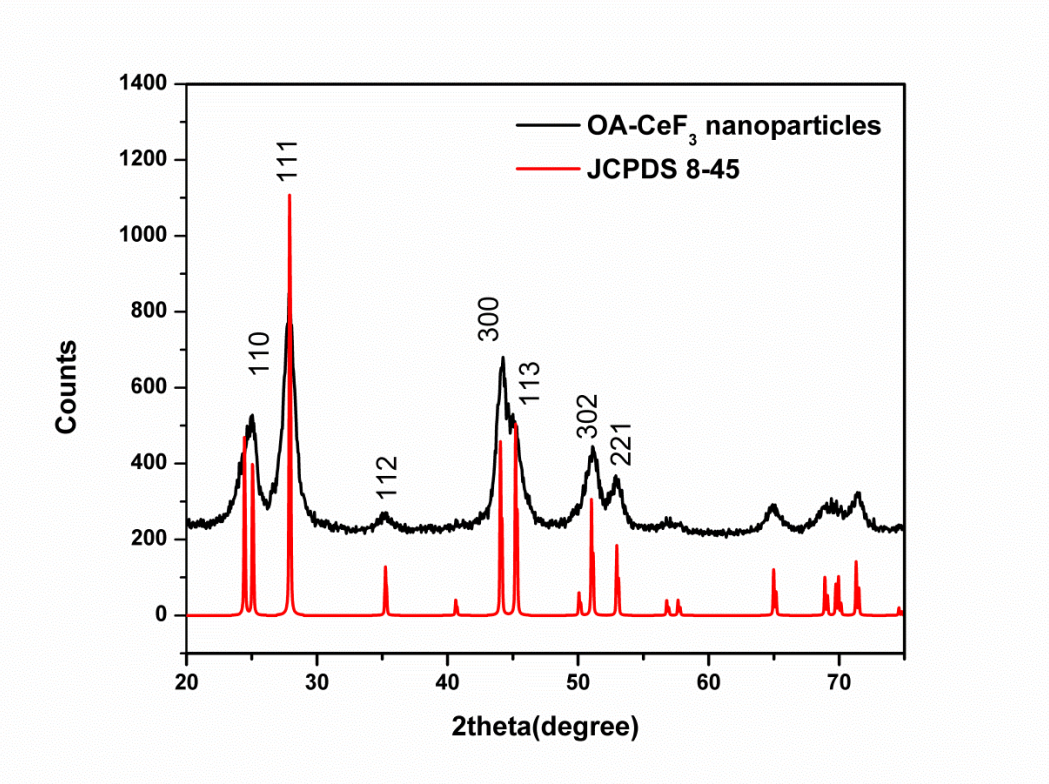

Figure 5-1 XRD pattern of oleic acid coated CeF3 nanoparticles.

The size of the nanoparticles was estimated using Scherrer equation. The size is estimated about 10 nm size using (111) XRD peak.

Figure 5-2(A) shows the TEM images of CeF_3 nanoparticles. The histogram shown in Figure 5-2(B) indicates that the average size of as-prepared CeF_3 nanoparticles is about 12 nm. The size of the nanoparticles estimated using XRD closely matches with the size obtained from TEM image. The presence of oleic acid on the nanoparticle surfaces not only significantly reduces the size of CeF_3 nanoparticles, but also enables the uniform dispersion of the nanoparticles into the polymer matrix. It was utilized to confine the growth of CeF_3 crystals so that small particle sizes can be achieved for minimizing light scattering.

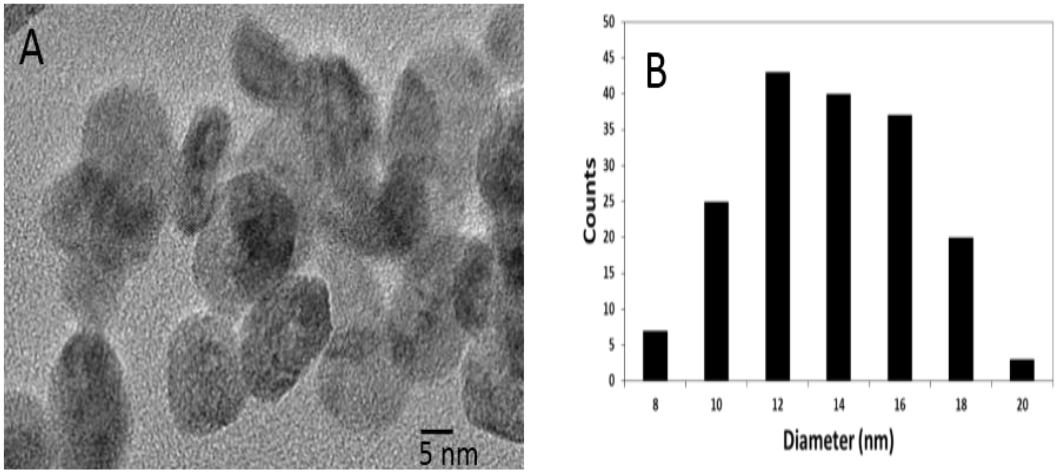

Figure 5-2 (A) TEM image of OA-CeF3 nanoparticles, (B) Size distribution of nanoparticles.

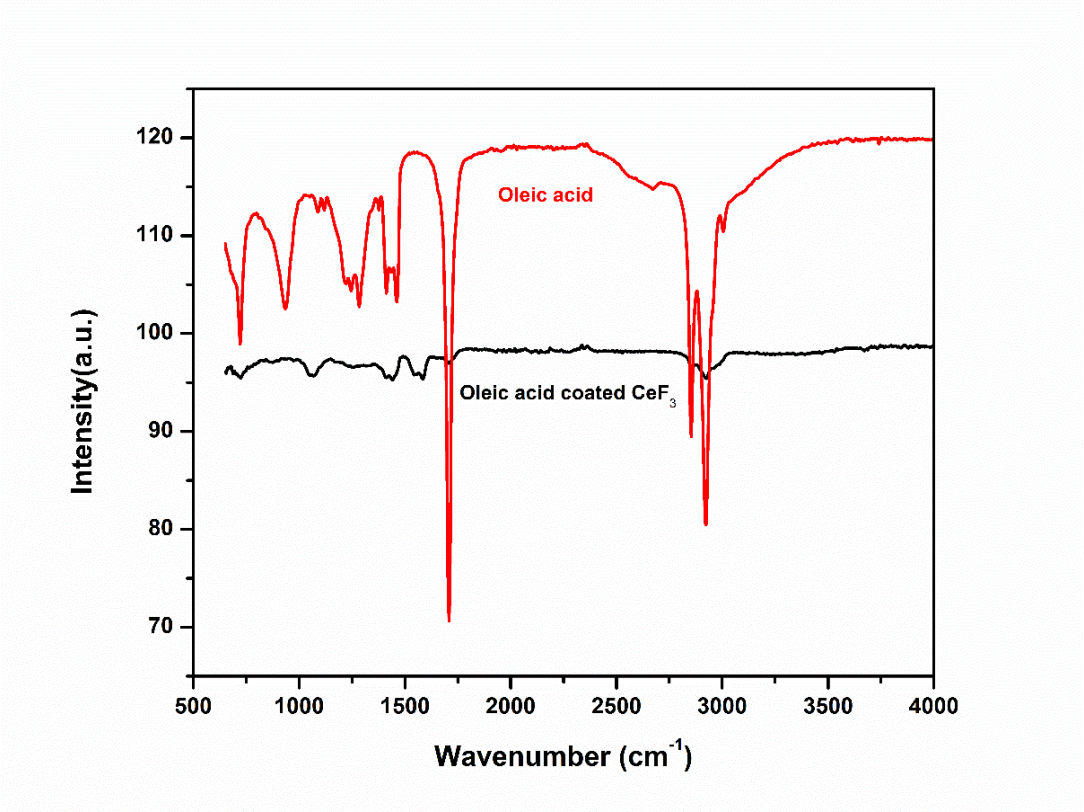

Figure 5-3 FTIR spectra of oleic acid and oleic acid coated nanoparticles.

Oleic acid coated CeF_3 nanoparticles were characterized using FTIR. FTIR spectra of oleic acid and oleic acid coated CeF_3 nanoparticles are shown in Figure 5-3. The absorption peak at 2925 and 2854 cm^{-1} are assigned to the asymmetric CH_2 stretch and the symmetric CH_2 stretch respectively in oleic acid. The infrared band at 1712 cm^{-1} is corresponds to the C=O stretching modes for dimeric COOH group. The FTIR spectrum of oleic acid coated CeF_3 nanoparticles shows some characteristics peaks of oleic acid. Moreover, the presence of some new absorption peaks at 1545 and 1590 cm^{-1} assigned to the asymmetric and symmetric COO- stretch confirms the oleic acid coating in CeF_3 nanoparticles.

Thermogravimetric analysis (TGA) of OA-CeF_3 and OA-CeF_3 loaded PVT is shown in Figure 5-4.

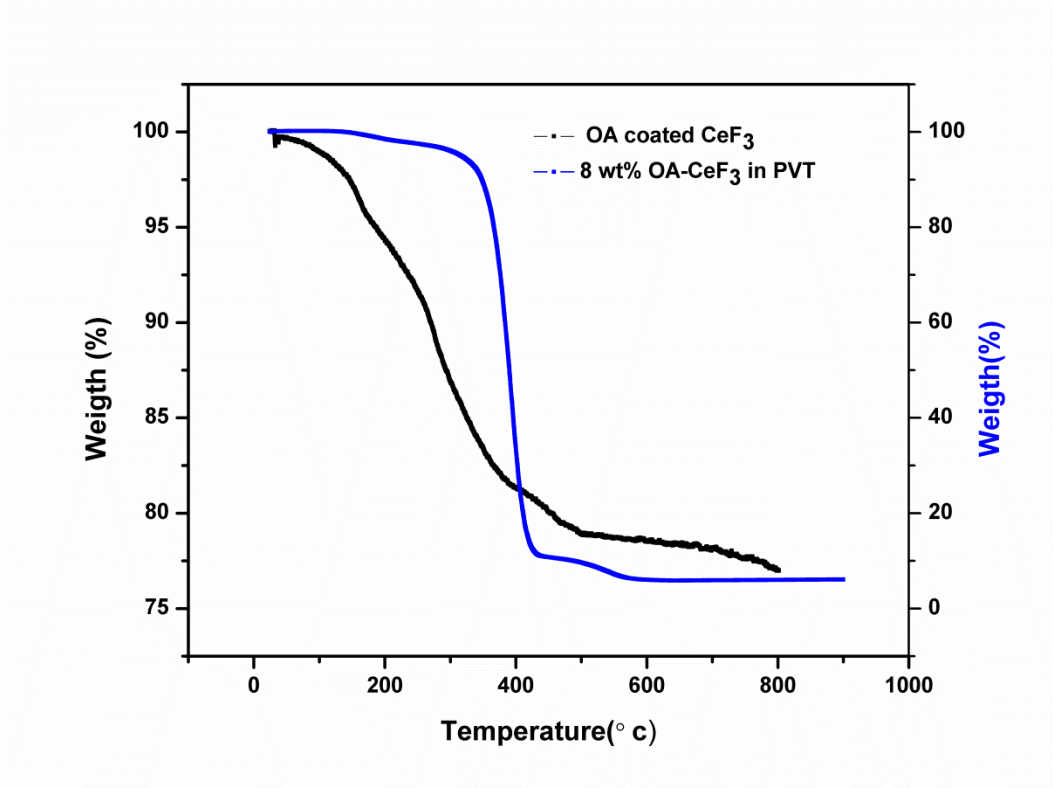

Figure 5-4 TGA spectra of oleic acid coated CeF3 and 8 wt% oleic acid coated CeF3 in PVT.

TGA of oleic acid coated CeF_3 nanoparticles show weight loss of 22 wt% when heated at 800 °C. This is further supported by the TGA spectra of nanoparticles loaded PVT nanocomposite. TGA spectra of 8 wt% nanoparticles loaded PVT show about 6 wt% residue weights, when heated at 900 °C.

Figure 5-5 shows photoluminescence emission (PL) and excitation (PLE) of CeF_3 nanoparticles along with the absorption spectrum of PPO/PVT. CeF_3 nanoparticle has an excitation peak at 290 nm and an emission peak at 330 nm. CeF_3 exhibits several excitation

bands, and the low energy one is centered about 250 nm when saturation effect is discarded. The emission of CeF_3 crystals is usually centered at 305 nm which is attributed to the *5d-4f* transition of the Ce^{3+} ion.[12, 63]. The emission at 330 nm in CeF_3 nanoparticles is mainly from surface states as pointed by Dujardin et al.[115]

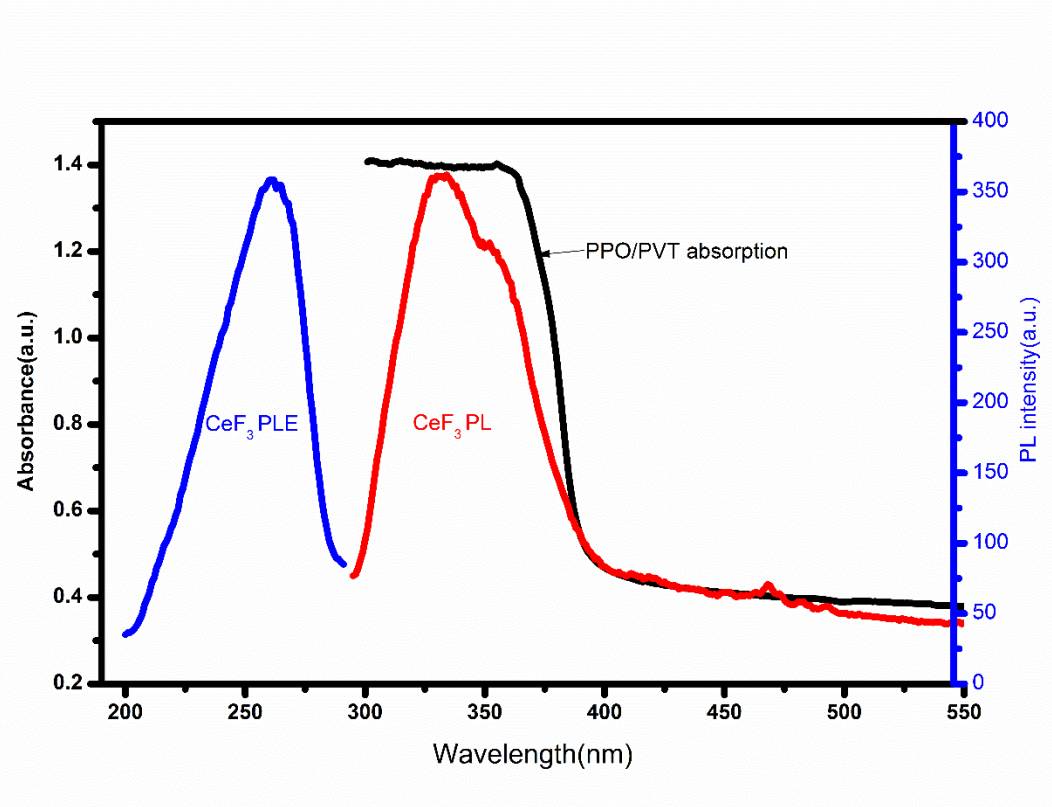

Figure 5-5 FRET overlapping of CeF3 emission and absorption of PPO/PVT.

The emission in CeF_3 nanoparticle overlaps with the absorption of PPO/PVT and fulfill the condition for FRET. It is expected that the energy can be transfer from CeF_3 nanoparticles to PPO/PVT due to this FRET overlapping. The lifetime of ~330 nm emission of CeF_3 is ~30 ns[12, 65], and that of PPO is 1.6 ns[116] as reported by various authors. These lifetimes also fulfill the criteria that the donor lifetime must be sufficient longer than

that of acceptor for FRET to occur. When being excited at 290 nm, PPO/PVT shows an emission band peaking at around 390 nm. In organic scintillator solute concentration of less than 2 wt% is use to avoid the luminescence quenching at higher concentrations. Figure 5-6 shows the photoluminescence of different concentration of PPO in PVT. In our measurement system 1 wt% PPO in PVT shows the highest photoluminescence. Hence, we have used 1 wt% PPO to fabricate the nanocomposite scintillators.

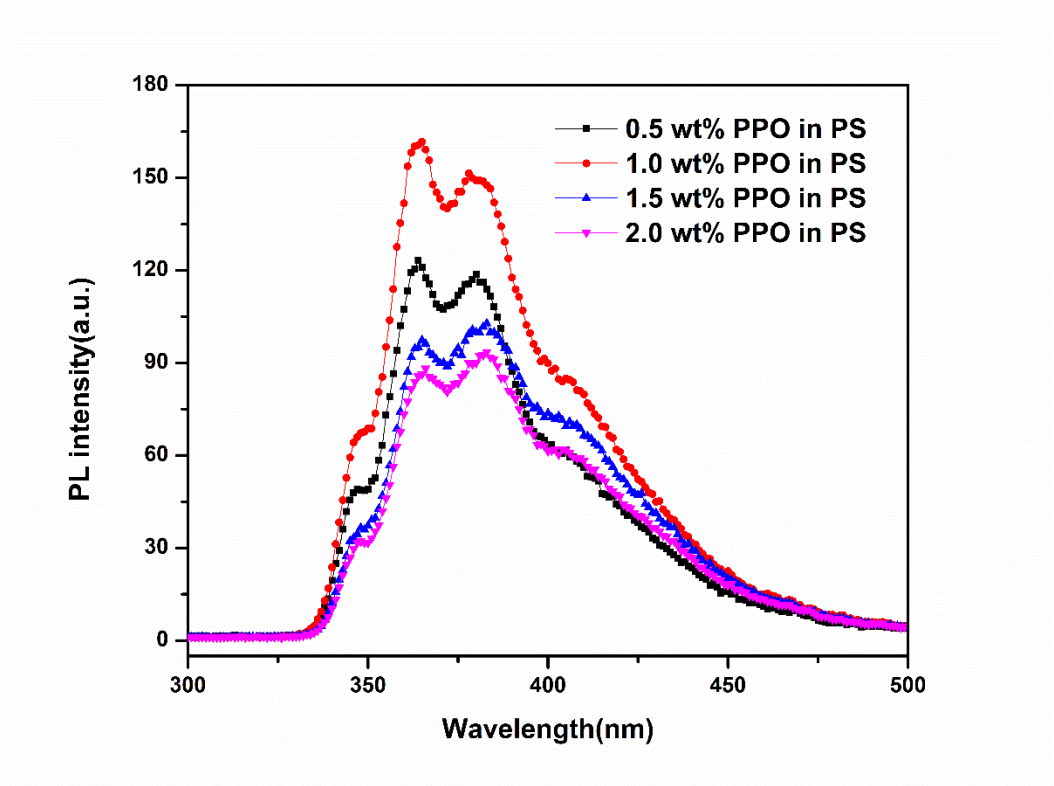

Figure 5-6 Photoluminescence of different concentration of PPO in PS.

To elucidate the enhancement effect of CeF_3 doping on the emission of PPO/PVT composites, different concentrations of CeF_3 nanoparticles are loaded into PVT matrix while the concentration of PPO was kept constant at 1 wt%. The room temperature photoluminescence spectra of nanocomposites excited at 290 nm are shown in Figure 5-

7. It is clear that CeF_3 nanoparticles significantly enhanced the photoluminescence of PPO/PVT composites. This enhancement in the emission intensity of nanocomposites loaded with CeF_3 nanoparticles is due to the energy transfer from CeF_3 to PPO in PVT matrix as expected. Also, there is no shift in PPO emission position in the nanocomposites. In addition, the photoluminescence spectra of CeF_3/PPO/PVT composites do not show any emission from CeF_3 nanoparticles when being excited at 290 nm wavelength, which further supported the argument that the enhancement in photoluminescence is due to the FRET from CeF_3 nanoparticles to PPO/PVT composite.

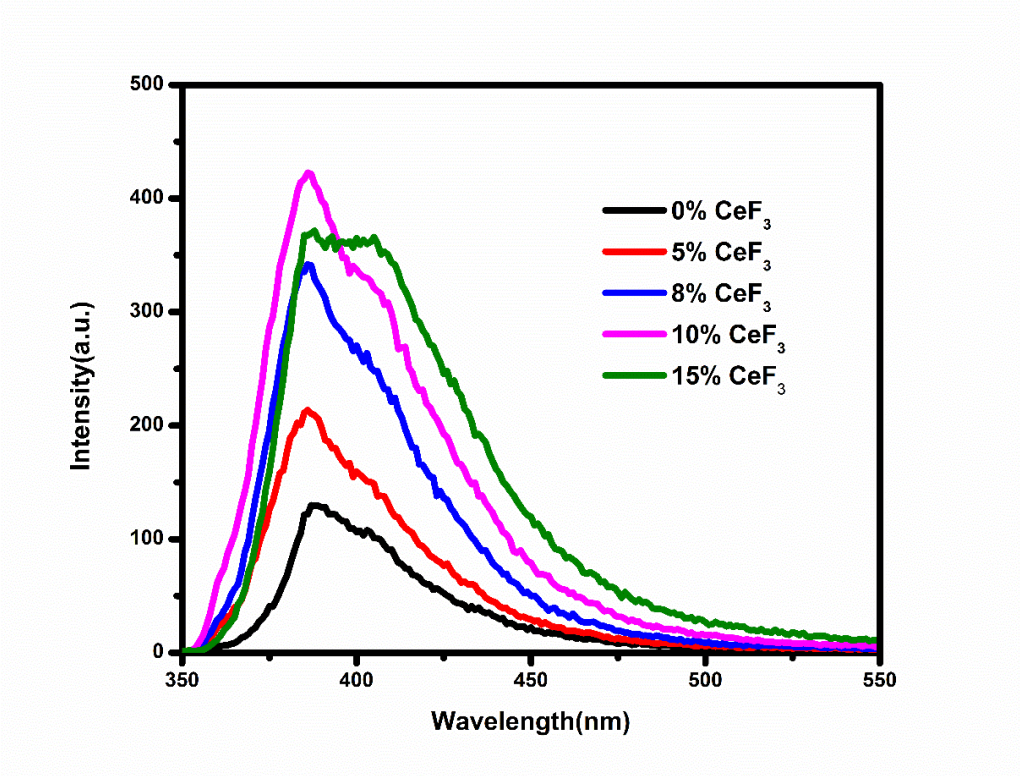

Figure 5-7 Photoluminescence of different concentration of oleic acid capped CeF3 nanoparticles and 1 wt% PPO in PVT.

Nanocomposites loaded with CeF_3 nanoparticles exhibited brighter emissions under UV-light as compared to the unloaded sample, as can be seen in Figure 5-8.

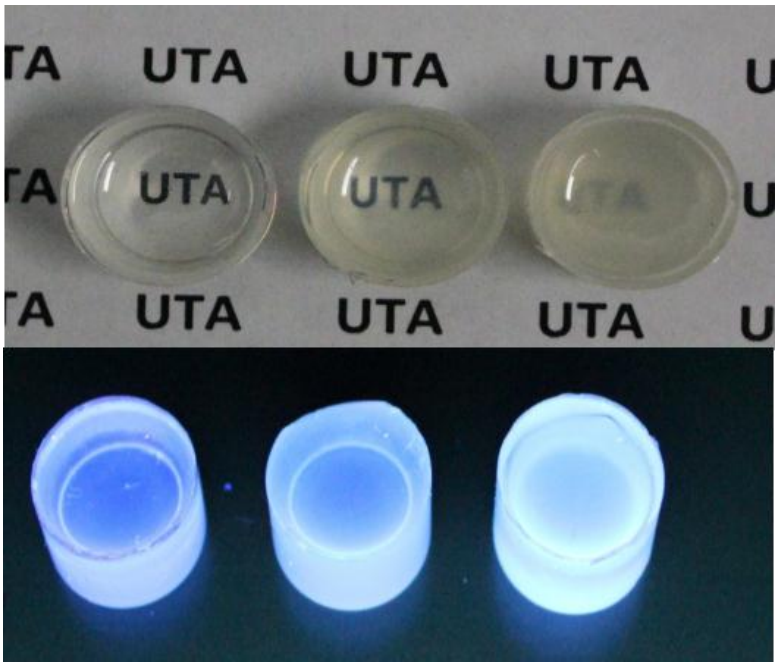

Figure 5-8 Pictorial image of CeF3 loaded (0 wt%, 5 wt% and 10 wt% from left to right) in PPO/PCT nanocomposite under normal light(top panel) and UV light (bottom panel)

The mechanism of energy transfer can be explained using the energy level diagram as shown in Figure 5-9. Upon irradiation with UV or X-ray, excitons are generated on CeF_3 nanocrystals. Since the emission of CeF_3 overlaps perfectly with the absorption of PPO in PVT, excitions on the nanoparticles can transfer its energy to PPO in PVT matrix as long as the distance between nanoparticles and fluor molecules reaches the critical radius as required by FRET principles.[117] Once excitons transfer their energy to PPO, it would recombine to give luminescence. Enhancement in PL is more than 3 times for the CeF_3 loading concentration of 10 wt % and then decreases to about 2.8 times for 15 wt %.

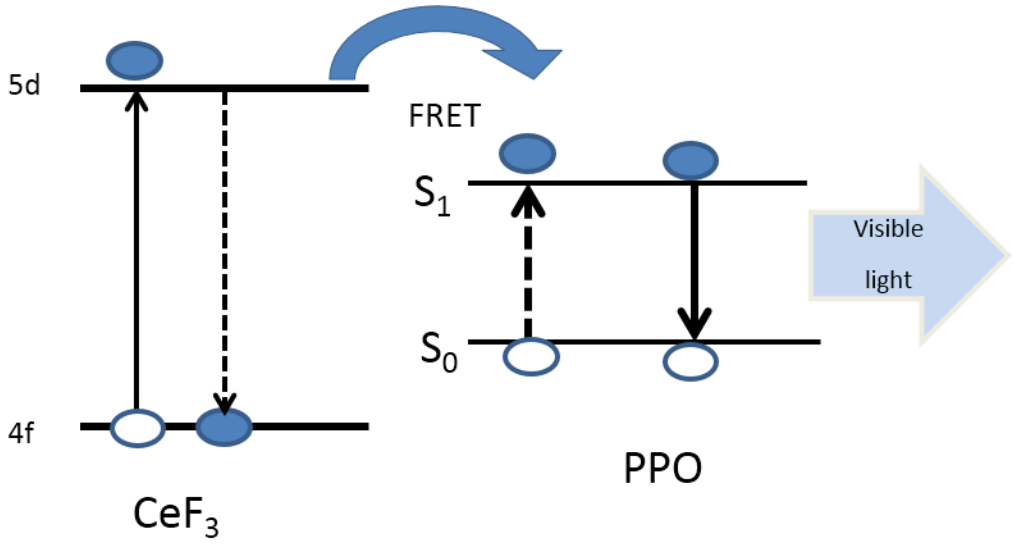

Figure 5-9 Schematic of energy transfer from CeF3 nanoparticles to PPO in PVT matrix.

This decrease in PL with higher loading concentration might be due to the increased population of the non-radiative triplet state or the loss of transparency of the nanocomposites at higher nanoparticle loading concentrations. As shown in Figure 5-8, the transparency of the nanocomposites decreases with increasing nanoparticle loading concentration.

Since the energy transfer mechanism is similar in case of both UV and X-ray excitation, we have used X-ray as an excitation source to provide further evidences of energy transfer in the nanocomposites, We have employed 90 kV X-ray as an excitation source to measure the X-ray Excited Optical Luminescence (XEOL) of the nanocomposites. Figure 5-10 shows the XEOL of nanocomposites with different nanoparticle loading concentrations. Again, enhanced luminescence was observed for

nanocomposites loaded with CeF_3 nanoparticles under X-ray excitation. This further strengthens the energy transfer evidence.

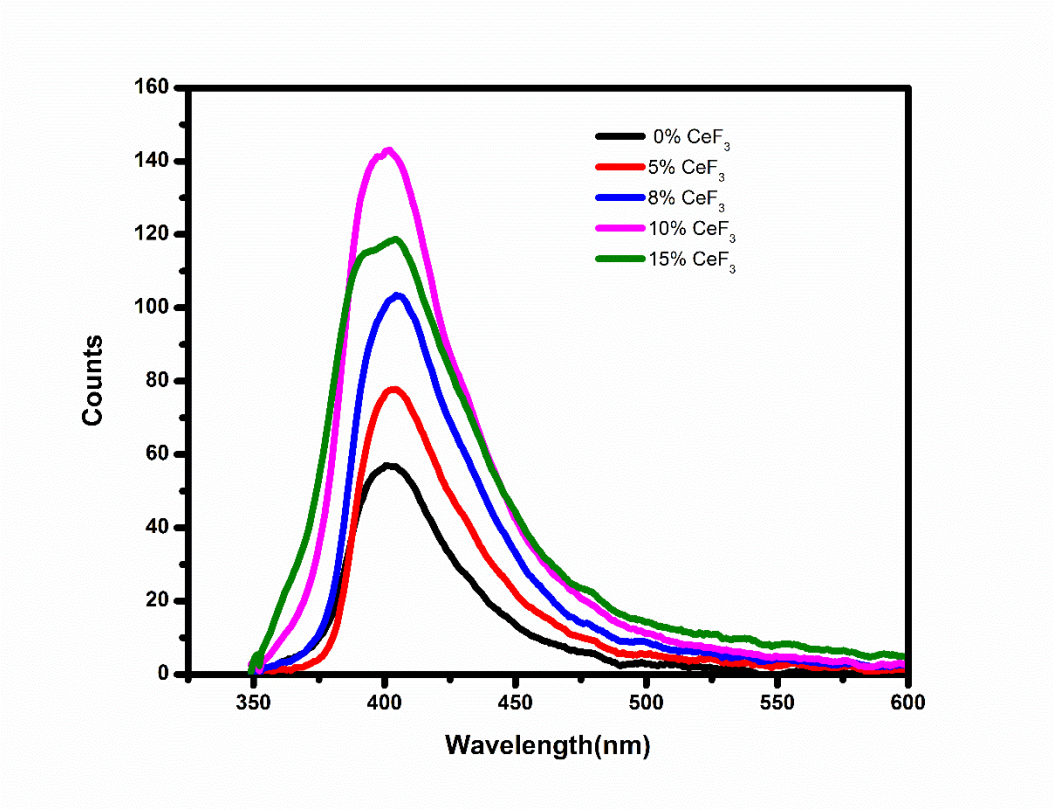

Figure 5-10 XEOL spectra of different concentration of CeF3 loaded PPO/PVT nanocomposite scintillators.

Also no CeF_3 emission is seen under X-ray excitation, which is due to the strong absorption of PPO/PVT composite in the region of CeF_3 emission. In case of X-ray excitation, the peak is red shifted by 10 nm in all the nanocomposites and enhancement is 2.5 times for the loading concentration of 10 wt % compared to only PPO/PVT composite, as shown in Figure 5-10. Again, at a higher nanoparticle loading concentration (15 wt %), the enhancement of XEOL decreased to 2.1 times as compared to the one without

nanoparticle. Thus, energy transfer from CeF_3 nanoparticle to PPO/PVT is observed when the nanocomposites are excited by both UV and X-ray source. It should be pointed out that, in addition to energy transfer, the increase of the stopping power by doping CeF_3 nanoparticles into PPO/PVT and the escape of charges from CeF_3 nanoparticles also contribute to the luminescence enhancement. For the same reasons, we believe the quenching of CeF_3 emission is due to energy transfer, self-absorption, charge escape as well as the surface modification when doped into PPO/PVT. Energy transfer is a complex process and more studies are necessary to prove the energy transfer and mechanism.

The fluorescence resonance energy transfer (FRET) process involves a pair of dissimilar fluorophores in close proximity, typically less than 10 nm apart. The shorter-wavelength fluorophore (donor) is directly excited with incident light, and then transfer's energy non-radiatively to the longer-wavelength fluorophore (acceptor), which then emits light. In this case, the excitation wavelength is chosen for maximum absorption by the donor, but the emitted light is characteristic of the acceptor. The magnitude of the FRET signal is extremely dependent on the separation between the fluorophores, and so can be used to monitor binding events and conformational changes. In the case of PPO/PVT by CeF_3, we believe the energy transfer is simply due to the absorption of the emission energy from CeF_3 nanoparticles by PPO/PVT organic scintillators. However, energy transfer is not the only reason for the luminescence enhancement or the quenching of CeF_3 luminescence. More studies are needed in order to understand the optical processes occurred in these materials.

For scintillation measurement, sample of dimension (Ø 20 X 8 mm) was prepared, with and without nanoparticles loading. Scintillation response was measured for Cs-137 gamma source with acquisition time of 300s. The pulse height spectrum of nanocomposite scintillator is shown in Figure 5-11.

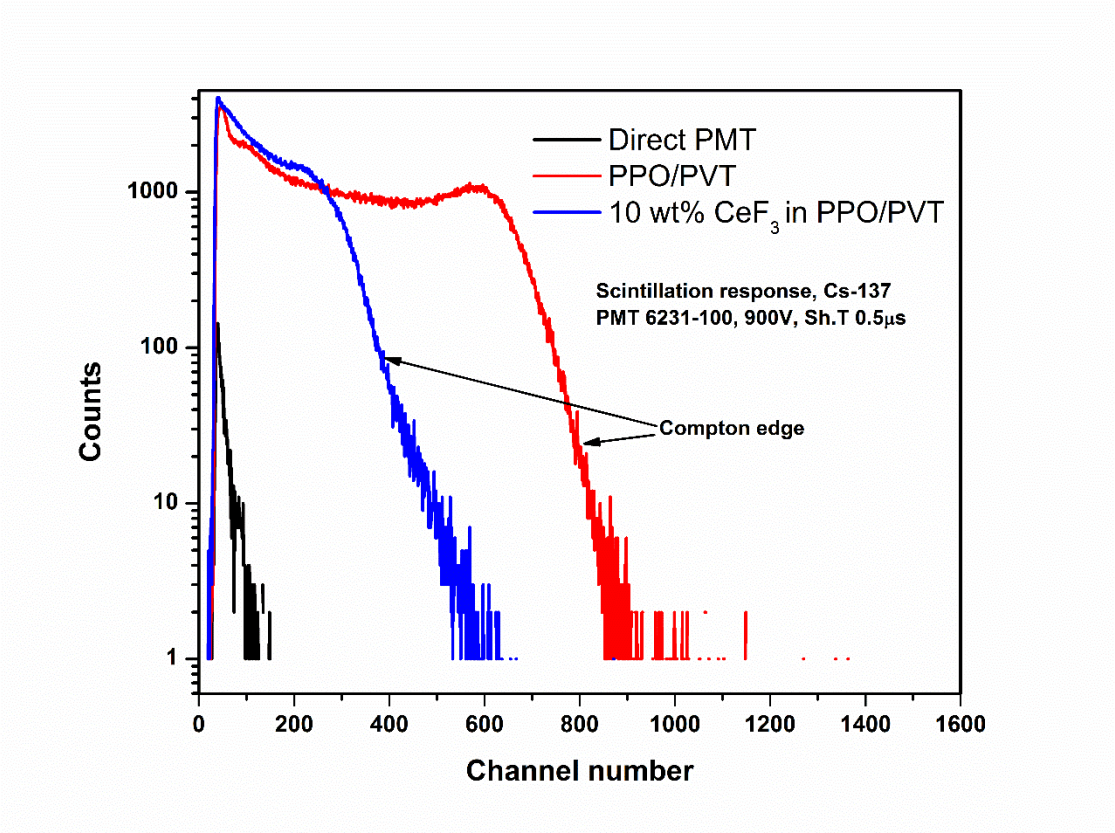

Figure 5-11 Pulse height spectra of Cs-137 obtained using PPO/PVT and CeF3 loaded PPO/PVT nanocomposite scintillator.

Pulse height spectra didn't show any sign of photopeak (662 keV) with nanoparticles free and nanoparticles loaded sample. However, the Compton edge can be seen with both PPO/PVT and CeF_3 loaded PPO/PVT nanocomposite scintillators. However, CeF_3 loaded nanocomposite scintillator exhibits lower scintillation counts compared to one without nanoparticles. This could be due to the increase in light scattering due to the loss of transparency at 10 wt% nanoparticles loading. Also, photoluminescence and XEOL studies showed luminescence quenching at higher than 10 wt% nanoparticles loading.

Figure 5-12 shows the scintillation decay time of nanoparticles free and 10 wt% CeF_3 loaded sample at Cs-137 (662 keV) gamma excitation. Decay time was calculated by exponential fitting of the experimental data. Decay time of 10.96 ns and 10.35 ns were calculated for nanoparticles free and 10 wt% CeF_3 loaded PPO/PVT nanocomposite scintillators. This shows nanocomposite scintillator with fast decay time can be achieved by loading nanoparticles in PPO/PVT.

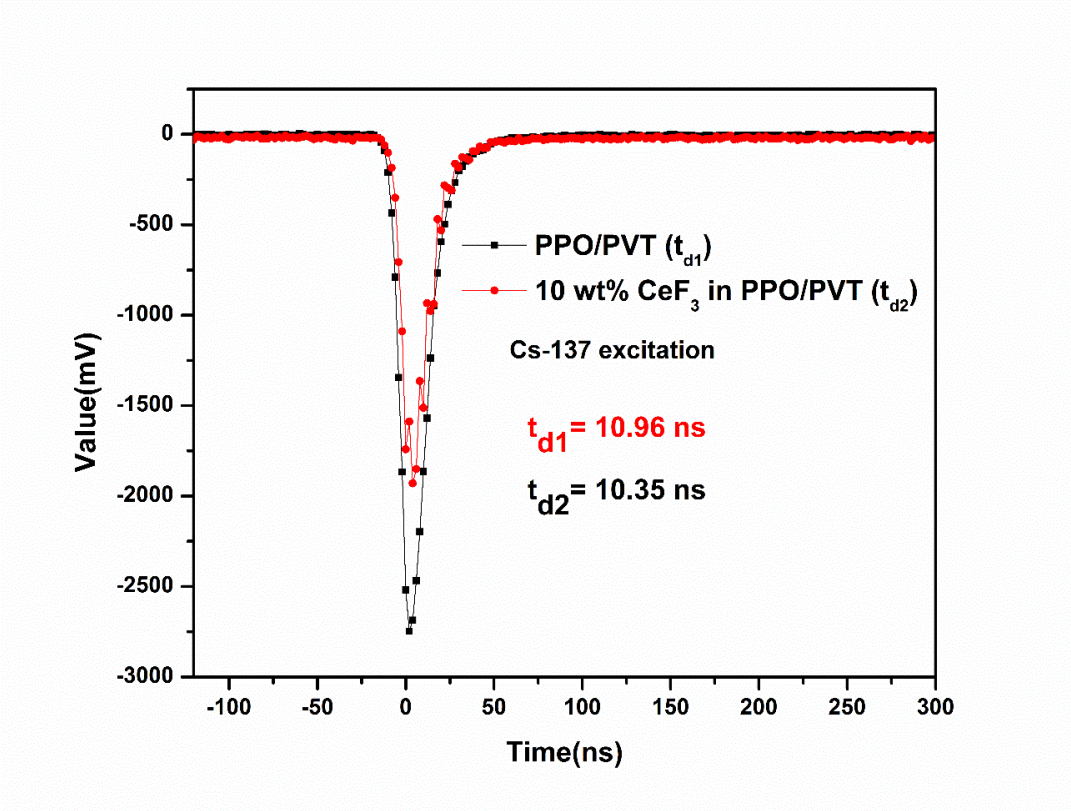

Figure 5-122 Scintillation decay time of PPO/PVT and 10 wt% CeF3 loaded PPO/PVT nanocomposite scintillator.

5.4 Summary

Oleic acid coated CeF_3 nanoparticles were synthesized with emission at 330 nm which is from the 5d-4f transition in Ce^{3+} ion. Enhanced luminescence is observed in PPO/PVT scintillators when embedded with CeF_3 nanoparticles. Enhancement in the PL is more than 3 times for 10 wt % of CeF_3 loading whereas enhancement is 2.5 times when X-ray is used as excitation source for the same nanoparticles loading concentration. The luminescence enhancement in PPO/PVT by CeF_3 nanoparticles is attributed to the energy transfer, the increase of the stopping power by doping CeF_3 nanoparticles as well as the escape of charges from CeF_3 nanoparticles. The observations provide a new method to improve PPO/PVT organic scintillators for radiation detection. However, the nanocomposites suffer loss of transparency at higher loading concentration, resulting in loss of scintillation photos due to light scattering. The low nanoparticle loading level affects the stopping power of the nanocomposite. For scintillation applications, higher nanoparticles loading are desirable to increase the Z- value and density of nanocomposite. To improve the nanoparticles loading level, a new approach was taken to coat the nanoparticles surface, resulting in nanoparticles with high dispersion into polymer matrix, which will be discussed in next chapter.

Chapter 6

Synthesis of $La_xCe_{1-x}F_3$ Nanocomposite Scintillator for Gamma Ray Spectroscopy

6.1 Introduction

Inorganic single crystals and organic plastic scintillators are the most common types of scintillators. Inorganic single crystals are preferred over organic plastic scintillators for gamma spectroscopy.[63, 118, 119] This is due to the better gamma stropping power of inorganic single crystal scintillators which arises as a result of high effective atomic number and high density.[8, 120] However, inorganic single crystals are difficult to grow in large size and thus expensive.[50, 121, 122] On the other hand, organic plastic scintillators are attractive due to its fast decay time and ease of fabrication.[42, 123] However, its application in gamma spectroscopy is limited due to its poor energy resolution. The poor energy resolution of organic plastic scintillator is due to its low density and low effective atomic number (Z_{eff}). In the past, studied have been done to increase the density of organic plastic scintillators by loading high–Z organometallic compound with limited success.[7, 24-29, 124] Recently, Rupert et al. demonstrated enhanced gamma stopping power using bismuth organometallic compound as a high density filler in polyvinylcarbazole polymer.[30] However, it has been reported that high – Z organometallics compound are thermally unstable.[31, 32]

In the last decade, inorganic nanoparticles and quantum dots has been heavily studied as a filler to increase the density of plastic scintillators.[33-38] However, no reports have been found on sufficient loading of quantum dots to produce the photo peak under gamma excitation. Also, most of the quantum dots embedded nanocomposites emit in the region where the quantum efficiency of commonly used photomultiplier tubes (PMTs) are low.[42-44] Rare earth based nanoparticles are also heavily studied for scintillation

applications. Feller et al. used oleic acid as an organic matrix to synthesized $Ce_xLa_{1-x}F_3$ nanocrystals embedded transparent nanocomposite.[45] However, the low mechanical strength of oleic acid matrix limits its application. Kang et al. used similar method to synthesized oleic acid coated BaF_2-Ce nanophosphors and embedded into epoxy matrix.[46] However, the nanocomposites showed significant loss of transparency at nanoparticles loading concentration of less than 10 wt%. We have previously reported luminescence enhancement in PPO/PVT scintillator by embedding oleic acid coated CeF_3 nanoparticles under UV and X-ray excitation.[47] However at loading concentration higher than 10 wt%, nanocomposites lose transparency resulting in diminished light yield. Cai et al. fabricated nanocomposite scintillator by embedding non-fluorescent Gd_2O_3 nanocrystals in PVT matrix. The nanocomposite are highly transparent even at high nanoparticles loading concentration of 31 wt% and exhibit a beta light yield more than twice that of conventional plastic scintillator. It was suggested that the wide band gap of Gd_2O_3 gamma photosensitizer helps to avoid the luminescence quenching in nanocomposites.[32] However, the nanocomposite emit in green region where the quantum efficiency of commonly used photomultiplier tubes (PMTs) is low. Recently, Liu et al. fabricated nanocomposite for gamma ray spectroscopy by embedding HfO_2 nanoparticles in PVT matrix. The nanocomposite exhibit high light transmittance even at a loading concentration as high as 40 wt%. The nanocomposite loaded with 20 wt% HfO_2 produced a deconvoluted photopeak with energy resolution ≤ 8% for 662 keV Cs-137 gamma radiations.[48] It was suggested that the high Z- value of Hf resulting in increased photoelectric cross-section is responsible for the production of photopeak. However, it was reported that the gamma light yield and photopeak resolution did not improve with large size nanocomposite or with the higher nanoparticle loading. Also, the measurement was done at acquisition time of 4 h.

In this paper we have used a different approached to fabricate blue emitting nanocomposite scintillator. We have studied $La_xCe_{1-x}F_3$ luminescent nanoparticles as high density filler to increase the density and Z_{eff} of plastic scintillator for gamma ray spectroscopy. We have used polymerizable surfactant as a surface coating agent to improve the dispersibility of $La_xCe_{1-x}F_3$ nanoparticles in styrene. Polymerizable surfactant octadecyal-p-vinylbenzyldimethylammonium chloride (OVDAC) has been used to extract CdTe quantum dots (QDs) from water to monomer and eventually copolymerization with free-radical monomer to fabricate QDs-polymer nanocomposites.[125-127] However, the method is limited to specific quantum dots and did not worked for $La_xCe_{1-x}F_3$ nanoparticles. In this paper, we have used polymerizable surfactant hexadecyl-*p*-vinylbenzyldimethylammonium chloride (HVDAC) and synthesized $La_xCe_{1-x}F_3$ nanoparticles in presence of HVDAC as surface coating agent. The long hydrocarbon chain in HVDAC makes the resulting HVDAC coated $La_xCe_{1-x}F_3$ nanoparticles highly dispersible in styrene. The free radical bulk polymerization is used to copolymerize HVDAC coated nanoparticles with styrene to obtained nanocomposites loaded with high concentration of $La_xCe_{1-x}F_3$ nanoparticles.

$La_xCe_{1-x}F_3$ nanoparticles were used in this study due to its large band gap and photoemission that overlaps with the absorption of 2,5- diphenyloxazole (PPO), which is a common scintillation dye used in plastic scintillators. This enables the energy transfer between $La_xCe_{1-x}F_3$ and PPO resulting in enhanced light yield. Wavelength shifting dye 1,4-bis(5-phenyloxazol-2-yl) benzene (POPOP) is used to shift the emission in the region of high quantum efficiency of PMT and also to reduce the self- absorption process.

6.2. Experimental

6.2.1. Synthesis of polymerizable surfactant hexadecyl-p-vinylbenzyldimethylammonium chloride (HVDAC)

HVDAC was synthesized using similar procedure reported by Zhang et al.[126] 20 mmole N, N- Dimethylhexadecylamine and 22 mmole 4-vinylbenzyl chloride was added to 12 ml acetone under vigorous stirring and refluxed at 40 °C for 2 hrs. The obtained product was cooled down to room temperature, washed with acetone for 4 times to remove any unreacted chemicals and dried under vacuum at 25 °C for 48 hrs. The final product was characterized using Fourier transform infrared spectroscopy (FTIR).

6.2.2. Synthesis of HVDAC capped $La_xCe_{1-x}F_3$ nanoparticles

HVDAC capped $La_xCe_{1-x}F_3$ nanoparticles were synthesis using a simple wet chemistry method. First, 900 mg HVDAC is dissolved in the 70 ml ethanol. In a separate beaker 18 mmole ammonium fluoride is dissolved in 50 ml DI water and mixed with HVDAC-ethanol solution under vigorous stirring. The water-ethanol solution was reflux at 80 °C for 1.5 hrs. Finally 6 mmole nitrate salts were dissolved in 10 ml DI water and added dropwise to the refluxed solution and further heated at 80 °C for 4 hrs. After completion of the reaction, the final product was cooling down to room temperature and washed 5 times with acetone and ethanol and dried at 45 °C.

6.2.3 Fabrication of nanocomposites

In the first step, styrene received from sigma-aldrich were run through a silica column to remove the inhibitor. To fabricate PPO/POPOP/PS nanocomposite, desired amount of PPO (1 wt%) and POPOP (0.05 wt%), 20 µl Luperox 231 and styrene were added to a glass vial and ultra-sonicated for 10-15 mins. Luperox 231 was added as an

initiator for thermally initiated free radical bulk polymerization process. The glass vials were then incubated at 65-70 °C for 3 days. Finally, the samples can be obtained by cooling down to room temperature and removing the samples from the glass vials. To fabricate $LaxCe1_{-x}F_3$/PPO/POPOP nanocomposites, everything is similar except HVDAC coated $La_xCe_{1-x}F_3$ nanoparticles were added along with PPO and POPOP.

6.2.4. Characterizations

Phase composition of the as synthesized HVDAC coated $La_xCe_{1-x}F_3$ nanoparticles was examined using X-ray diffraction (Bruker D8 Advance, USA). Transmission electron microscope (JEOL 1200EX) was used to determine the size of $La_xCe_{1-x}F_3$ nanoparticles. Photoluminescence emission (PL) and excitation (PLE) were measured on a SHIMADZU RF-5301 PC Spectrofluorometer. Fourier transform infrared spectroscopies (FTIR) studies were performed using Thermo Nicolet 6700 FTIR spectrometer. Thermogravimetric analysis were perform using SDT Q600 V20.9 Build 20. The scintillation response to gamma 662 KeV (Cs-137) was measured using a super bi-alkali Hamamatsu PMT R6231-100 biased at 900V. PMT output was further amplified with Hamamatsu preamplifier C6438 and shaped with a spectroscopy Ortec amplifier Model 671. Multi-channel analyzer was a Canberra MPII. Scintillation timing was measured using gamma excitation (Cs-137) and PMT at 900V and output of the preamplifier applied to a digital oscilloscope (Picotech).

6.3. Results and Discussion

Figure 6-1 shows the schematic of nanoparticles surface coating and copolymerization of HVDAC with styrene. HVDAC is synthesized by alkylation of N, N-dimethylhexadecylamine with 4-vinylbenzyl chloride. HVDAC coated La0.6Ce0.4F3 nanoparticles were synthesized using a simple one step wet chemistry method as describe

in the experimental section. The as synthesized nanoparticles were washed several times with acetone and ethanol to remove all the unreacted HVDAC. $La_{0.6}Ce_{0.4}F_3$ nanoparticles were then dried at 50 °C for further studies.

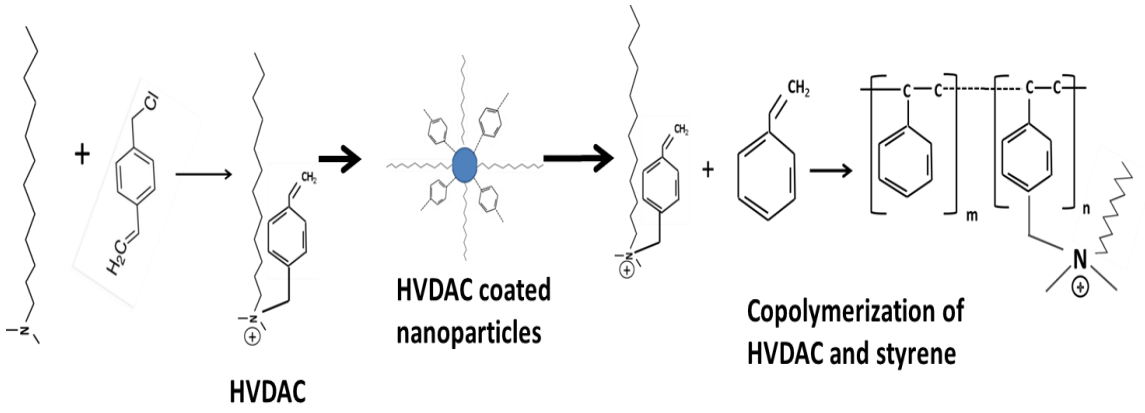

Figure 6-1 Schematic of the synthesis of HVDAC coated nanoparticles and copolymerization of HVDAC coated nanoparticles with styrene.

The phase structure of $La_{0.6}Ce_{0.4}F_3$ nanoparticles were examined using X-ray diffraction (XRD) as shown in Figure 6-2. XRD pattern of HVDAC coated $La_{0.6}Ce_{0.4}F_3$ nanoparticles matches well with the JCPDS 32-0483 profile of LaF_3-Ce with hexagonal phase structure. The peak broadening in the XRD pattern is due to the small size of the nanoparticles.

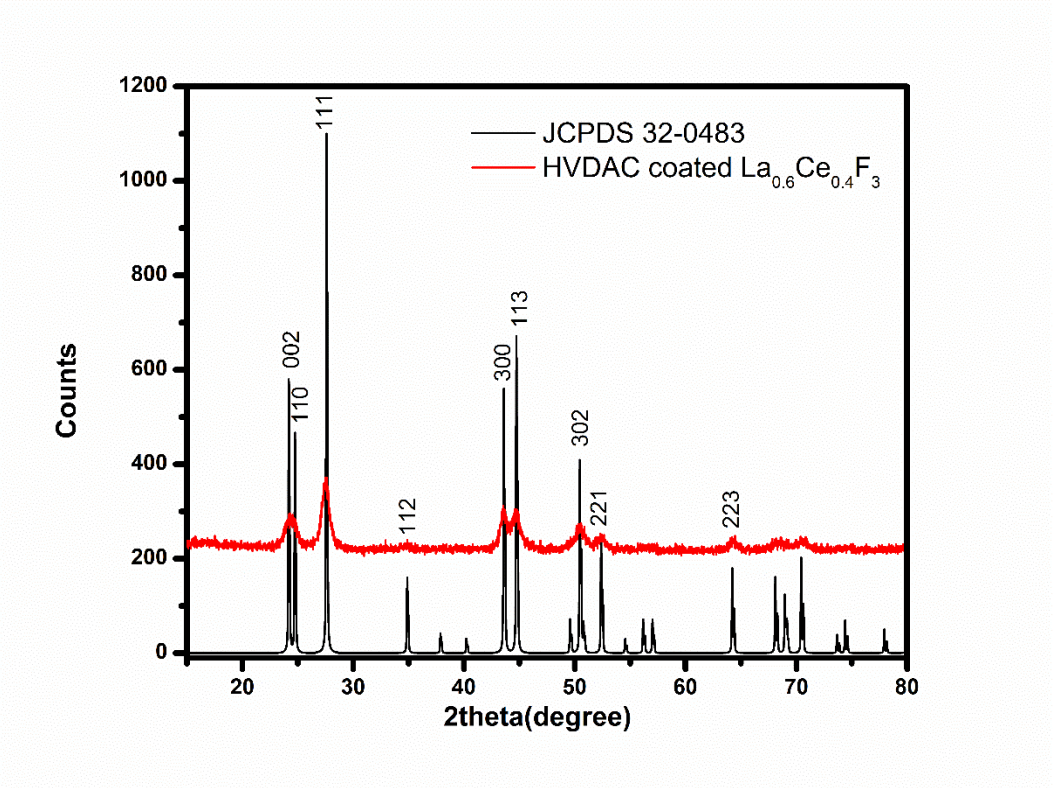

Figure 6-2 XRD pattern of HVDAC coated La0.6Ce0.4F3 nanoparticles and JCPDS reference file.

The size of the $La_{0.6}Ce_{0.4}F_3$ nanoparticles were estimated using the Scherrer equation, $D = K\lambda / \beta \cos\theta$, where D is the average size of the particles, K is a dimensionless shape factor (typical value of K is 0.9, same value is used for size calculation here), λ is the wavelength of X-ray (1.5406 Å for Cu K-alpha), θ is the diffraction angel and β is FWHM of an observed peak. The average size of the $La_xCe_{1-x}F_3$ nanoparticles were estimated about 11.7 nm using (111) peak. The as synthesized nanoparticles are assumed to be coated with HVDAC during the reaction period. To confirm the HVDAC coating on the nanoparticles surface, we have perform the Fourier transform infrared spectroscopy (FTIR) measurements of the as synthesized $La_{0.6}Ce_{0.4}F_3$ nanoparticles and compared with FTIR

spectrum of HVDAC used for the nanoparticles synthesis. FTIR spectra of HVDAC and HVDAC coated $La_{0.6}Ce_{0.4}F_3$ nanoparticles are presented in Figure 6-3.

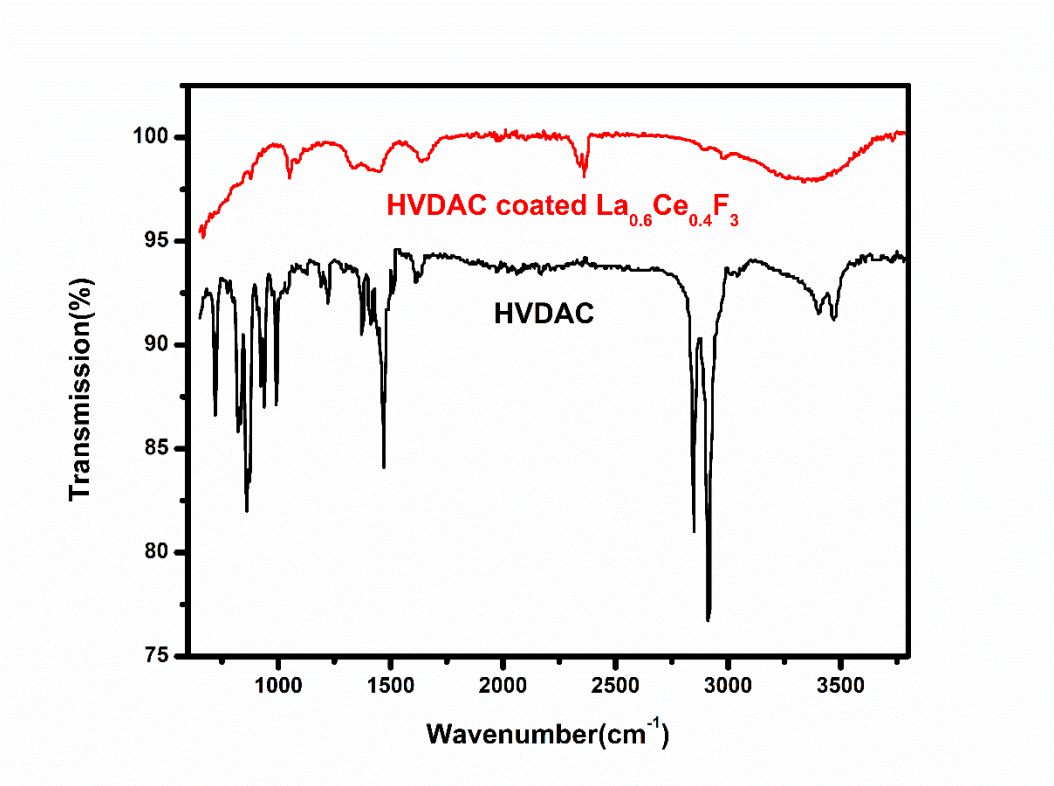

Figure 6-3 FTIR spectra of HVDAC and HVDAC coated La0.6Ce0.4F3 nanoparticles.

The peaks at 3400 and 3475 cm-1 are assigned to the N-H symmetric and asymmetric stretch. The peaks at around 2915, 2850 and 1475 cm-1 in FTIR spectra of HVDAC can be assigned to the CH2 stretching vibration of alkyl chain in HVDAC. The absence of N-H stretch in HVDAC coated La0.6Ce0.4F3 nanoparticles and the presence of characteristic absorption peaks of HVDAC in as synthesized $La_{0.6}Ce_{0.4}F_3$ nanoparticles confirms the HVDAC coating during the nanoparticles synthesis. The size of the HVDAC

coated nanoparticles were observed with Transmission electron microscopy (TEM) as shown in Figure 6-4. TEM image of the as synthesized HVDAC coated $La_{0.6}Ce_{0.4}F_3$ nanoparticles shows uniform size distribution with average size around 12 nm. The size obtain from TEM matches quite well with the size estimated from the XRD peak.

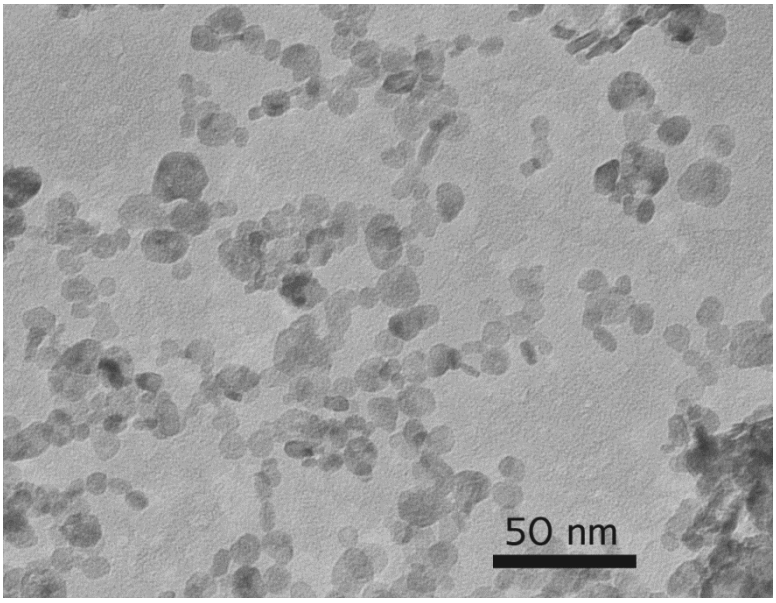

Figure 6-4 TEM image of HVDAC coated La0.6Ce0.4F3 nanoparticles.

The smaller size of the nanoparticles is due to the HVDAC coating on the surface of $La_{0.6}Ce_{0.4}F_3$ nanoparticles. We have performed the thermogravimetric analysis (TGA) to determine the content of HVDAC on the nanoparticles surface. TGA data of HVDAC coated $La_{0.6}Ce_{0.4}F_3$ nanoparticles are shown in Figure 6-5. TGA data shows weight loss of 10 % upon heating to1000 °C under nitrogen atmosphere. This shows HVDAC content of the as synthesized $La_{0.6}Ce_{0.4}F_3$ nanoparticles is less than 10 %. This is further supported by the

TGA data of 27 wt% $La_{0.6}Ce_{0.4}F_3$ nanoparticles loaded polystyrene monolith which shows about 24 wt% residues when heated at 1000 °C.

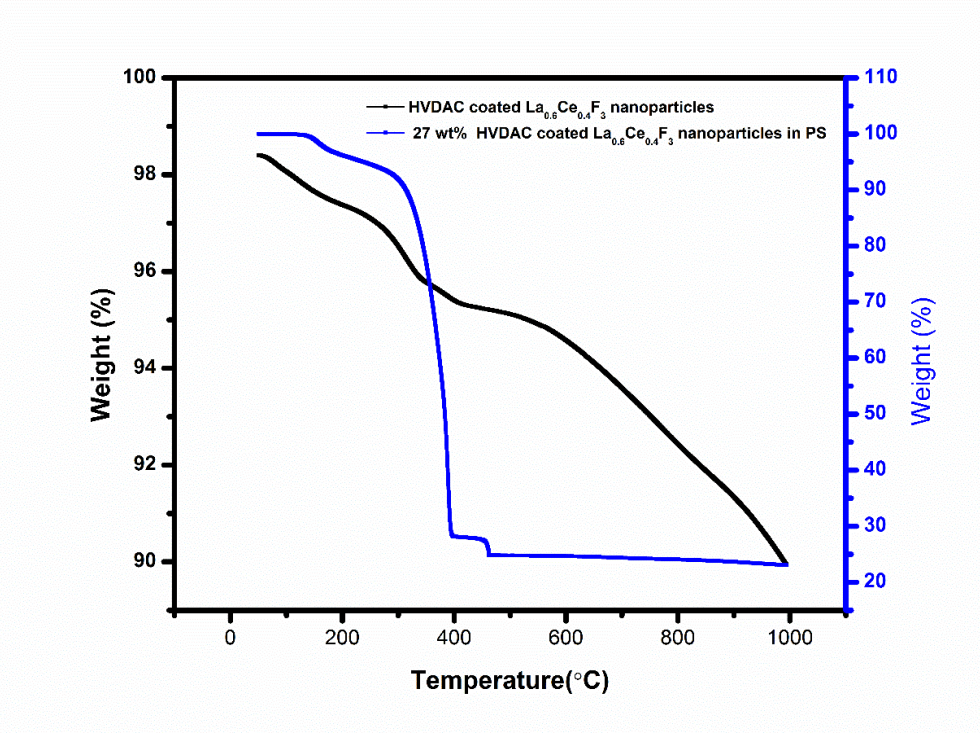

Figure 6-5 TGA spectra of HVDAC coated La0.6Ce0.4F3 nanoparticles and 27 wt% HVDAC coated La0.6Ce0.4F3 nanoparticles in polystyrene.

The photoluminescence of the as synthesized $La_{0.6}Ce_{0.4}F_3$ nanoparticles is shown in Figure 6-6. Photoluminescence measured at 280 nm excitation shows an emission band with peak about 318 nm. This emission is attributed to the *5d-4f* transition of the Ce^{3+} ion as reported by several authors in $La_xCe_{1-x}F_3$.[50, 104]

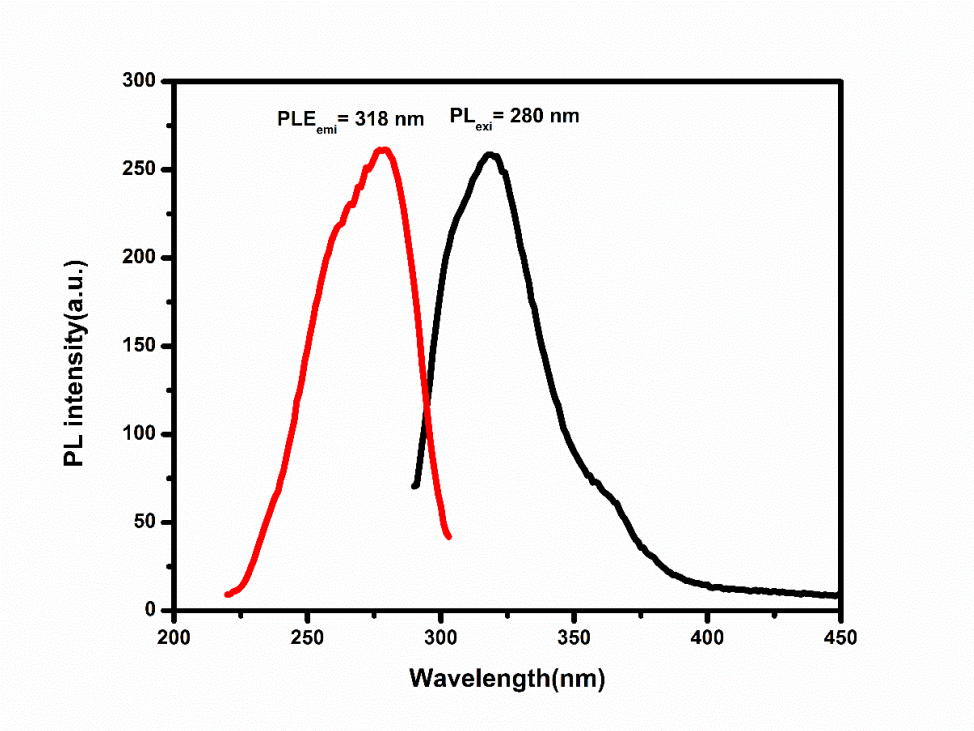

Figure 6-6 Photoluminescence emission and excitation spectra of HVDAC coated La0.6Ce0.4F3 nanoparticles.

The purpose of the nanoparticles loading in polystyrene (PS) with scintillating dye PPO and POPOP is to increase of density and effective atomic number (Z_{eff}) of the composite to convert an incident gamma-ray energy into photoelectrons. The incident gamma ray photon will excite a primary electron and populate one of the many excited states. The energetic photoelectron may de-excite to a lower energy level and in the process excite the nearby electrons through inelastic electron-electron scattering forming an electron cascade with in the PS matrix. This energy is then transfer to the primary dye PPO through fluorescence resonance energy transfer (FRET) resulting in photon emission. The FRET energy transfer is possible as the emission from $La_{0.6}Ce_{0.4}F_3$ nanoparticles as well as emission from PS matrix matches well with the absorption of PPO dye as shown in Figure 6-7. Wavelength shifter dye POPOP is added in the nanocomposite system to

reduce the luminescence quenching due to self-absorption as a result of small stokes shift in PPO.

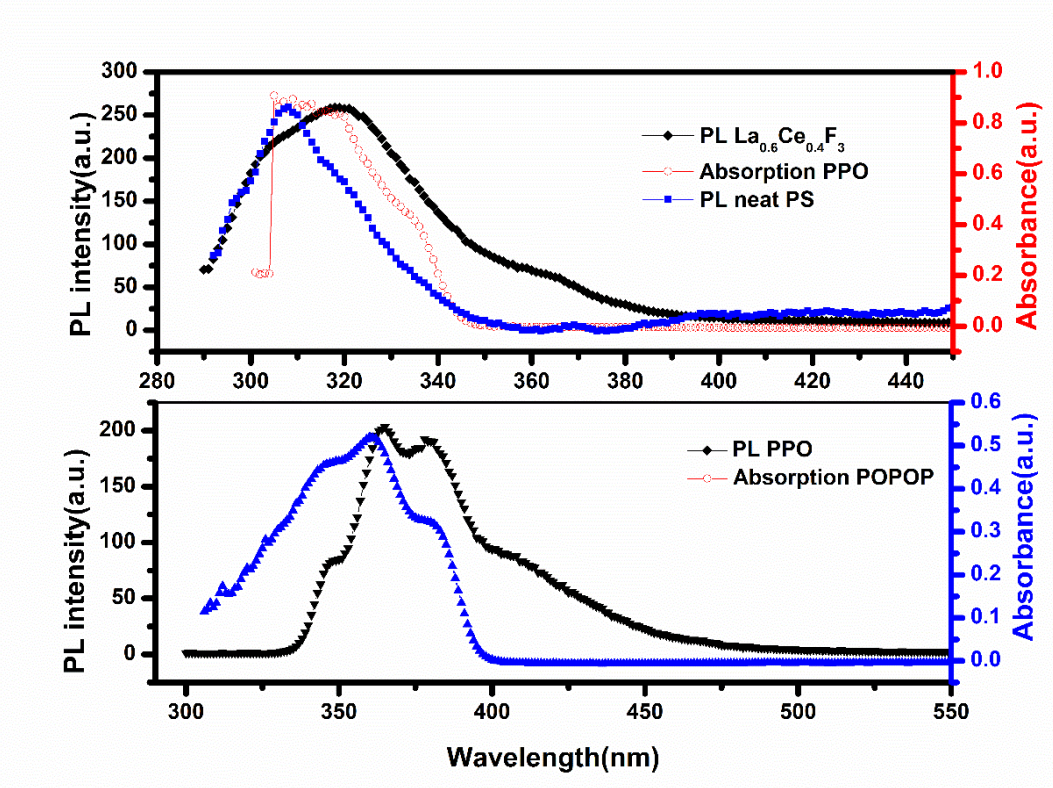

Figure 6-7 (Top) FRET spectral overlap between emission of PS and La0.6Ce0.4F3 nanoparticles and absorption spectra of PPO, (Bottom) spectral overlap between emission of PPO and absorption of POPOP.

Again the absorption of POPOP overlaps with the PPO emission fulfilling the condition for energy transfer from PPO to POPOP as shown in Figure 6-7. As a result of this FRET energy transfer from bulk part which includes $La_{0.6}Ce_{0.4}F_3$ nanoparticles in PS to PPO and eventual energy transfer to POPOP, the nanocomposite exhibits only POPOP emission at $La_{0.6}Ce_{0.4}F_3$ nanoparticles excitation wavelength of 290 nm as shown in Figure 6-8. The concentration of PPO and POPOP used for this study is 1 wt% and 0.05 wt% respectively. The photoluminescence of 20 wt % and 30 wt% HVDAC coated $La_{0.6}Ce_{0.4}F_3$

nanoparticles measured at 290 nm excitation shows enhanced photoluminescence compared to nanoparticles free PPO/POPOP/PS monolith.

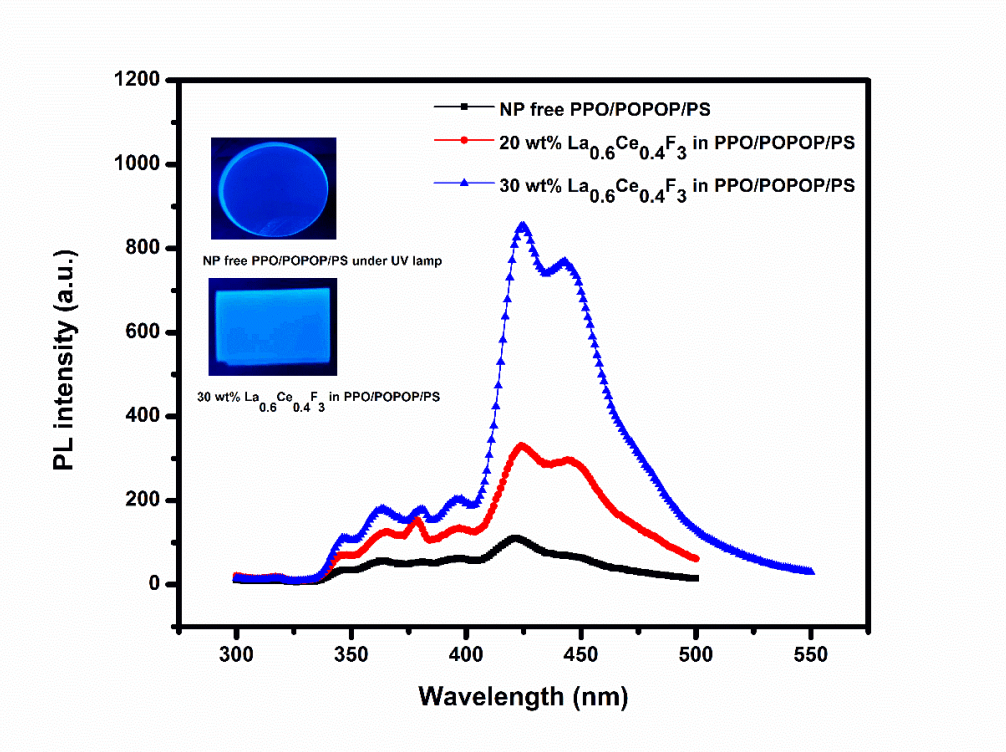

Figure 6-8 Photoluminescence emission of nanoparticles free and different concentration La0.6Ce0.4F3 nanoparticles loaded nanocomposites excited at 280 nm. Inset shows the image of nanoparticles free and 30 wt% La0.6Ce0.4F3 loaded nanocomposite under UV lamp.

This enhancement is due to the increase in energy transfer from the bulk part to the combination PPO and POPOP dye as a result of high density and high Z value. This increase density and Z-value of nanocomposite scintillator results in a higher conversion of gamma-ray photons to energetic primary electron and eventually enhance the photoluminescence through efficient energy transfer process. The enhancement is about 3 times in the 20 wt% nanoparticles loaded sample and more than 7 times in case of the

30 wt% nanoparticles loaded nanocomposite. We also compared the photoluminescence of 30 wt% $La_{0.6}Ce_{0.4}F_3$ nanoparticles loaded nanocomposite and EJ-200 commercial plastic scintillator from Eljen technology as shown in Figure 6-9. The photoluminescence peak intensity obtained from the nanocomposite is about 2.5 times stronger compared to EJ-200 plastic scintillator. This shows that the as fabricated nanocomposite do not luminescence quenching due to loading of high density $La_{0.6}Ce_{0.4}F_3$ nanoparticles as observed in some composite scintillators reported in the past. This is due to the efficient FRET energy transfer between the luminescent $La_{0.6}Ce_{0.4}F_3$ nanoparticles and scintillation dye as a result of spectral overlapping of nanoparticles and scintillating dye.

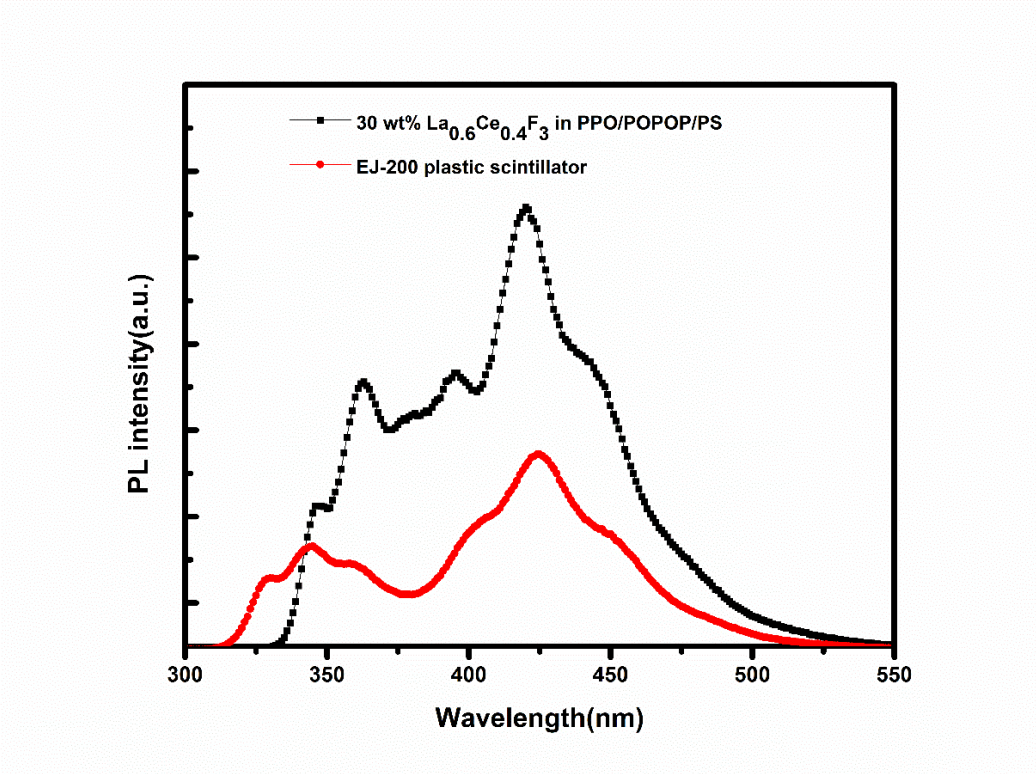

Figure 6-9 Comparison of photoluminescence of 30 wt% La0.6Ce0.4F3 nanoparticles loaded PPO/POPOP/PS and EJ-200 commercial plastic scintillator excited at 280 nm.

To further study the prospect of using nanocomposite scintillator for gamma-ray spectroscopy, we have performed scintillation studies with two different energy sources. For this study, we have use relatively low energy Co-57 (122 keV) and high energy Cs-137 (662 keV) as gamma sources and scintillators of dimension (Ø 20 mm X 5 mm). Figure 6.10 shows the pulse height spectra obtained with 0.5 µs shaping time and acquisition time of 300 seconds. Pulse height spectra of nanoparticles free (NP free PPO/POPOP/PS) and 30 wt% $La_{0.6}Ce_{0.4}F_3$ nanoparticles loaded PPO/POPOP/PS samples under 122 keV gamma excitation source (Co-57). The Photopeak (122 keV) can be clearly seen with 30 wt% nanoparticles loaded PPO/POPOP/PS monolith whereas nanoparticles free sample show no sign of photopeak.

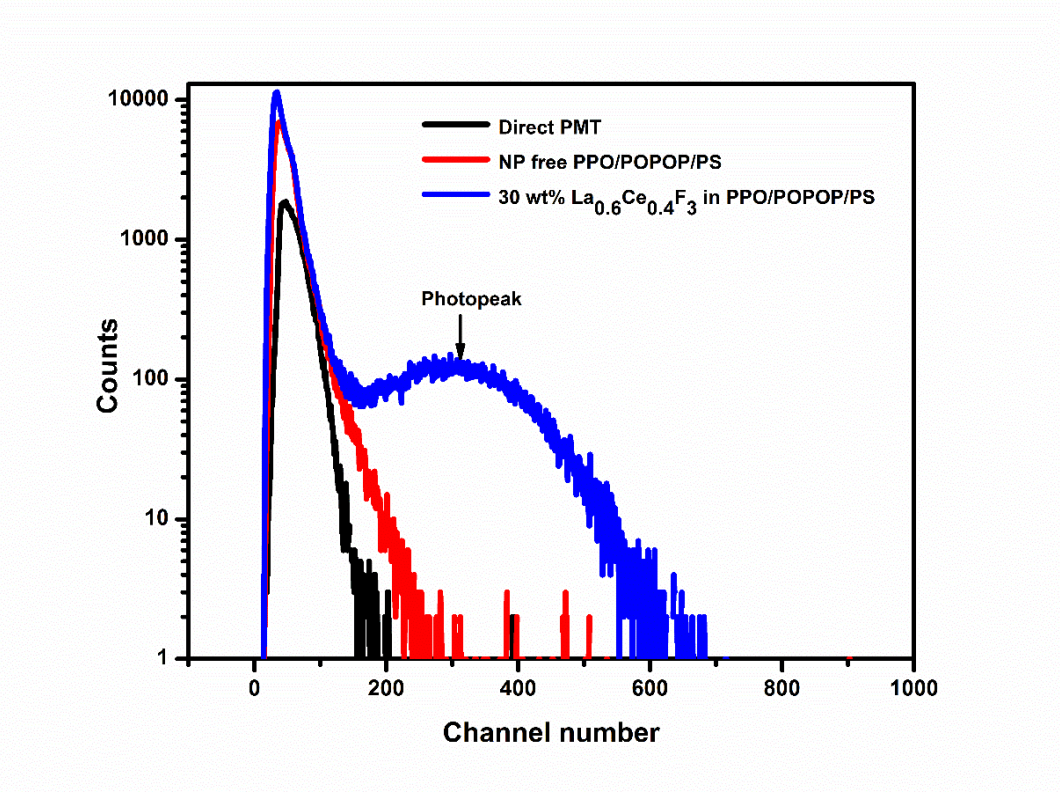

Figure 6-10 Pulse height spectra of nanoparticles free and 30 wt% La0.6Ce0.4F3 nanoparticles loaded PPO/POPOP/PS, for a Co-57 (122 keV) gamma source.

This appearance of photopeak with nanocomposite scintillator is due to the increase density and Z_{eff} value of nanocomposite as well as the effective FRET energy transfer from base to the fluor.

To provide further evidence of photopeak generation with nanocomposite scintillator, we have measured the pulse height spectra of nanoparticles free and 30 wt% nanoparticles loaded sample and compare with commercial plastic scintillator (EJ-200) using 662 keV (Cs-137) gamma ray source. Pulse height spectra of both the nanoparticles free PPO/POPOP/PS monolith and EJ-200 plastic scintillator did not show any sign of photopeak as shown in Figure 6-11.

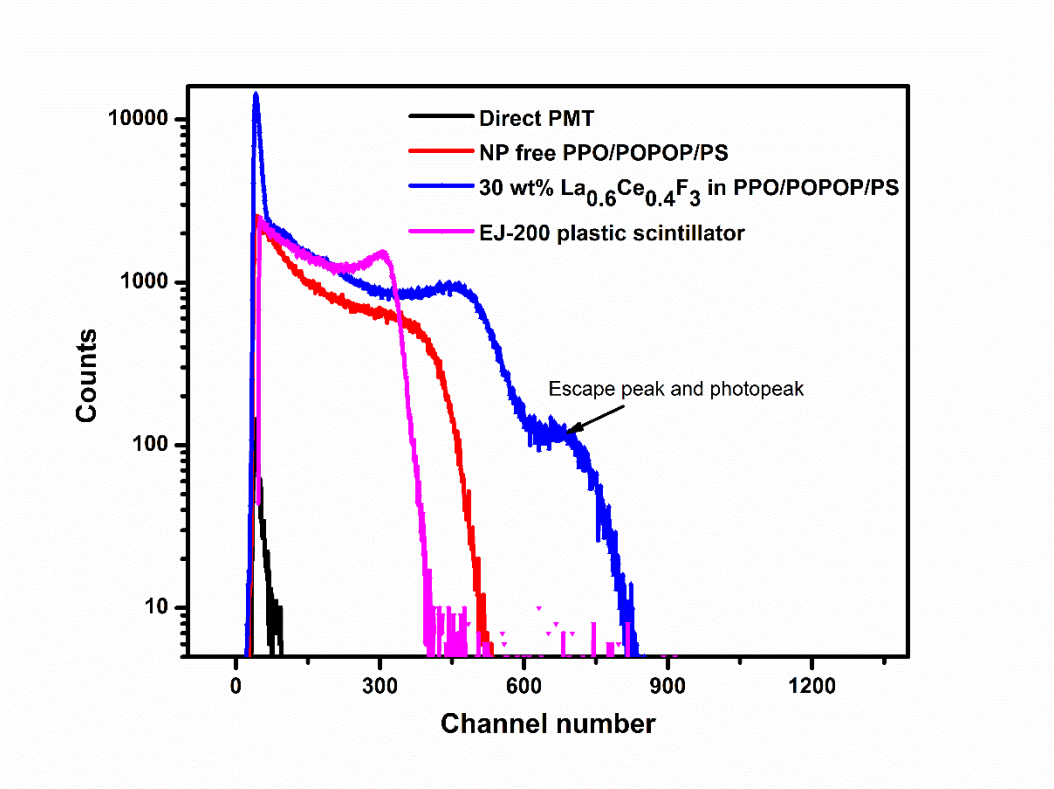

Figure 6-11 Pulse height spectra of nanoparticles free and 30 wt% La0.6Ce0.4F3 nanoparticles loaded PPO/POPOP/PS for a Cs-137 (662 keV) gamma source.

However, pulse height spectra of 30 wt% nanoparticles loaded PPO/POPOP/PS monolith exhibits a shoulder peak. To further clear the appearance of shoulder peak in the pulse height spectra of nanocomposite, we have obtained pulse height spectrum of nanoparticle free sample and 30 wt% $La_{0.6}Ce_{0.4}F_3$ nanoparticles with longer acquisition time of 20 min. The pulse height spectrum of nanoparticles free sample as shown in Figure 6-12 shows the Compton edge at 478 keV. The position of Compton edge is solely depends on the energy of incoming gamma ray. It has been reported that for a 662 keV gamma ray, the Compton edge corresponds to a deposited energy of 478 keV.[48]

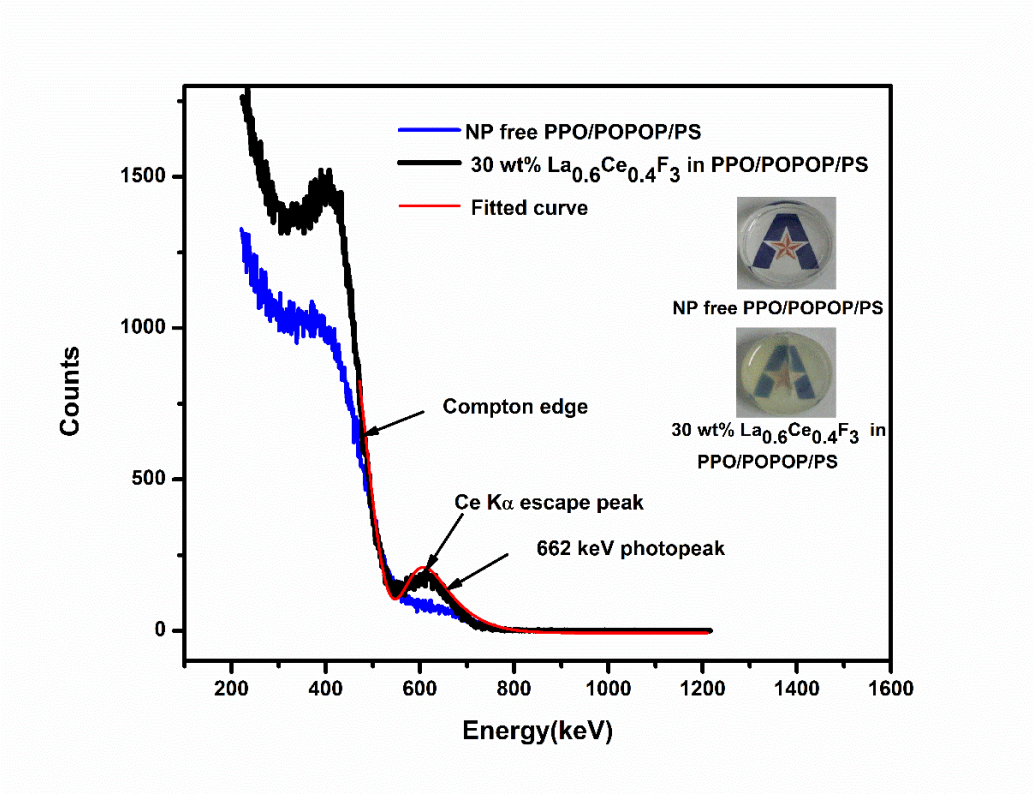

Figure 6-12 Cs-137 (662 keV) gamma-ray spectrum of nanoparticles free and 30 wt% La0.6Ce0.4F3 nanoparticles loaded PPO/POPOP/PS. Inset shows the image of nanoparticles free and 30 wt% La0.6Ce0.4F3 loaded nanocomposite of dimension (Ø 20 mm X 5 mm).

The pulse height spectrum of nanocomposite shows the Compton edge at 478 keV and full energy peak with peak at 622 keV. This peak is in agreement with the escape peak of La and Ce Kα X-rays (622 - 34 = 628 keV). An escape peak usually dominant in the small size scintillators as a result of high-Z Kα X-rays escaping from the scintillator and should disappear for the large size scintillator due to the recapture of La and Ce Kα X-rays. It is likely that 662 keV photopeak will be well resolved with the large test sample, sufficient enough to stop the high energy 662 keV photons or to recapture the escaping X-rays. In addition, the further improvement in the transparency of the nanocomposite scintillator would improve the scintillation efficiency by reducing the photons loss due to the light scattering at higher nanoparticles loading.

Figure 6-13 shows the scintillation decay time of the nanocomposite, measured at 662 keV excitation. Scintillation decay time was obtained by exponential fitting of the experimental data. The scintillation decay time of 11.5 and 13.2 ns are obtained for the nanoparticles free PPO/POPOP/PS and 30 wt% La0.6Ce0.4F3 nanoparticles loaded PPO/POPOP/PS nanocomposites. The decay time measurement shows no significant change in scintillation decay time due to the nanoparticles loading resulting in a nanocomposite scintillator with fast decay time.

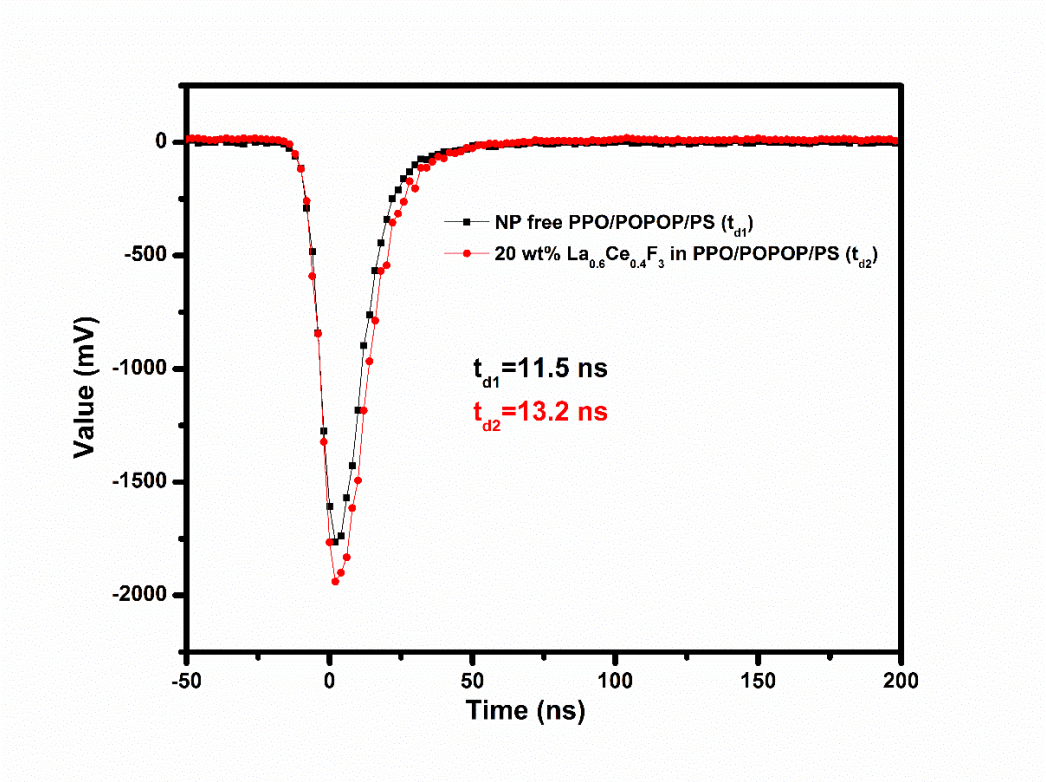

Figure 6-13 Scintillation decay time of nanoparticles free and 30 wt% La0.6Ce0.4F3 nanoparticles loaded PPO/POPOP/PS using Cs-137 (662 keV) gamma excitation source.

6.4 Summary

This work explains a new synthesis approach of highly dispersible $La_{0.6}Ce_{0.4}F_3$ nanoparticles using polymerizable surfactant HVDAC as a surface coating agent. HVDAC coated $La_{0.6}Ce_{0.4}F_3$ nanoparticles were synthesized using a simple one step wet chemistry method. As-synthesized nanoparticles are highly dispersible in styrene due to the presence of the long hydrocarbon chain of HVDAC. Transparent nanocomposite scintillators were fabricated by copolymerization of HVDAC coated $La_{0.6}Ce_{0.4}F_3$ nanoparticles with styrene using free radical bulk polymerization. Nanoparticles loading as high as 30 wt% were

achieved. Nanocomposite scintillator exhibits enhanced photoluminescence and relatively high gamma stopping power. Pulse height spectra show that these nanocomposites exhibit a clear photopeak. The pulse height spectrum clearly shows the low energy 122 keV (Co-57) photopeak. This is due to the higher stopping power and, in part, due to the effective FRET energy transfer from base to fluor in nanocomposite scintillator as a result of high nanoparticles loading. The gamma spectrum of Cs-137 (662 keV) obtained with nanocomposite scintillator exhibits a full energy spectrum with peak at 622 keV. This peak is associated with the escape of La and Ce Kα X-rays is due to the small size of the tested scintillators. It is expected that the further improvement in transparency at 30 wt% nanoparticles loading and using large size test sample, may resolve the photopeak from the escape peak. The scintillation decay time shows no significant dependence in the nanoparticle loading concentration in the range studied, thus resulting in nanocomposite with fast decay time. Further work is underway to improve the transparency of the PS matrix at high nanoparticles loading concentration and improve the resolution of high energy photopeak.

Chapter 7

Investigation of $La_xY_{2-x}O_3$ Ceramic as a Cost Effective Alternative to Single Crystal Scintillators

7.1 Introduction

For radiation detection, the sensitivity, response time, and energy resolution are important. To perform optimally, a scintillator must have high luminescence quantum efficiency, fast decay time, high stopping power and high carrier mobility-lifetime products.[128] Gamma radiation detectors have traditionally been made with inorganic scintillators, single-crystal materials that generate visible or ultraviolet (UV) light when traversed by gamma ray photons. Such materials must be highly transparent to the wavelengths generated. Examples of scintillator crystals in current use are CsI, NaI, BaF_2, bismuth germanate (BGO),[129, 130] and the recently developed such as $LaBr_3$:Ce.[131, 132] Even though these crystals generally work well for radiation detection, they have some limitations. For example, the low detection sensitivities and energy resolutions of most crystals cannot fulfill today's requirements for low dose radiation detection. Some scintillator crystals, such as NaI, are hygroscopic, which is a critical issue for practical applications. In addition, it is very difficult to grow large, high quality crystals; consequently most scintillation crystals are very expensive.

Organic scintillators such as polyvinyl toluene (PVT)/2,5-Diphenyloxazole (PPO) have been used for radiation portal monitors.[133, 134] The advantages of organic scintillators are that they are low cost, can be produced in large quantities, and have high sensitivity.[133, 134],[135] However, they also have several disadvantages including poor energy resolution and susceptibility to radiation damage. Moreover, they are not as stable as inorganic scintillators, and have less sensitivity to high energy radiation.[133, 134]

Another possible option for radiation detection is scintillating nanoparticles, which have been shown to possess three times higher luminescent efficiency[136] and two times better energy resolution[137] than bulk crystal scintillators.

Recently, polycrystalline transparent ceramic has emerges as an alternative to single crystals[138],[139]. Transparent ceramics are fully dense monoliths of micron-scale crystallites, formed by sintering ceramic nanopowders, generally of a single pure phase cubic crystal structure[140]. Compared to single crystal these can grow in large volumes, easy fabrication, low cost, mass production and can be easily doped with various ions for specifics applications[141]. La_xY_2-xO3, $0<x\leq1$ is an interesting host material for high power solid state laser due to its high thermal conductivity, broad transparency range, good chemical stability and relatively low phonon energy[142],[143]. However, the high melting point of Y_2O_3 (2430 °C) makes it difficult to fabricate a high quality single crystal[144]. Transparent $La_xY_{2-x}O_3$ ceramic can be fabricated at relatively low sintering temperature. Here, for the first time, we report $La_{0.2}Y_{1.8}O_3$ transparent ceramic as a new scintillator for radiation detection. It has comparable energy resolution to NaI(Tl) single crystal scintillator.

7.2 Experimental

7.2.1 Fabrication of $La_{0.2}Y_{1.8}O_3$ Ceramic

$La_{0.2}Y_{1.8}O_3$ ceramic samples were prepared using the same method as reported for $La_{0.1}Nd_{0.1}Y_{1.8}O_3$ and Y_2O_3 transparent ceramics.[145, 146] 0.5 mol/l rare earth nitrate solution was prepared according to $La_{0.2}Y_{1.8}O_3$ stoichiometric ratio using Y_2O_3 and $La(NO_3)_3$.6H2O. At the same time, 0.5 mol/l citric acid solution was prepared according to a certain molar ratio to rare earth nitrate solution. The rare earth nitrate solution was put into a large beaker and stirred for 10 min, and then the citric acid solution was also put into the large beaker and stirred for 30 min. Lastly, 2 wt.% polyethylene glycol was added as

the dispersant and stirred for 30 min. The mixed solution was dried at 90 °C electric blast oven until it became purple red gel, and then the precursor was obtained. The gel was heated up to certain temperature in an electric furnace and self-combustion would occur, resulting in the formation of black and white powders. Then the powder was calcined at different temperatures in chamber furnace for 2 h, after cooling, grinding with agate mortar, the nanopowder of $La_{0.2}Y_{1.8}O_3$ was obtained. The nanopowder was suppressed into green compact of 16×1 mm, and then sintered in a vacuum furnace with 1×10^{-3} Pa and 1600 °C for 6 h. In the last, the $La_{0.2}Y_{1.8}O_3$ transparent ceramic was obtained.

7.2.2 Characterization

$La_{0.2}Y_{1.8}O_3$ transparent ceramic was examined by X-ray diffraction (XRD) with Cu Kα radiation to know the phase structure. Transmission electron microscope (TEM) image of nanoparticles was obtained by JEOL 1200EX STEM. Optical absorption measurement was recorded with Shimadzu UV-2450 spectrophotometer. Photoluminescence (PL) and PL excitation (PLE) spectra were taken on a Shimadzu RF-5301 PC Spectrofluorometer. X-ray luminescence was measured in a light-proof X-ray cabinet equipped with optic fiber connection to an outside detector. X-ray irradiation (60 kV and 5 mA) was performed using a Faxitron RX-650 X-ray cabinet (Faxitron X-Ray Corp, IL, USA). The luminescence spectra were recorded using a QE65000 spectrometer (Ocean Optics Inc, Dunedin, FL), connected to the X-ray chamber using a 600 μm core diameter, P600-2-UV-Vis fiber optic (Ocean Optics Inc, Dunedin, FL). Gamma spectra were acquired with various radioactive sources, with scintillators coupled to a Hamamatsu PMT, ORTEC 113 preamplifier and ORTEC 575A amplifier and recorded with an ORTEC 926 ADCAM MCB multichannel analyzer.

7.3 Result and Discussion

The $La_{0.2}Y_{1.8}O_3$ transparent scintillator was fabricated by sintering $La_{0.2}Y_{1.8}O_3$ nanoparticles powders at high temperature in vacuum. The size of the $La_{0.2}Y_{1.8}O_3$ ceramic used for this study was Ø 10 X 1 mm^2. Figure 7-1 shows the XRD pattern of $La_{0.2}Y_{1.8}O_3$ transparent ceramic and commercial Y_2O_3 particles.

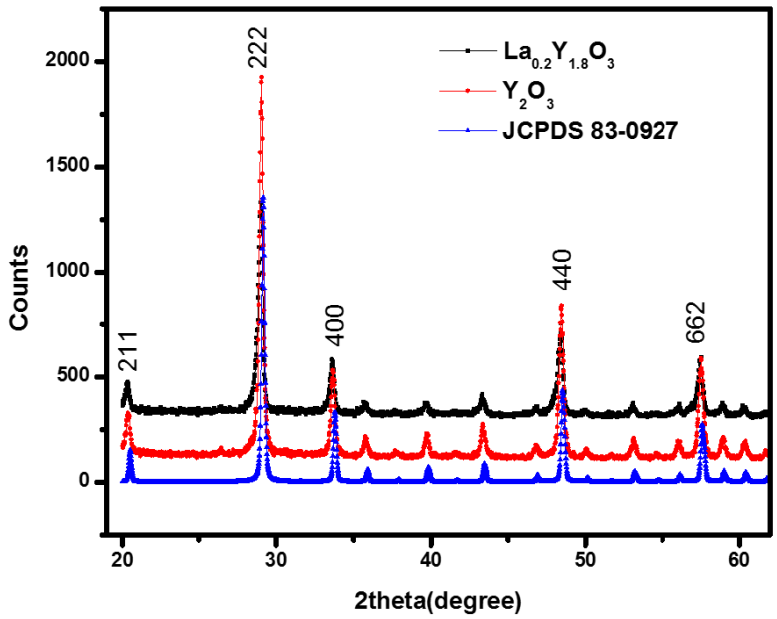

Figure 7-1 XRD pattern of La0.2Y1.8O3 ceramic, Y2O3 powder and JCPDS reference file.

All the peaks are assigned to the cubic phase of Y_2O_3 which means La^{3+} ions is completely dissolved in Y_2O_3, when sintered at temperature higher than 1100°C. A left-shift in the diffraction peak can be observed in $La_{0.2}Y_{1.8}O_3$. This is due to the larger ionic radius of La^{3+} (117.2 pm) compared to that of Y^{3+} (104 pm). Figure 7-2(A) shows the TEM image of $La_{0.2}Y_{1.8}O_3$ nanoparticles before the fabrication of transparent ceramic and the average size of the particles is about 28 nm. Scanning electron microscope (SEM) microstructure

of $La_{0.2}Y_{1.8}O_3$ transparent ceramic is shown in Figure 7-2(B) with an average grain size of about 200 μm.

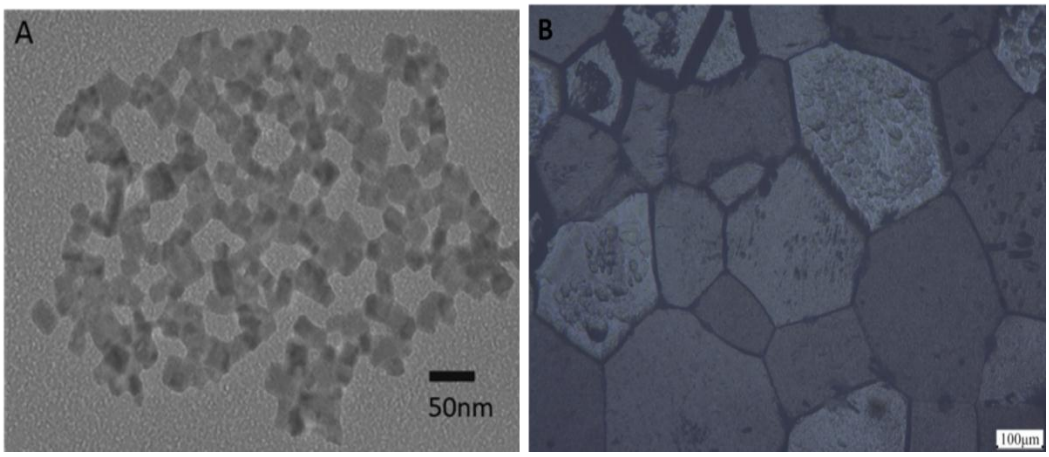

Figure 7-2 TEM image of La0.2Y1.8O3 nanoparticles (A), SEM micrograph of La0.2Y1.8O3 transparent ceramic (B).

Figure 7-3 shows the photoluminescence emission and excitation spectrum of $La_{0.2}Y_{1.8}O_3$ ceramic. The main peak of the PL emission is at 430 nm with a bump at 375 nm. The emission at about 375 nm has been observed in Y_2O_3 and reported by several authors.[147-151] Based on the ODMR study which showed the existence of a triplet state of trapped excitons, Hayes et al. reported that the 360 nm emission in Y_2O_3 is due the recombination of self-trapped excitons (STE).[147] Lushchik et al. reported that the self-trapped excitons emission in Y_2O_3 is similar to that observed in Al_2O_3 but different from STE emission in alkali halides. In Y_2O_3 electrons and holes do not separately undergo transformation separately into a stable self-trapped state while self-shrunk excitons are formed and the intrinsic emission is due to the radiative decay of self-shrunk excitons.[149,

152]. The emission at 430 nm is likely due to the self-trapped emission which is the most common cause of luminescence in wide band gap oxides.

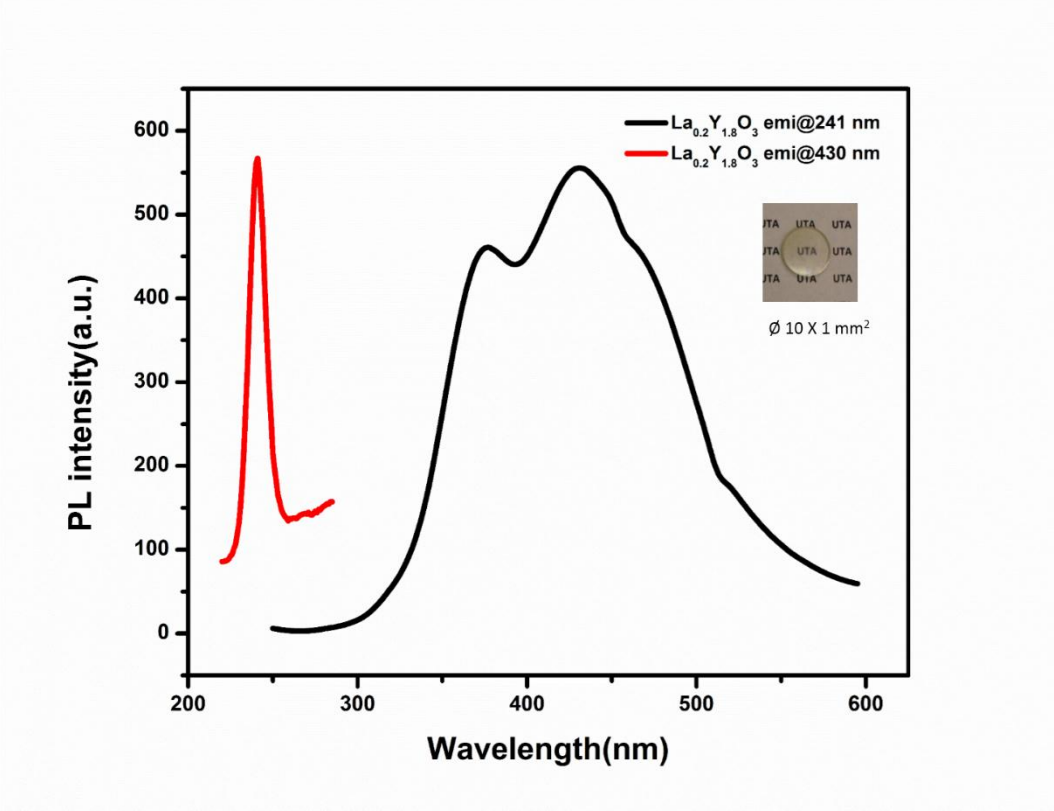

Figure 7-3 Photoluminescence emission and excitation of La0.2Y1.8O3 ceramic.

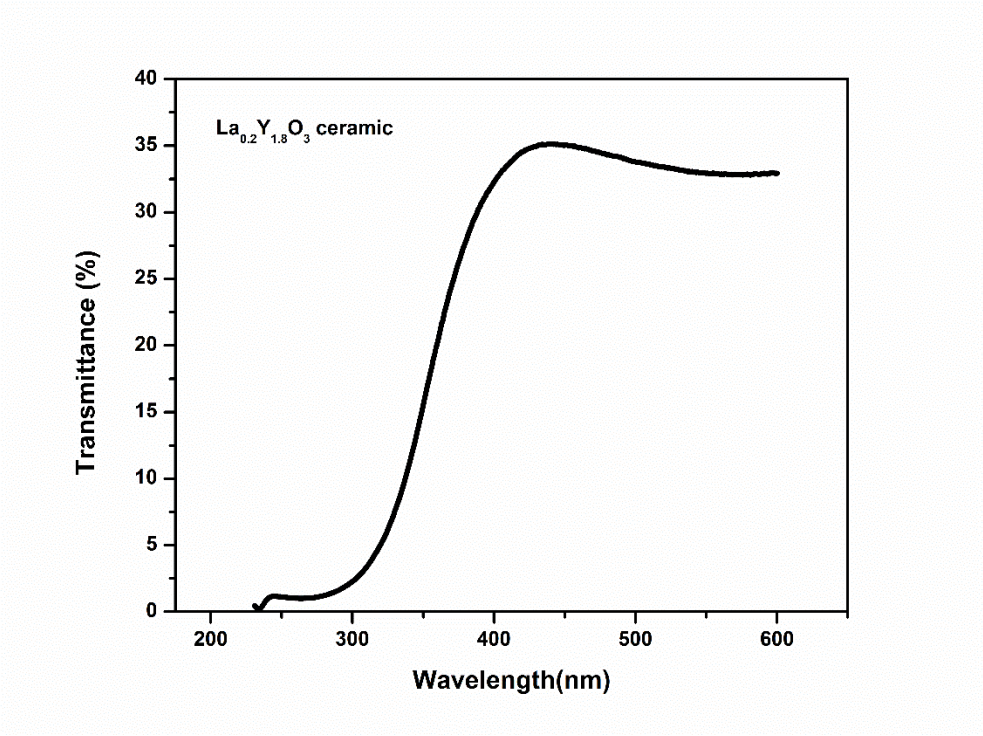

Figure 7-4 Optical transmittance of La0.2Y¬1.8O3 ceramic of thickness 1 mm.

The transparent ceramic of $La_{0.2}Y_{1.8}O_3$ shows light transmittance up to 35% in the region of it emission as shown in Figure 7-4. To compare the scintillation properties of $La_{0.2}Y_{1.8}O_3$ ceramic, we have measured the X-ray excited luminescence of $La_{0.2}Y_{1.8}O_3$ ceramic and compared with EJ-200 commercial plastic scintillator from Eljen Technology. Our measurements show that the XL of $La_{0.2}Y_{1.8}O_3$ ceramic is more than 20 times stronger in intensity than that of EJ-200 of about the same dimension as shown in Figure 7-5. This indicates that $La_{0.2}Y_{1.8}O_3$ is a good scintillator for radiation detection.

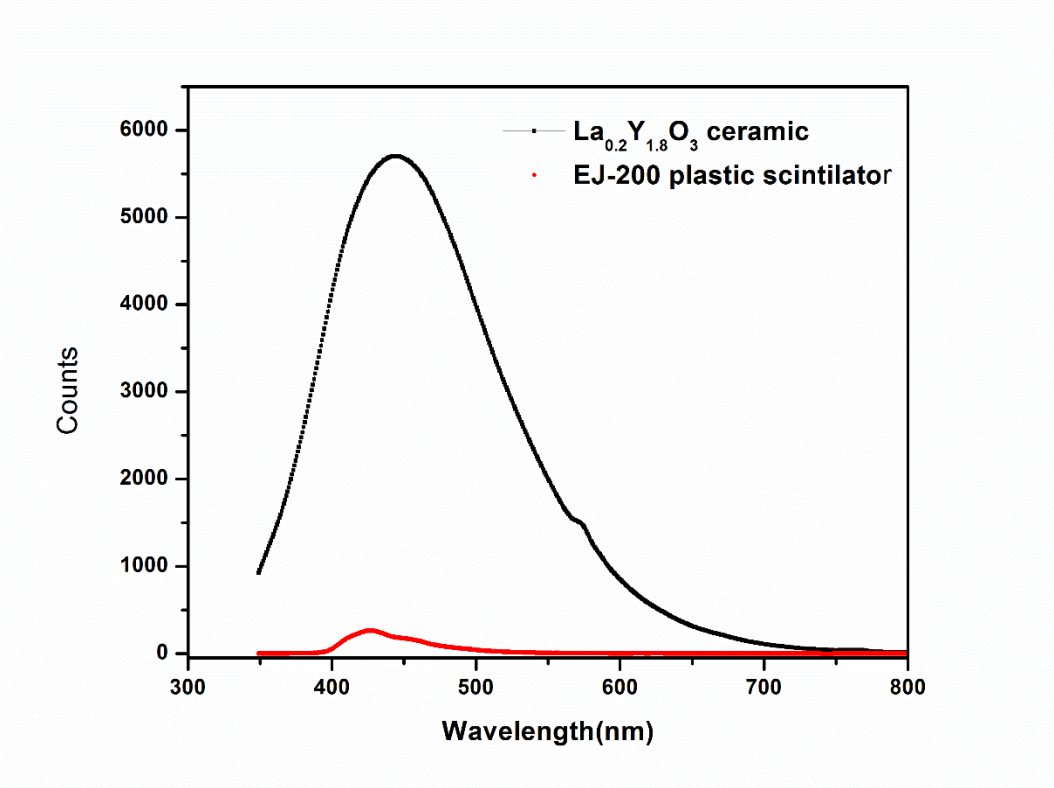

Figure 7-5 X-ray excited optical luminescence of La0.2Y¬1.8O3 ceramic and EJ-200 plastic scintillator.

To prove that, $La_{0.2}Y_{1.8}O_3$ was tested for radiation detection with different gamma sources. The radiation testing results show that $La_{0.2}Y_{1.8}O_3$ has excellent scintillation properties under gamma excitation. Figure 7-6 shows the pulse height spectra of Na-22 gamma source. The pulse height spectrum clearly shows the 511 keV. A small bump at high energy (1275 KeV) is seen in $La_{0.2}Y_{1.8}O_3$ scintillator compared to a peak from NaI. This signal is weak and this is likely due to the small size of the $La_{0.2}Y_{1.8}O_3$ scintillator that affects the detection efficiency. As the volume of $La_{0.2}Y_{1.8}O_3$ (0.07 cm3) is much smaller than the CsI (1 cm3) and NaI (16.4 cm3) scintillators, its detection efficiency is lower

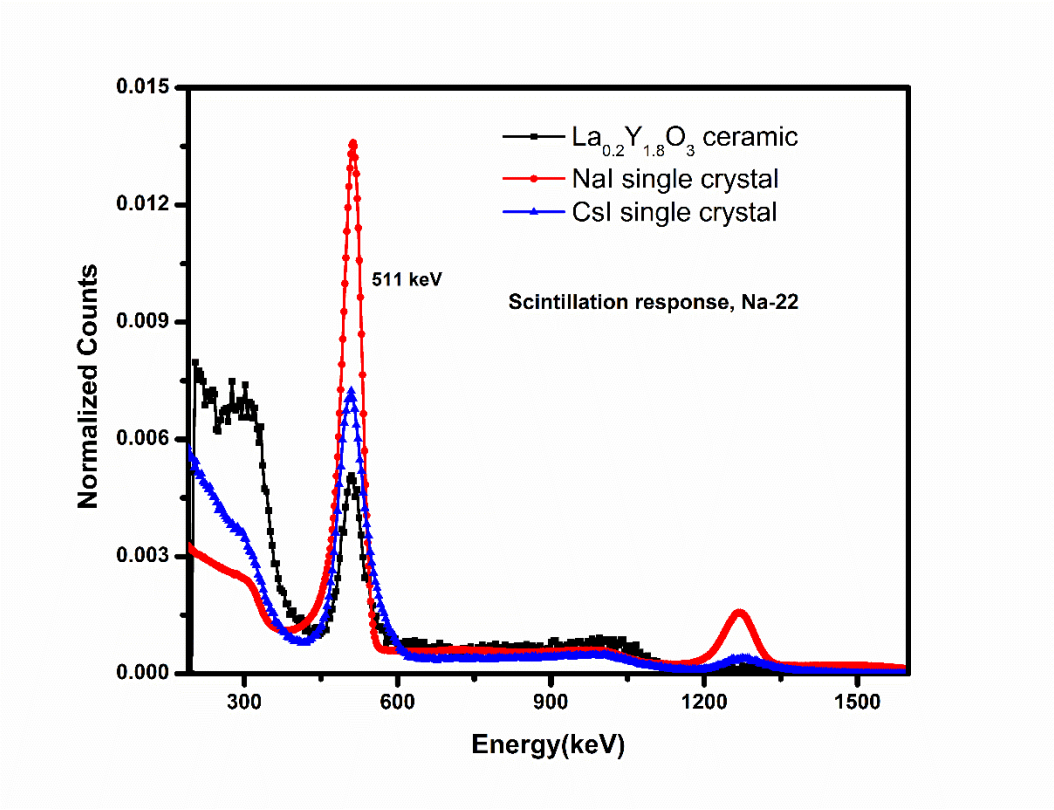

Figure 7-6 Pulse height spectra of Na-22 gamma source obtained with La0.2Y1.8O3 ceramic, NaI and CsI single cyrstals.

Pulse height spectra of Cs-137 gamma source are shown in Figure 7-7. Again 662 keV photopeak is clearly pronounced in the pulse height spectra. The energy resolution of the $La_{0.2}Y_{1.8}O_3$ scintillator at 662 keV is compared with NaI and CsI single crystals. Due to the small size, $La_{0.2}Y_{1.8}O_3$ shows a lower detector efficiency but its energy resolution is comparable to that of CsI and NaI scintillators. All these indicated that $La_{0.2}Y_{1.8}O_3$ is a good scintillator with a good potential for radiation detection and dosimetry.

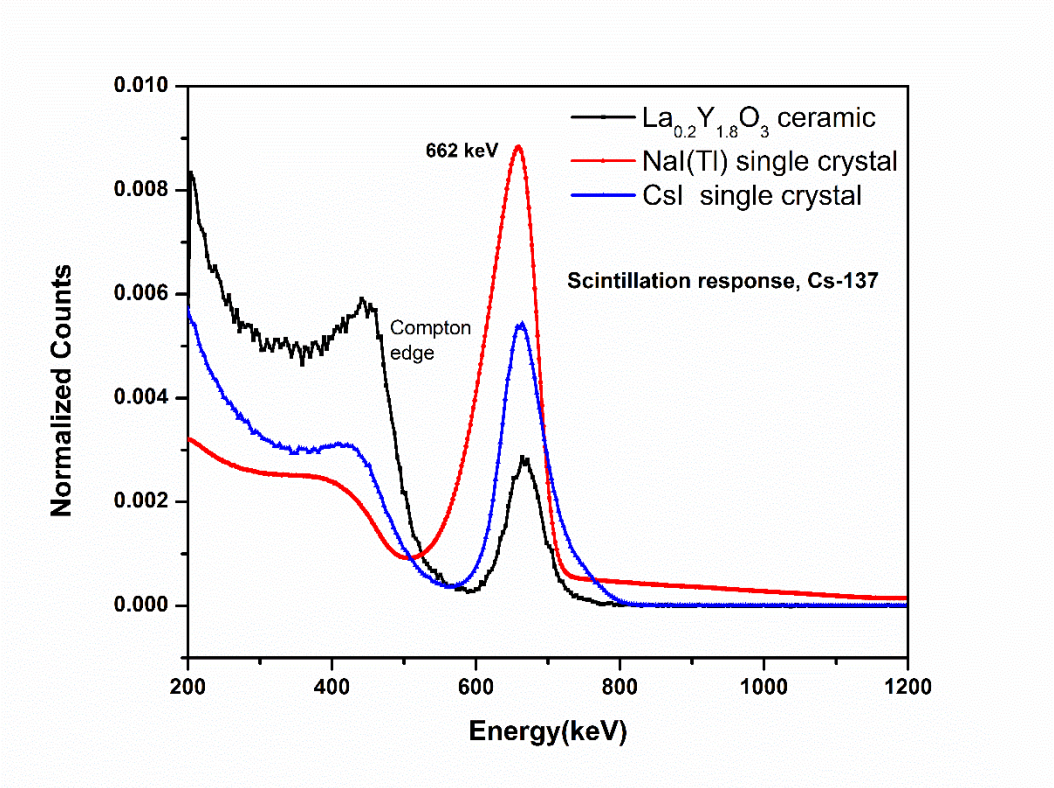

Figure 7-7 Pulse height spectra of Cs-137 gamma source obtained with La0.2Y1.8O3 ceramic, NaI and CsI single cyrstals.

The uncovering of the scintillation luminescence in $La_{0.2}Y_{1.8}O_3$ would be very helpful for the design and development of the new scintillator for practical applications. As it was pointed out that $La_xY_{2-x}O_3$, Y_2O_3 and La_2O_3 are host materials for doped luminescence materials, but not as luminescence materials or scintillators themselves and no luminescence can be observed from La^{3+} or Y^{3+} ions because it is well-known that La^{3+}, Y^{3+}, Lu^{3+} and Sc^{3+} ions have no 4f electrons, therefore no electronic energy levels that can induce excitation and luminescence processes. The luminescence may be from some defects or the so called intrinsic luminescence in wide-gap materials. The intrinsic luminescence is from self-trapped excitons (STEs) which have been detected and well-

studied in some wide-gap materials such as alkali halides, alkali-earth fluorides and oxides.[153] Luminescence of STEs is characterized for its large Stokes-shift and a large emission band-width due to a strong electron-phonon coupling.[154, 155]

From emission and excitation spectra shown in Figure 7-3, we can see that the Stokes shift of the emission is about 190 nm (2.2 eV) and the emission band-width is about 150 nm (0.8 eV). Also, a well-resolved excitonic peak in the excitation spectrum is detected just at the edge of the optical absorption spectrum. All these characteristics indicate that the emission is from STEs in $La_{0.2}Y_{1.8}O_3$.

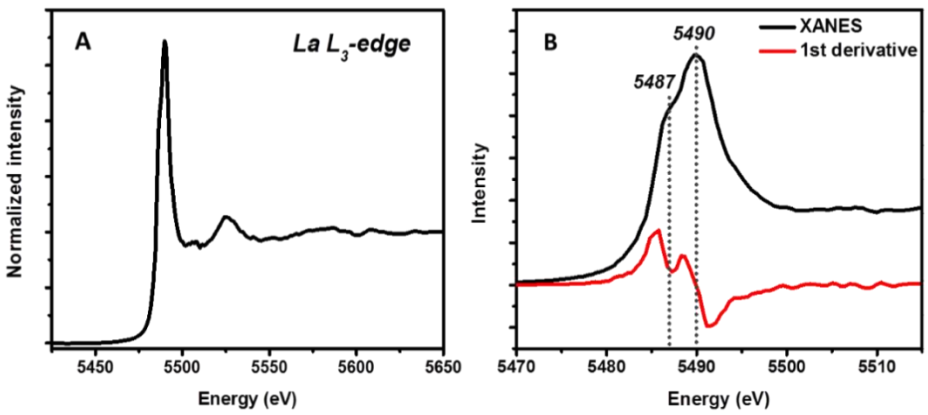

Figure 7-8 (A) Time ungated and time gated XEOL of La0.2Y1.8O3 ceramic, excited with 5800 eV X-ray energy and (B) Fitted curve for fast window.

To further understand the effect of La^{3+} doping on the luminescence and scintillation properties of Y_2O_3, we have performed XANES, time ungated and time gated XEOL as well as TRXEOL of $La_{0.2}Y_{1.8}O_3$ transparent ceramic. We have used elemental

selective XANES to excite the $La_{0.2}Y_{1.8}O_3$ transparent ceramic with excitation energy below, above and at the La L3-edge. La L3-edge XANES spectrum of $La_{0.2}Y_{1.8}O_3$ transparent ceramic is shown in Figure 7-8(A). The main characteristic of the La L3-edge XANES spectrum is a white line at around 5490 eV assigned to electric transition from $2P_{3/2}$ to 5d. The first derivative of La L3-edge XANES shown in Figure 7-8(B) reflects the splitting of 5d orbital, which is due to the local distortion of the crystal field.

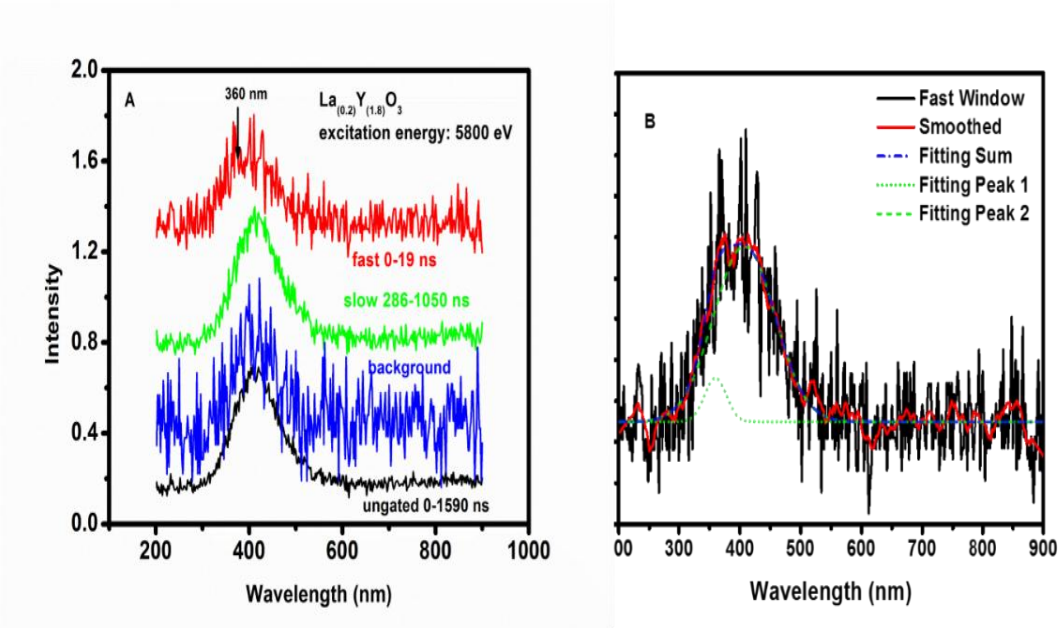

Figure 7-9 (A) Time ungated and time gated XEOL of La0.2Y1.8O3 ceramic, excited with 5800 eV X-ray energy and (B) Fitted curve for fast window.

Time ungated and time gated (fast and slow time windows) XEOL spectra when excited above the La L_3 absorption edge (5800 eV) is shown in Figure 7-9(A). Relative lifetime of multiple peaks can be determined by applying different time gates.[156] Time gates of 0-19 ns and 280-1050 ns were chosen for fast and slow time windows respectively

and 0-1590 ns for ungated window. XEOL spectra obtained from the ungated window (black curve) and slow time window (green curve) are both characterized by a broad emission band with peak center at around 415 nm. In the fast time window, weak emission at around 415 nm can be still seen due to very long decay time. Interestingly, a weak emission also appears at 360 nm in the fast window, which was not observed in the slow window as shown in Figure 7-10.

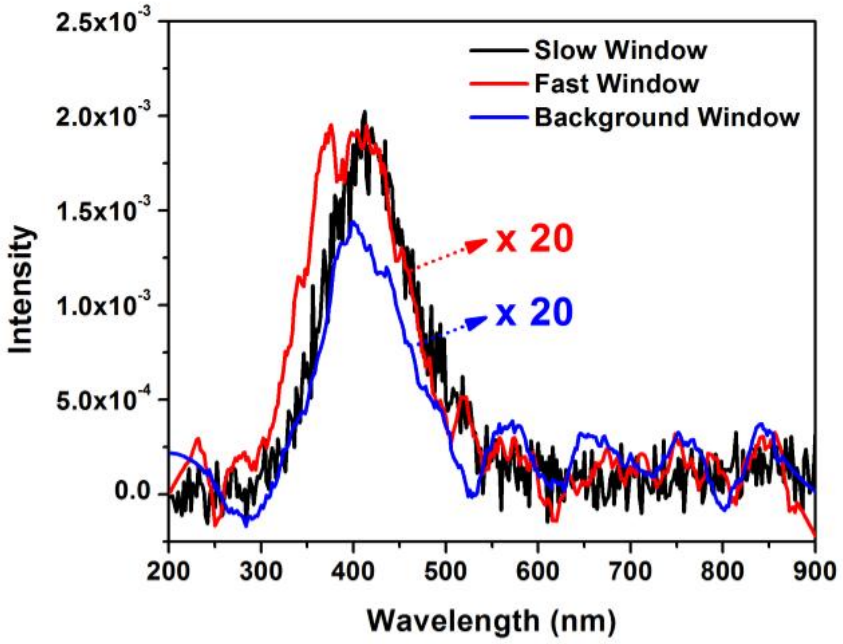

Figure 7-10 Comparison of the XEOL spectra (Eex = 5800 eV) obtained from slow (black curve), fast (red curve, smoothed) and background (blue curve, smoothed) windows. The intensities of the spectrum from slow and fast window are increased by 20 times.

The fitted XEOL curve from the fast window is shown in Figure 7-9(B). The spectrum from the fast window is well fitted using two peaks at 360 and 410 nm via multiple

Gaussian fitting. To make it further clear we have measured the TRXEOL of different emission curve. Decay curve of 360 nm and 415 nm emission (excited at 5800 eV) is shown in Figure 7-11(A). It shows that the 360 nm emission decays relatively faster than the broad emission at 415 nm. Decay times are approximated by using two exponential fitting of the decay curve. The decay time for 360 nm peak shows a faster component of 25 ns and a slower component of 255 ns whereas the dominant decay time of 364 ns is observed for 415 nm peak along with a fast component of about 55 ns.

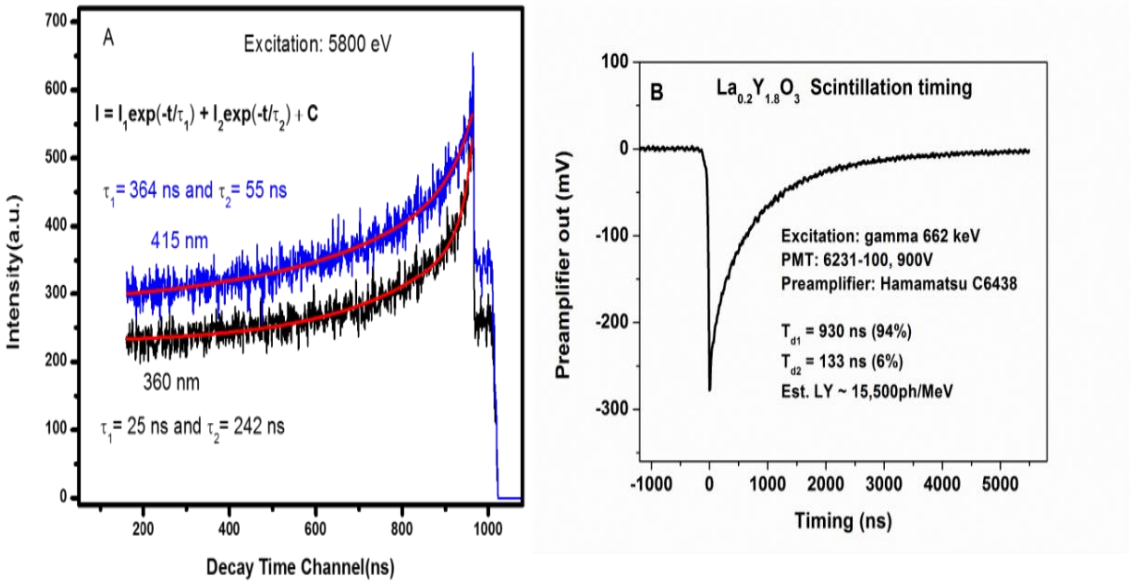

Figure 7-11 (A) Decay curve of 360 and 415 nm emission. The solid red line is the result of bi-exponential curve fitting and (B) Scintillation timing of La0.2Y1.8O3 ceramic excited with gamma 662 keV.

We have also measured the scintillation decay time where the sample is excited with 662 keV gamma source. Our results shows the decay consisting of a relatively fast component of 133 ns and a slower one of about 930 ns. The main decay component is the slower one with 94% of the emission decaying through this channel and 6% of emission through fast component as shown in Figure 7-11 (B). This is further supported by the time gated (fast and slow) XEOL measured below the La L_3-edge and at the white line as shown in Figure 7-12 (A) and (B) respectively. When the sample is excited both below the La L_3-edge and at the white line, a strong emission is observed at ungated and slow gated windows whereas a weak emission at the fast window.

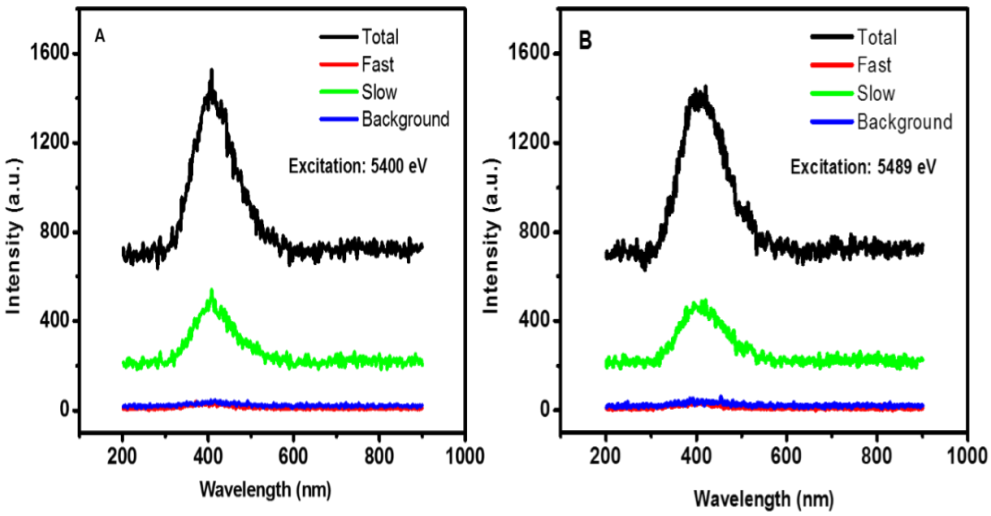

Figure 7-12 Time ungated and time-gated (fast and slow window) XEOL intensity (A) below the La L3-edge (5400 eV) and (B) at the white line (5489 eV).

At the La whiteline, La absorbs preferentially compared to absorption below the edge; since La is a minor component and the dominant energy transfer is to the slow optical channel, the TRXEOL should be similar as observed; that is that the ungated and the slow

window gated XEOL are similar and dominant. This suggest that the weak emission at 360 nm at the fast window in $La_{0.2}Y_{1.8}O_3$ under 5800 eV excitation is associated with the Y_2O_3 host matrix. The dominant slower emission at 415 nm has not been reported in Y_2O_3 and therefore is associated with the La^{3+} doping in Y_2O_3. As, no luminescence can be observed from La^{3+} or Y^{3+} ions because La^{3+}, Y^{3+}, Lu^{3+} and Sc^{3+} ions have no 4f electrons, therefore no electronic energy levels that can induce excitation and the luminescence processes. The first derivative of XANES spectrum in figure 7.8(B) shows the local distortion of crystal field in $La_{0.2}Y_{1.8}O_3$ ceramic. Also the XRD pattern in figure 7.1 shows the left shift of diffraction peaks due to the lattice distortion upon larger La^{3+} doping into smaller Y^{3+} sites and the emission at 415 nm is likely due to the defects induced as a result of lattice distortion during La^{3+} doping into Y^{3+} sites. Luminescence studies showed that the recombination of self-trapped excitons is the most common cause of luminescence in wide band gap oxides.[147, 149, 157, 158] In $La_{0.2}Y_{1.8}O_3$, we believe the lattice defects are created due to La^{3+} doping in Y_2O_3; resulting in trapping of excitons and the emission at 415 nm might be due to the recombination of the trapped excitons in $La_{0.2}Y_{1.8}O_3$.

7.4 Summary

For the first time, $La_{0.2}Y_{1.8}O_3$ is reported as a scintillation material for radiation detection. The transparent $La_{0.2}Y_{1.8}O_3$ sample is made with nanoparticles of about 25 nm. Pulse height spectra clearly show the photopeak with $La_{0.2}Y_{1.8}O_3$ ceramic scintillator. The preliminary observations show that $La_{0.2}Y_{1.8}O_3$ has a comparable energy resolution to NaI scintillators. In addition, $La_{0.2}Y_{1.8}O_3$ has very good chemical stability, low phonon energy and is cost-effective than NaI crystals.

Chapter 8

Conclusions and Future Work

Inorganic single crystals and organic scintillators are two main type of scintillators currently used for radiation detection. Inorganic single crystals have high efficiency and good energy resolution. However, inorganic single crystals are difficult to grow in large size and are expensive. On the other hand, organic scintillators are attractive for large area detection due to its easy of fabrication and low cost. However, low Z-value of organic scintillator; result in poor energy resolution, limiting its application in gamma ray spectroscopy.

Nanocomposite scintillators have been researched as a new scintillator type. Nanocomposite scintillators are fabricated by embedding nano size inorganic crystal into polymer matrix. It is expected that the nanocomposite scintillators will combine the advantages of both inorganic crystals and organic polymers. In principle, nanocomposite scintillator would have an efficiency and energy resolution similar to the embedded inorganic crystals and ease of fabrication and cost effectiveness of organic polymers.

The synthesis of nanocomposite scintillators requires two steps. First, synthesis of nanocrystals and secondly dispersion of nanocrystals into monomer and polymerization to obtain the solid polymer monolith embedded with nanocrystals. The efficiency and energy resolution of nanocomposite scintillator depends on the concentration of nanocrystals embedded in polymer matrix. It is required to embed high concentration of nanocrystals into polymer to produce photopeak at gamma excitation. However, the high concentration of nanocrystals loading results in aggregation of nanocrystals in polymer matrix. Due to nanocrystals aggregation, polymer matrix loses optical transparency, resulting in luminescence quenching.

The main work of this dissertation work is to improve the energy resolution of organic plastic scintillator by embedding nanocrystals into polymer matrix. To achieve this it is absolutely necessary to synthesis nanocrystals with high dispersion into polymer matrix.

We have used $La_xCe_{1-x}F_3$ $0<x\leq1$ as a nano filler with high density. $La_xCe_{1-x}F_3$ nanofiller coated with different organic surfactant to improve the dispersion of $La_xCe_{1-x}F_3$ into polymer matrix. First, polyethylene glycol coated CeF_3 nanoparticles were synthesized with high dispersion in water and water soluble polymer. High concentration of the as synthesized CeF_3 nanoparticles (up to 30 wt%) were embedded into water soluble polymer polyvinyl alcohol (PVA) using solvent casting method. CeF_3-PVA nanocomposites show characteristics CeF_3 emission. However, the polymer nanocomposites were limited by its thickness. CeF_3-PVA nanocomposites were less than 1 mm and too thin to attenuate high energy gamma photons. Also, CeF_3-PVA nanocomposites emits in the region of low detection efficiency of photomultiplier tube (PMT). To overcome this CeF_3/ZnO nanocomposite were synthesized. ZnO was used due to the spectral overlapping of ZnO absorption with emission of CeF_3 nanoparticles. The spectral overlapping enables the fluorescence resonance energy transfer (FRET) from CeF_3 to ZnO nanoparticles, resulting in ZnO emission at CeF_3 excitation. However, the nanocomposite shows low dispersion in polymers showing aggregation of nanoparticles with less than 2 wt% loading concentration.

To improve the dispersion of nanoparticles in to polymers we have used oleic acid as surface coating agent to synthesized CeF_3 nanoparticles. The as synthesized oleic acid coated CeF_3 (OA-CeF_3) nanoparticles show better dispersion in organic polymer such as polyvinyl toluene and polystyrene. Polyvinyl toluene (PVT) was used as a polymer matrix to embed OA-CeF_3 nanoparticles using free radical bulk polymerization. Scintillating dye 2,5-diphenyloxazole (PPO) were used to shift the emission of nanocomposite in the region

of high detection efficiency of PMT. The absorption spectra of PPO overlaps with the emission of OA-CeF_3 nanoparticles resulting in enhance PPO emission in PPO/CeF_3/PVT nanocomposites. Due to the improvement in dispersion of OA-CeF_3 nanoparticles, loading up to 10 wt% were achieved in PVT matrix. However, above 10 wt% nanoparticles loading, PPO/CeF_3/PVT nanocomposites show loss of transparency. Scintillation measurements studies shows, reduced light yield at 10 wt% nanoparticles loading. This is due to the light scattering in nanocomposite due to aggregation of nanoparticles at higher loading. Also, no photopeak was observed in pulse height spectra, which might be due to the lower loading level of nanoparticles into polymer matrix.

To further improve the dispersion of nanoparticles in polymer matrix at higher nanoparticles loading concentration, we have synthesized a polymerizable surfactant hexadecyl-*p*-vinylbenzyldimethylammonium chloride (HVDAC) and used as a surface coating agent for $La_xCe_{1-x}F_3$ nanoparticles. The as synthesized HVDAC coated $La_xCe_{1-x}F_3$ nanoparticles shows high dispersion in styrene. Nanocomposite scintillator were fabricated by embedding HVDAC coated $La_xCe_{1-x}F_3$ nanoparticles with scintillating dye PPO and 1,4-bis(5-phenyloxazol-2-yl) benzene (POPOP). POPOP is commonly used as a wavelength shifter in plastic scintillator to overcome the problem of self-quenching in organic scintillating dye. The as fabricated nanocomposites were optically transparent at nanoparticle loading concentration as high as 30 wt%. Nanocomposites show enhanced photoluminescence and gamma stopping power. Gamma spectroscopy shows nanocomposite with the capability to produce photopeak. Pulse height spectra clearly shows the low energy photopeak. This is due to the enhanced photoelectric effects to produce photoelectron and effective FRET energy transfer from base to fluor in nanocomposite scintillator as a result of nanoparticles loading. Although high energy photopeak is not clearly observed, it is expected that with the further improvement in

transparency at 30 wt% nanoparticles loading and testing with the large size sample, may resolve the photopeak from the escape peak. The scintillation decay time shows no significant difference in decay time due to nanoparticles loading resulting in nanocomposite with fast decay time. Further work is underway to improve the transparency of the PS matrix at high nanoparticles loading concentration and improve the resolution of high energy photopeak.

Finally, a transparent ceramic of $La_{0.2}Y_{1.8}O_3$ has been studied for as a cost effective alternative to single crystal scintillators. Transparent ceramics of $La_{0.2}Y_{1.8}O_3$ were fabricated by vacuum sintering the compact green body of nanoparticles. The photoluminescence spectrum show emission with peak at around 430 nm and large stoke shift of 190 nm for $La_{0.2}Y_{1.8}O_3$ transparent ceramic. The pulse height spectra shows photopeak with $La_{0.2}Y_{1.8}O_3$ transparent ceramic. Moreover, the energy resolution of $La_{0.2}Y_{1.8}O_3$ transparent ceramic at 662 keV is comparable to that of NaI(Tl) single crystal scintillator which is the most common inorganic scintillator currently in use. The scintillation decay time measurements shows the main emission at around 415 nm with intensity of around 94% decay relatively slow and a weak emission at 360nm with intensity of about 6% decay has fast decay time. In addition, transparent ceramic are very stable and easy to fabricate compared to single crystals. This show, transparent ceramic can be used as a cost effective alternative to expensive single crystal scintillators.

For future studies, it is important to embed high concentration of nanocrystals into polymers while maintaining the high light transmission. So, optimization of surface coating with HVDAC is important for maintaining the optical transparency of the matrix. It will be interesting to see how the change in the initial concentration of HVDAC will affects the optical transmittance and light yield of the nanocomposite scintillator. Also, fabrication of

large size nanocomposite scintillators to test the effect of size increment in gamma stopping power to optimized the size to produce the photopeak.

The main scintillation decay of $La_{0.2}Y_{1.8}O_3$ transparent ceramic is the slower component with decay time of 940 ns. Some scintillation application required fast decay time. The decay time as well as efficiency of $La_{0.2}Y_{1.8}O_3$ transparent ceramic can be improved by different co doping. Our preliminary studied on Mg^{2+} co-doping showed enhancement in luminescence of $La_{0.2}Y_{1.8}O_3$ transparent ceramic. It will be interesting to see the effect of co-doping in $La_{0.2}Y_{1.8}O_3$ transparent ceramic.

References

1. Alivisatos, A.P., *Semiconductor clusters, nanocrystals, and quantum dots.* Science, 1996. **271**(5251): p. 933.

2. Blasse, G. and B.C. Grabmaier, *Luminescent materials*. 1994, Berlin; New York: Springer-Verlag.

3. Kitai, A., *Luminescent materials and applications*. 2008, Chichester, England; Hoboken, NJ: John Wiley.

4. Virk, H.S. *Luminescent Materials and their Applications*. 2015; Trans Tech Publisher.

5. Thomas, S. *Recent advances in polymer nanocomposites synthesis and characterisation*. 2010;Tayol and Francis Group, LLC.

6. Mai, Y.W., et al. *Polymer nanocomposites*. 2006; Woodland Publishing.

7. Britvich, G.I., et al., *New heavy plastic scintillators.* Instruments and Experimental Techniques, 2000. **43**(1): p. 36-39.

8. van Eijk, C.W.E., *Inorganic-scintillator development.* Nuclear Instruments and Methods in Physics Research Section A: Accelerators, Spectrometers, Detectors and Associated Equipment, 2001. **460**(1): p. 1-14.

9. Derenzo, S.E., et al., *The quest for the ideal inorganic scintillator.* Nuclear Instruments and Methods in Physics Research Section A: Accelerators, Spectrometers, Detectors and Associated Equipment, 2003. **505**(1-2): p. 111-117.

10. van Eijk, C.W.E., *Development of inorganic scintillators.* Nuclear Instruments and Methods in Physics Research Section A: Accelerators, Spectrometers, Detectors and Associated Equipment, 1997. **392**(1–3): p. 285-290.

11. Novotny, R., *Inorganic scintillators—a basic material for instrumentation in physics.* Nuclear Instruments and Methods in Physics Research Section A: Accelerators, Spectrometers, Detectors and Associated Equipment, 2005. **537**(1-2): p. 1-5.

12. Moses, W.W., et al., *Scintillation mechanisms in cerium fluoride.* Journal of Luminescence, 1994. **59**(1–2): p. 89-100.

13. van Eijk, C.W.E., *Cross-luminescence.* Journal of Luminescence, 1994. **60–61**: p. 936-941.

14. Huijun, Y., et al., *Energy transfer in multi component plastic scintillators.* Journal of Luminescence, 1984. **31–32, Part 2**: p. 833-835.

15. Shah, K.S., et al., *LaBr₃:Ce scintillators for gamma-ray spectroscopy.* Nuclear Science, IEEE Transactions on, 2003. **50**(6): p. 2410-2413.

16. Knoll, G.F., *Radiation detection and measurement*. 2000, New York: Wiley.

17. Ahmed, S.N. *Physics and engineering of radiation detection*. 2007; Academic Press.

18. Kume, H., K. Okano, and P. Hamamatsu, *Photomultiplier tube : principle to application : photon is our business*. 1994, [S.l.]: Hamamatsu Photonics.

19. Lecoq, P. *Inorganic scintillators for detector systems physical principles and crystal engineering*. Springer-Verlag Berlin and Heidelberg, 2006.

20. Bizarri, G., *Scintillation mechanisms of inorganic materials: From crystal characteristics to scintillation properties.* Journal of Crystal Growth, 2010. **312**(8): p. 1213-1215.

21. International Symposium on Organic, S. and D.L. Horrocks. *Organic scintillators; proceedings*. New York: Gordon and Breach.

22. Krasovitskii, B.M. and B.M. Bolotin, *Organic luminescent materials*. 1988, Weinheim; New York, NY, USA: VCH.

23. Brooks, F.D., *Development of organic scintillators.* Nuclear Instruments and Methods, 1979. **162**(1): p. 477-505.

24. Cho, Z.H., C.M. Tsai, and L.A. Eriksson, *Tin and Lead Loaded Plastic Scintillators for Low Energy Gamma-Ray Detection with Particular Application to High Rate Detection.* Nuclear Science, IEEE Transactions on, 1975. **22**(1): p. 72-80.

25. Hyman, M. and J.J. Ryan, *Heavy Elements in Plastic Scintillators.* Nuclear Science, IRE Transactions on, 1958. **5**(3): p. 87-90.

26. Hamel, M., et al., *Preparation and characterization of highly lead-loaded red plastic scintillators under low energy x-rays.* Nuclear Instruments and Methods in Physics Research Section A: Accelerators, Spectrometers, Detectors and Associated Equipment, 2011. **660**(1): p. 57-63.

27. Sandler, S.R. and K.C. Tsou, *Evaluation of organometallics in plastic scintillators toward γ-radiation.* The International Journal of Applied Radiation and Isotopes, 1964. **15**(7): p. 419-426.

28. Tsou, K.C., *Evaluation of Organometallic Compounds for Gamma Detection in Plastic Scintillators.* Nuclear Science, IEEE Transactions on, 1965. **12**(1): p. 28-33.

29. Dannin, J., S.R. Sandler, and B. Baum, *The use of organometallic compounds in plastic scintillators for the detection and resolution of gamma rays.* The International Journal of Applied Radiation and Isotopes, 1965. **16**(10): p. 589-597.

30. Rupert, B.L., et al., *Bismuth-loaded plastic scintillators for gamma-ray spectroscopy.* EPL (Europhysics Letters), 2012. **97**(2): p. 22002.

31. Steele, W.V., *The standard enthalpies of formation of the triphenyl compounds of the Group V elements 2. Triphenylbismuth and the Ph□Bi mean bond-dissociation energy.* The Journal of Chemical Thermodynamics, 1979. **11**(2): p. 187-192.

32. Cai, W., et al., *Synthesis of bulk-size transparent gadolinium oxide-polymer nanocomposites for gamma ray spectroscopy.* Journal of Materials Chemistry C, 2013. **1**(10): p. 1970-1976.

33. Lawrence, W.G., et al., *Quantum Dot-Organic Polymer Composite Materials for Radiation Detection and Imaging.* Nuclear Science, IEEE Transactions on, 2012. **59**(1): p. 215-221.

34. Kang, Z., et al., *CdTe quantum dots and polymer nanocomposites for x-ray scintillation and imaging.* Applied Physics Letters, 2011. **98**(18): p. 181914.

35. Yao, M., et al., *Luminescent LaF3:Ce-doped organically modified nanoporous silica xerogels.* Journal of Applied Physics, 2013. **113**(1).

36. Letant, S.E. and T.F. Wang, *Semiconductor quantum dot scintillation under gamma-ray irradiation.* Nano Letters, 2006. **6**(12): p. 2877-2880.

37. McKigney, E.A., et al., *LaF(3): Ce nanocomposite scintillator for gamma-ray detection*, in *Hard X-Ray and Gamma-Ray Detector Physics Ix*, R.B. James, A. Burger, and L.A. Franks, Editors. 2007.

38. McKigney, E.A., et al., *Nanocomposite scintillators for radiation detection and nuclear spectroscopy.* Nuclear Instruments and Methods in Physics Research Section A: Accelerators, Spectrometers, Detectors and Associated Equipment, 2007. **579**(1): p. 15-18.

39. Vasil'chenko, V.G. and A.S. Solov'ev, *Properties of composite scintillators in static and dynamic states.* Instruments and Experimental Techniques, 2003. **46**(6): p. 758-764.

40. Dai, S., et al., *Nanocrystal-based Scintillators for Radiation Detection.* AIP Conference Proceedings, 2002. **632**(1): p. 220-224.

41. Manickaraj, K., B.K. Wagner, and Z. Kang. *Radiation detection with CdTe quantum dots in sol-gel glass and polymer nanocomposites*. 2013.

42. Campbell, I.H. and B.K. Crone, *Quantum-Dot/Organic Semiconductor Composites for Radiation Detection.* Advanced Materials, 2006. **18**(1): p. 77-79.

43. Létant, S.E. and T.-F. Wang, *Study of porous glass doped with quantum dots or laser dyes under alpha irradiation.* Applied Physics Letters, 2006. **88**(10): p. 103110.

44. Manickaraj, K., B.K. Wagner, and Z. Kang, *Radiation detection with CdTe quantum dots in sol-gel glass and polymer nanocomposites*, in *Micro- and Nanotechnology Sensors, Systems, and Applications V*, T. George, M.S. Islam, and A.K. Dutta, Editors. 2013.

45. Feller, R.K., et al., *Large-scale synthesis of CexLa1-xF3 nanocomposite scintillator materials.* Journal of Materials Chemistry, 2011. **21**(15): p. 5716-5722.

46. Kang, Z., et al., *Synthesis of BaF2:Ce nanophosphor and epoxy encapsulated transparent nanocomposite.* Journal of Luminescence, 2011. **131**(10): p. 2140-2143.

47. Sahi, S., W. Chen, and K. Jiang, *Luminescence enhancement of PPO/PVT scintillators by CeF3 nanoparticles.* Journal of Luminescence, 2015. **159**: p. 105-109.

48. Liu, C., et al., *Facile Single-Precursor Synthesis and Surface Modification of Hafnium Oxide Nanoparticles for Nanocomposite γ-Ray Scintillators.* Advanced Functional Materials, 2015. **25**(29): p. 4607-4616.

49. Hossu, M., et al., *X-ray luminescence of CdTe quantum dots in LaF3:Ce/CdTe nanocomposites.* Applied Physics Letters, 2012. **100**(1).

50. Sahi, S. and W. Chen, *Luminescence enhancement in CeF3/ZnO nanocomposites for radiation detection.* Radiation Measurements, 2013. **59**(0): p. 139-143.

51. Cullity, B.D., *Elements of X-ray diffraction*. 1956, Reading, Mass.: Addison-Wesley Pub. Co.

52. Guo, Z. and L. Tan. *Fundamentals and applications of nanomaterials*. Artech House, 2009.

53. Williams, D.B., *Transmission electron microscopy 1, 1*. 1996, New York; London: Plenum Pr.

54. Oatley, C.W., *The Scanning electron microscope*. 1972, London: Cambridge University Press.

55. Smith, B.C., *Fundamentals of Fourier transform infrared spectroscopy*. 1996, Boca Raton: CRC Press.

56. Pan, W.-P. and L. Judovits. *Techniques in thermal analysis : hyphenated techniques, thermal analysis of the surface, and fast rate analysis*. West Conshohocken, PA: ASTM.

57. Kumar, C.S.S.R. *UV-VIS and photoluminescence spectroscopy for nanomaterials characterization*. Springer Berlin, Heidelberg, 2013.

58. Perkampus, H.-H., *UV-VIS spectroscopy and its applications*. 1992, Berlin; New York: Springer-Verlag.

59. *Faxitron X-ray Corp., Technical manual, models 43855A, 43855B, 43856A, Manual No. 5081-9519*

60. Moses, W.W., *<current trends in scintillator detector and materials.pdf>.* Nuclear Instruments and Methods in Physics Research Section A: Accelerators, Spectrometers, Detectors and Associated Equipment, 2002. **487**: p. 123-128

61. van Eijk, C.W.E., *Inorganic-scintillator development.* Nuclear Instruments & Methods in Physics Research Section a-Accelerators Spectrometers Detectors and Associated Equipment, 2001. **460**(1): p. 1-14.

62. Shah, K.S., et al., *LaBr3 : Ce scintillators for gamma-ray spectroscopy.* IEEE Transactions on Nuclear Science, 2003. **50**(6): p. 2410-2413.

63. vanEijk, C.W.E., *Development of inorganic scintillators.* Nuclear Instruments & Methods in Physics Research Section a-Accelerators Spectrometers Detectors and Associated Equipment, 1997. **392**(1-3): p. 285-290.

64. Létant, S.E. and T.F. Wang, *Study of porous glass doped with quantum dots or laser dyes under alpha irradiation.* Applied Physics Letters, 2006. **88**(10): p. 103110.

65. Moses, W.W. and S.E. Derenzo, *Cerium fluoride, a new fast, heavy scintillator.* IEEE Transactions on Nuclear Science, 1989. **36**(1): p. 173-176.

66. Anderson, D.F., *Properties of the high-density scintillator cerium fluoride.* IEEE Transactions on Nuclear Science, 1989. **36**(1): p. 137-140.

67. Jacobsohn, L.G., et al., *Fluoride Nanoscintillators.* Journal of Nanomaterials, 2011. **2011**: p. 1-6.

68. Bruchez Jr, M., *Semiconductor Nanocrystals as Fluorescent Biological Labels.* Science, 1998. **281**(5385): p. 2013-2016.

69. Byers, R.J. and E.R. Hitchman, *Quantum Dots Brighten Biological Imaging.* Progress in Histochemistry and Cytochemistry, 2011. **45**(4): p. 201-237.

70. Medintz, I.L., et al., *Self-assembled nanoscale biosensors based on quantum dot FRET donors.* Nature Materials, 2003. **2**(9): p. 630-638.

71. Eberl, K., et al., *Self-assembling InAs and InP quantum dots for optoelectronic devices.* Thin Solid Films, 2000. **380**(1-2): p. 183-188.

72. Zhang, Q., et al., *Toward highly efficient CdS/CdSe quantum dots-sensitized solar cells incorporating ordered photoanodes on transparent conductive substrates.* Physical Chemistry Chemical Physics, 2012. **14**(18): p. 6479.

73. Hossu, M., et al., *X-ray luminescence of CdTe quantum dots in LaF3:Ce/CdTe nanocomposites.* Applied Physics Letters, 2012. **100**(1): p. 013109.

74. Chen, W., *Nanoparticle fluorescence based technology for biological applications.* Journal of Nanoscience and Nanotechnology, 2008. **8**(3): p. 1019-1051.

75. Yao, M., et al., *Luminescence enhancement of CdTe nanostructures in LaF[sub 3]:Ce/CdTe nanocomposites.* Journal of Applied Physics, 2010. **108**(10): p. 103104.

76. Simpson, P.J., et al., *Superfast timing performance from ZnO scintillators.* Nuclear Instruments & Methods in Physics Research Section a-Accelerators Spectrometers Detectors and Associated Equipment, 2003. **505**(1-2): p. 82-84.

77. Bourret-Courchesne, E.D., et al., *Development of ZnO:Ga as an Ultra-Fast Alpha Particle Detector*, in *2006 Ieee Nuclear Science Symposium Conference Record, Vol 1-6*. 2006. p. 1541-1544.

78. Sun, D., et al., *Purification and stabilization of colloidal ZnO nanoparticles in methanol.* Journal of Sol-Gel Science and Technology, 2007. **43**(2): p. 237-243.

79. Sun, Z., et al., *Luminescence and Energy Transfer in Water Soluble CeF₃ and CeF₃:Tb³⁺ Nanoparticles.* Journal of Nanoscience and Nanotechnology, 2009. **9**(11): p. 6283-6291.

80. Elias, L.R., W.S. Heaps, and W.M. Yen, *Excitation of uv Fluorescence in La${\mathrm{F}}_{3}$ Doped with Trivalent Cerium and Praseodymium.* Physical Review B, 1973. **8**(11): p. 4989-4995.

81. Pedrini, C., et al., *One- and two-photon spectroscopy of Ce 3+ ions in LaF 3 -CeF 3 mixed crystals.* Journal of Physics: Condensed Matter, 1992. **4**(24): p. 5461.

82. Zhong Lin, W., *Zinc oxide nanostructures: growth, properties and applications.* Journal of Physics: Condensed Matter, 2004. **16**(25): p. R829.

83. Woo, B.K., et al., *The effects of aging on the luminescence of PEG-coated water-soluble ZnO nanoparticle solutions.* Journal of Physical Chemistry C, 2008. **112**(37): p. 14292-14296.

84. Feller, R.K., et al., *Large-scale synthesis of CexLa1−xF3 nanocomposite scintillator materials.* Journal of Materials Chemistry, 2011. **21**(15): p. 5716.

85. Vanheusden, K., et al., *Correlation between photoluminescence and oxygen vacancies in ZnO phosphors.* Applied Physics Letters, 1996. **68**(3): p. 403.

86. Irimpan, L., et al., *Size dependent fluorescence spectroscopy of nanocolloids of ZnO.* Journal of Applied Physics, 2007. **102**(6): p. 063524.

87. Ozgur, U., et al., *A comprehensive review of ZnO materials and devices.* Journal of Applied Physics, 2005. **98**(4).

88. Bandyopadhyay, P.K., G.W. Russell, and K. Chakrabarti, *Optically stimulated luminescence in KCl:Cu x-irradiated at room temperatur.* Radiation Measurements, 1999. **30**: p. 51-57.

89. Chen, W., A.G. Joly, and J. Roark, *Photostimulated Luminescence and Dynamics of AgI and Ag Nanoclusters in Zeolites* Physical Review B, 2002. **65**: p. 2454041.

90. Chen, W., et al., *X-ray storage luminescence of BaFCl:Eu2+ Single Crystals.* J ournal of Physical Chemistry B, 2005. **109**: p. 11505.

91. Chen, W., et al., *The Origin of X-ray Luminescence from CdTe Nanoparticles in CdTe/BaFBr:Eu2+ Nanocomposite Phosphors.* Journal of Applied Physics, 2006. **99**: p. 34302 1-5.

92. Chen, W., J. Song, and M. Su, *Electron Migration in BaFCl:Eu2+ Phosphors.* Journal of Applied Physics, 1997. **81**(7): p. 3170-3174.

93. Chen, W. and M. Su, *Stimulated Luminescence and Photo-gated hole burning in* $BaFCl_{0.8}\ Br_{0.2}:Sm^{2+},Sm^{3+}$ *Phosphors.* J. Phys. Chem., 1999. **60**: p. 371.

94. Chen, W., et al., *Dose Dependent X-Ray Luminescence in MgF2:Eu2+, Mn2+ Phosphors.* J. Appl. Phys. , 2008. **103**: p. 113103.

95. Chen, W., S.L. Westcott, and J. Zhang, *Dose Dependence of X-Ray Luminescence from CaF2:Eu2+, Mn2+ Phosphors,.* Appl. Phys. Lett., 2007. **91**: p. 211103.

96. Chen, W., et al., *New Color Centers and Photostimulated Luminescence of BaFCl:Eu2+.* J. Phys. Chem. Solids, 1998. **59**(1): p. 49-53.

97. Lecoq, P., *THE HIGH-ENERGY PHYSICS DEMAND FOR A NEW-GENERATION OF SCINTILLATORS.* Journal of Luminescence, 1994. **60-1**: p. 948-955.

98. van Eijk, C.W.E., *Inorganic scintillators in medical imaging detectors.* Nuclear Instruments & Methods in Physics Research Section a-Accelerators Spectrometers Detectors and Associated Equipment, 2003. **509**(1-3): p. 17-25.

99. Melcher, C.L., *INDUSTRIAL APPLICATIONS OF SCINTILLATORS*. Heavy Scintillators for Scientific and Industrial Applications - Crystal 2000, ed. F. DeNotaristefani, P. Lecoq, and M. Schneegans. 1993. 75-84.

100. Hamada, H.M., et al., *Radiation damage studies on the optical and mechanical properties of plastic scintillators.* Nuclear Instruments & Methods in Physics Research Section a-Accelerators Spectrometers Detectors and Associated Equipment, 1999. **422**(1-3): p. 148-154.

101. Zhong, H., et al., *Photoluminescence quenching of conjugated polymer nanocomposites for gamma ray detection.* Nanotechnology, 2008. **19**(50).

102. Liu, Y., et al., *X-ray luminescence of LaF3:Tb3+ and LaF3:Ce3+,Tb3+ water-soluble nanoparticles.* Journal of Applied Physics, 2008. **103**(6): p. -.

103. Liu, Y., et al., *Investigation of water-soluble x-ray luminescence nanoparticles for photodynamic activation.* Applied Physics Letters, 2008. **92**(4).

104. Sun, Z., et al., *Luminescence and Energy Transfer in Water Soluble CeF3 and CeF3:Tb3+ Nanoparticles.* Journal of Nanoscience and Nanotechnology, 2009. **9**(11): p. 6283-6291.

105. Liu, Y., Q. Ju, and X. Chen, *Water-Soluble Lanthanides Doped Fluoride Nanocrystals for Biolabeling: Materials and Photophysics.* Reviews in Nanoscience and Nanotechnology, 2012. **1**(3): p. 163-171.

106. Jacobsohn, L.G., et al., *Fluoride Nanoscintillators.* Journal of Nanomaterials, 2011. **2011**.

107. Li, C., et al., *LaF3, CeF3, CeF3 : Tb3+, and CeF3 : Tb3+@LaF3 (core-shell) nanoplates: Hydrothermal synthesis and luminescence properties (vol 112C, pg 2908, 2008).* Journal of Physical Chemistry C, 2008. **112**(39): p. 15602-15602.

108. Qu, X., et al., *Polyol-mediated solvothermal synthesis and luminescence properties of CeF3, and CeF3:Tb3+ nanocrystals.* Journal of Solid State Chemistry, 2011. **184**(2): p. 246-251.

109. Wang, L., et al., *The preparation of CeF3 nanocluster capped with oleic acid by extraction method and application to lithium grease.* Materials Research Bulletin, 2008. **43**(8-9): p. 2220-2227.

110. Ma, L., et al., *Synthesis and characterization of novel flower-like CeF3 nanostructures via a rapid microwave method.* Materials Letters, 2010. **64**(14): p. 1559-1561.

111. Arun Kumar, D., et al., *Structural and conductivity analysis on cerium fluoride nanoparticles prepared by sonication assisted method.* Solid State Sciences, 2012. **14**(5): p. 626-634.

112. Zhang, H., et al., *Synthesis and characterization of ultrafine CeF3 nanoparticles modified by catanionic surfactant via a reverse micelles route.* Journal of Colloid and Interface Science, 2006. **302**(2): p. 509-515.

113. Sunqing, Q., D. Junxiu, and C. Guoxu, *Tribological properties of CeF₃ nanoparticles as additives in lubricating oils.* Wear, 1999. **230**(1): p. 35-38.

114. Qiu, S., J. Dong, and G. Chen, *Synthesis of CeF3 nanoparticles from water-in-oil microemulsions.* Powder Technology, 2000. **113**(1–2): p. 9-13.

115. Dujardin, C., et al., *Luminescence and Scintillation Properties at the Nanoscale.* IEEE Transactions on Nuclear Science, 2010. **57**(3): p. 1348-1354.

116. Luchowski, R., *Two-photon excitation of 2,5-diphenyloxazole using a low power green solid state laser.* Chemical Physics Letters, 2011. **501**(4-6): p. 572-574.

117. Chirio-Lebrun, M.-C. and M. Prats, *Fluorescence resonance energy transfer (FRET): Theory and experiments.* Biochemical Education, 1998. **26**(4): p. 320-323.

118. Weber, M.J., *Inorganic scintillators: today and tomorrow.* Journal of Luminescence, 2002. **100**(1–4): p. 35-45.

119. Chen, W., et al., *Luminescence of La0.2Y1.8O3 nanostructured scintillators.* Optics Letters, 2014. **39**(19): p. 5705-5708.

120. Novotny, R., *Inorganic scintillators - a basic material for instrumentation in physics.* Nuclear Instruments & Methods in Physics Research Section a-Accelerators Spectrometers Detectors and Associated Equipment, 2005. **537**(1-2): p. 1-5.

121. Gektin, A., et al., *Inorganic–organic rubbery scintillators.* Nuclear Instruments and Methods in Physics Research Section A: Accelerators, Spectrometers, Detectors and Associated Equipment, 2002. **486**(1–2): p. 191-195.

122. Sahi, S., et al., *Investigation of luminescence mechanism in La0.2Y1.8O3 scintillator.* Journal of Luminescence, 2016. **173**: p. 99-104.

123. Iwanowska-Hanke, J., et al., *Comparative study of large samples (2" × 2") plastic scintillators and EJ309 liquid with pulse shape discrimination (PSD) capabilities.* Journal of Instrumentation, 2014. **9**(06): p. P06014.

124. Bertrand, G.H.V., et al., *Influence of bismuth loading in polystyrene-based plastic scintillators for low energy gamma spectroscopy.* Journal of Materials Chemistry C, 2014. **2**(35): p. 7304-7312.

125. Zhang, H., et al., *From Water-Soluble CdTe Nanocrystals to Fluorescent Nanocrystal–Polymer Transparent Composites Using Polymerizable Surfactants.* Advanced Materials, 2003. **15**(10): p. 777-780.

126. Zhang, H., et al., *Fluorescent Nanocrystal–Polymer Complexes with Flexible Processability.* Advanced Materials, 2005. **17**(7): p. 853-857.

127. Zhang, H., et al., *Fluorescent Nanocrystal−Polymer Composites from Aqueous Nanocrystals: Methods without Ligand Exchange.* Chemistry of Materials, 2005. **17**(19): p. 4783-4788.

128. Derenzo, S.E., et al., *The quest for the ideal inorganic scintillator.* Nuclear Instruments and methods in Physics Research A, 2003. **505**: p. 111-117.

129. Rodnyi, P.A., *Physical Processes in Inorganic Scintillators*. 1997, N. Y.: CRC Press.

130. Eijk, C.v., *Inorganic scintillators in medical imaging.* Phys. Med. Biol., 2002. **47**: p. R85.

131. Fiorini, C., et al., *Gamma-Ray Spectroscopy With LaBr3:Ce Scintillator Readout by a Silicon Drift Detector.* IEEE TRANSACTIONS ON NUCLEAR SCIENCE,, 2006. **53**(4): p. 2392.

132. González, R., et al., *Performance Comparison of a Large Volume CZT Semiconductor Detector and a LaBr3(Ce) Scintillator Detector.* IEEE TRANSACTIONS ON NUCLEAR SCIENCE,, 2006. **53**(4): p. 2409.

133. Siciliano, E.R., et al., *Comparison of PVT and NaI(Tl) scintillators for vehicle portal monitor applications.* Nuclear Instruments and Methods in Physics Research A, 2005. **550**: p. 647-674.

134. Torrisi, L., *Radiation damage in polyvinyltoluene (PVT).* Radiation Physics and Chemistry, 2002. **63**: p. 89-92.

135. Beddar, A.S., *Plastic scintillation dosimetry and its application to radiotherapy.* Radiation Measurements, 2007. **41**: p. S124-S133.

136. McKigney, E.A., et al., *Nanocomposite scintillators for radiation detection and nuclear spectroscopy* Nucl. Instr. and Meth. in Phys. Res. A, 2007. **579**(1): p. 15-18.

137. Letant, S.E. and T.-F. Wang, *Semiconductor Quantum Dot Scintillation under γ-Ray Irradiation.* Nano Lett., 2006. **6**: p. 2877.

138. Wisniewski, D.J., et al., *Development of novel polycrystalline ceramic scintillators.* IEEE Transactions on Nuclear Science, 2008. **55**(3): p. 1501-1508.

139. Cherepy, N.J., et al., *Comparative gamma spectroscopy with SrI2(Eu), GYGAG(Ce) and Bi-loaded plastic scintillators.* Ieee Nuclear Science Symposium Conference. Proceedings, 2010: p. 1288-1291.

140. Cherepy, N.J., et al., *Transparent Ceramic Scintillators for Gamma Spectroscopy and Radiography*, in *Hard X-Ray, Gamma-Ray, and Neutron Detector Physics Xii*, A. Burger, L.A. Franks, and R.B. James, Editors. 2010.

141. Ding, J., et al., *Investigation of the spectroscopic properties of (Y0.92-xLa0.08Ndx)(2)O-3 transparent ceramics.* Journal of the Optical Society of America B-Optical Physics, 2007. **24**(3): p. 681-684.

142. Hao, Q., et al., *Low-threshold and broadly tunable lasers of Yb(3+)-doped yttrium lanthanum oxide ceramic.* Applied Physics Letters, 2008. **92**(21).

143. Hoskins, R.H. and B.H. Soffer, *STIMULATED EMISSION FROM Y2O3:Nd3+.* Applied Physics Letters, 1964. **4**(1): p. 22-23.

144. Li, Y.H., Q.H. Yang, and S.Z. Lu, *Fabrication and Characterization of Yttrium Lanthanum Oxide Transparent Ceramics Using Powders Prepared by Different methods*, in *Materials and Manufacturing, Pts 1 and 2*, J.H. Wang and J.G. Qi, Editors. 2011. p. 588-591.

145. Luo, J., et al., *Combustion synthesis of a nanoceramic and its transparent properties.* Physica B 2012. **407**: p. 2705-2708.

146. Luo, J., Z. Zhong, and J. Xu, *Yttrium oxide transparent ceramics by low-temperature microwave sintering.* Mater. Res. Bull., 2012. **47**: p. 4283-4285.

147. Hayes, W., et al., *AN ODMR STUDY OF EXCITON TRAPPING IN Y2O3 AND SC2O3.* Journal of Physics C-Solid State Physics, 1984. **17**(14): p. L383-L387.

148. Fukabori, A., et al., *Optical and scintillation characteristics of Y2O3 transparent ceramic.* Journal of Applied Physics, 2010. **107**(7): p. 073501.

149. Lushchik, A., et al., *Luminescence of free and self-trapped excitons in wide-gap oxides.* Journal of Luminescence, 2000. **87–89**(0): p. 232-234.

150. Babin, V., et al., *Luminescent properties of RE2O3 (RE = Lu, Sc, Y) single crystals and ceramics*.* Eur. Phys. J. B, 2013. **86**(3): p. 93.

151. Fukabori, A., et al., *Growth of Y2O3, Sc2O3 and Lu2O3 crystals by the micro-pulling-down method and their optical and scintillation characteristics.* Journal of Crystal Growth, 2011. **318**(1): p. 823-827.

152. Kirm, M., et al., *Self-trapping and multiplication of electronic excitations in Al_2O_3 and Al_2O_3:Sc crystals.* Physical Review B, 1999. **60**(1): p. 502-510.

153. Williams, R.T. and K.S. Song, *The self-trapped exciton.* J. Phys. Chem. Solids, 1990. **51**: p. 679.

154. Pankratov, V., M. Kirm, and H.v. Seggern, *Intrinsic luminescence in yttrium trifluoride.* J. Lumin., 2005. **113**: p. 143.

155. Lushchik, A., et al., *Luminescence of free and self-trapped excitons in wide-gap oxides.* J. Lumin., 2000. **87-89**(232).

156. Rosenberg, R.A., et al., *Anisotropic x-ray absorption effects in the optical luminescence yield of ZnO nanostructures.* Applied Physics Letters, 2006. **89**(9): p. 093118.

157. Wood, R.L. and W. Hayes, *A study of recombination centres in YAlO 3 , EuAlO 3 , LaAlO 3 and Y 2 O 3 using ODMR.* Journal of Physics C: Solid State Physics, 1982. **15**(35): p. 7209.

158. Babin, V., et al., *Time-resolved spectroscopy of exciton states in single crystals and single crystalline films of YAlO 3 and YAlO 3 : Ce.* Journal of Physics D: Applied Physics, 2011. **44**(31): p. 315402.

Biographical Information

Sunil Sahi has completed his high school education from Kolkata, India. He received his Bachelor of Science (B.Sc) degree in Physics from Tribhuvan University, Kathmandu, Nepal. After receiving his Master of Science (M.Sc) degree in Physics from Tribuvan University, Kathmandu, Nepal in 2007 he moved to the United State of America for higher education.

Sunil enrolled as a PhD student at the Department of Physics, University of Texas at Arlington in the spring of 2010. During his PhD studied he worked in the development of nanocomposite scintillators under the supervision of Dr. Wei Chen. He has authored six scientific publications peer-reviewed and published in various journals. During his PhD studied he has received scholarships and fellowship such as John D. McNutt Memorial Scholarship (2011), Richard Jack Marquis Physics Scholarship (2015) and Dean's Dissertation Fellowship (2015). He obtained his PhD degree in Physics in the spring of 2016. The author's interest of research area includes scintillator detectors, polymer nanocomposites, solid state lighting and nanotechnology.